A Search for Alternative Electronic Order in the High Temperature Superconductor $Bi_2Sr_2CaCu_2O_{8+\delta}$ by Scanning Tunneling Microscopy

by

Jennifer Eve Hoffman

B.A. (Harvard University) 1999
M.A. (University of California, Berkeley) 2001

A dissertation submitted in partial satisfaction of the

requirements for the degree of

Doctor of Philosophy

in

Physics

in the

GRADUATE DIVISION

of the

UNIVERSITY OF CALIFORNIA, BERKELEY

Committee in charge:
Professor J. C. Séamus Davis, Chair
Professor Dung-Hai Lee
Professor Norman Phillips

Fall 2003

The dissertation of Jennifer Eve Hoffman is approved:

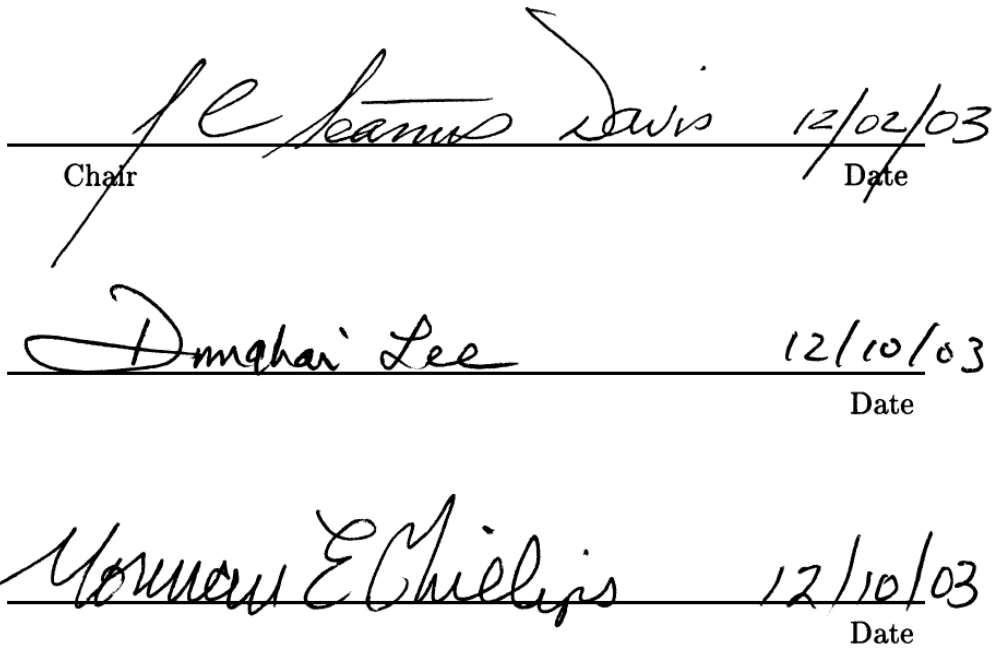

Chair Date

Date

Date

University of California, Berkeley

Fall 2003

A Search for Alternative Electronic Order in the High Temperature Superconductor $Bi_2Sr_2CaCu_2O_{8+\delta}$ by Scanning Tunneling Microscopy

by

Jennifer Eve Hoffman

(Version 2, minor revisions, August 2004)

Abstract

A Search for Alternative Electronic Order in the High Temperature Superconductor $Bi_2Sr_2CaCu_2O_{8+\delta}$ by Scanning Tunneling Microscopy

by

Jennifer Eve Hoffman

Doctor of Philosophy in Physics

University of California, Berkeley

Professor J. C. Séamus Davis, Chair

High temperature superconductors were discovered in 1986, but despite a frantic pace of research, resulting in some 10^4 publications per year for the last 16 years, these materials remain poorly understood. Because their electronic structure is both inhomogeneous and highly correlated, a full understanding will require knowledge of quasiparticle properties both in real space and momentum space. These materials also exhibit a rich three-dimensional phase diagram parameterized by temperature, magnetic field, and carrier concentration. Despite numerous theoretical predictions for exotic phases, large regions of parameter space remain unexplored due to experimental limitations.

In this thesis, I will present the first application of Fourier-transform scanning tunneling spectroscopy (FT-STS) to a high temperature superconductor, $Bi_2Sr_2CaCu_2O_{8+\delta}$. For the first time, a single experiment can simultaneously probe the real space and momentum space properties of the quasiparticles. FT-STS shows that the quasiparticles in optimally doped BSCCO at 4.2 K and zero applied field can be described by a *d*-wave superconducting phase, without the need to invoke any exotic order parameters.

I will also present scanning tunneling microscopy (STM) studies of nanoscale features in BSCCO. With such a local probe, we may take advantage of spatial inhomogeneity to gain insight into phases inaccessible to bulk experiments. Crystal inhomogeneity allows the use of single atom defects to probe nanoscale domains of very underdoped BSCCO, sug-

gesting that the electronic structure there is very different from that in the superconducting state. Field inhomogeneity, because BSCCO is a type-II superconductor, allows the study of magnetic vortices, another kind of nanoscale domain where superconductivity is destroyed. Remarkably, in vortices I find evidence of a four-unit-cell periodic "checkerboard"-like electronic structure. This may be the first local glimpse into the structure of the mysterious "pseudogap" phase whose bulk properties are exhibited by all high temperature superconducting materials outside of the superconducting dome.

J C Séamus Davis

Professor J. C. Séamus Davis
Dissertation Committee Chair

To my husband,

Daniel Todd Larson

who can always find a way to make me laugh.

Contents

List of Figures

List of Tables

Acknowledgments

Without the support of many people in many places, this thesis could not have been written. I'd like to thank first of all my emotional support network: my husband Daniel Larson who helped me to laugh through all the obstacles which appeared in my path during graduate school, and my parents Edward & Caroline Hoffman who were always only a phone call away. Graduate school included many frustrations as well as triumphs, but I was lucky to have kind and patient listeners. Thanks also to the running partners and soulmates whom I was so lucky to find during my last year at Berkeley: Jenni Buckley and Joey & David Kimdon.

Thanks to my labmates, who doubled as friends and teachers. To Kyle McElroy for laughs and sarcasm and heated discussions of physics. To Joan Hoffmann for more sarcasm, much empathy in issues both personal and academic, and innumerable chocolate emergency missions. To Kristine Lang and Eric Hudson who have been big sister and big brother to me and have answered many of my dumb questions both about physics and life. To Krishna Swamy who somehow tolerated a year and a half of sharing a lab with me, and retaught me the value of teamwork in science. To Sudeep Dutta, Christian Lupien, Barry Barker, and Rob Johnson for laughter, advice, and shared memories. To Peter Hamel for being smart and independent, and for often doing the dirty work, if not cheerfully, at least capably. To Annie Endozo and Lorraine Sadler for hugs and the comfort and support of another female presence in the physics department at stressful times.

Thanks to many of the people who made my work so much easier. To Anne Takizawa who was always willing to drop everything in order to listen to a problem or find an impossible solution impossibly quickly. To Donna Sakima and Claudia Trujillo who always had smiles and often candy to go along with their frequent help as I struggled to run SWPS and then teach physics 141.

Thanks to the guys in the machine shop who spent so much time giving me advice and critiquing my designs: Tom Pedersen, Dave Murai, Pete Thuesen, Steve Butler, and Marco Ambrosini. Thanks also to Pat Bonnefil in the electronics shop for his advice and patience especially during my last few frantic months.

Thanks to Lynne Pelosi for a few last minute Friday afternoon purchases which wouldn't have gone out on time without special attention. Thanks to Laura Ng for a smile and personal greeting every time I stepped into the physics library. And thanks especially to Eleanor Crump, who knows everything about everything about the workings of Birge and LeConte and always managed to find a few seconds to share her smile, her personal concern

for my well-being, and her tricks for getting emergency construction projects done quickly.

Thanks to Kathryn Moler for her patience as I struggled to complete this thesis while ramping up as a post-doc in her lab. I wish I could have put 100% effort into both responsibilities simultaneously. Thanks also to the rest of the Moler group for their friendship and inclusiveness during this stressful semester.

A special thanks to my surrogate advisors at Berkeley. To Richard Packard who helped me to launch fearlessly into a construction project which turned out to be both harder and more rewarding than I had imagined, and which now forms a cornerstone of my self confidence that I can do anything in lab that I set my mind to. To John Clarke who was endlessly supportive and frequently popped his head into my lab just to check how I was doing at the end of the day. Teaching with him was one of the most rewarding experiences of graduate school: I learned from him new ways to understand solid state physics, but more importantly how to be a clear and patient teacher. Thanks especially to Dung-Hai Lee who provided the brilliant theoretical insights behind the most exciting discoveries I was fortunate enough to play a role in during graduate school. His patience in explaining simple concepts was wonderful, and his enthusiasm for beautiful explanations was absolutely contagious. I hope that we can continue to work together for a long time.

Finally, by far my biggest debt of gratitude is to my advisor, Séamus Davis. Without him, none of this would be possible. We have at times tried each other's patience, but I have again and again benefited from his calm and imperturbability. He has taught me quite a lot of physics, but perhaps even more importantly he has taught me a whole way of thought: how to break a goal down and think both tactically and strategically about it, then just get the job done.

I would also like to acknowledge the Fannie and John Hertz Foundation, which provided me with two years of generous financial support during graduate school.

Jennifer E. Hoffman

Curriculum Vitae

Department of Physics	Phone: 617-384-9487
Harvard University	Fax: 617-495-0416
Cambridge, MA 02138	E-mail: jhoffman@physics.harvard.edu

Education

Dec. 2003	Ph.D. Physics (experimental condensed matter), University of California, Berkeley
May 2001	M.A. Physics, University of California, Berkeley
June 1999	B.A. Physics, Magna Cum Laude, Highest Honors in Physics, Harvard University

Research and Teaching Positions

2003–04	Stanford University, Postdoctoral Research Associate, K. A. Moler Group
1999–2003	UC Berkeley, Graduate Student Research Assistant, J. C. Davis Group
1999, 2002–03	UC Berkeley, Graduate Student Instructor, Physics Department
Summer 1999	UC Berkeley and Fermi National Accelerator Laboratory, Graduate Student Research Assistant, Y. K. Kim Group
1996–98	Harvard University, Research Assistant, E. Mazur Group

Fellowships and Awards

2003	Outstanding Graduate Student Instructor, University of California, Berkeley
2001–03	Hertz Graduate Fellowship, Fannie & John Hertz Foundation
2001	NSF Graduate Fellowship (declined), National Science Foundation
2001	National Defense Science and Engineering Graduate Fellowship (declined), Department of Defense
2001	Mentored Research Award (declined), University of California
1999–01	Physics Department Fellowship, University of California, Berkeley
1998–99	Goldwater Fellowship, Barry Goldwater Foundation
1996–99	Robert Byrd Scholarship, State of Connecticut Department of Higher Education
1996	National Merit Scholarship, National Merit Scholarship Corporation

Publications

[1] "Relating atomic-scale electronic phenomena to wave-like quasiparticle states in superconducting $Bi_2Sr_2CaCu_2O_{8+\delta}$," K. McElroy, R.W. Simmonds, J.E. Hoffman, D.-H. Lee, J. Orenstein, H. Eisaki, S. Uchida, J.C. Davis, *Nature* **422**, 592 (2003).

[2] "Imaging quasiparticle interference in $Bi_2Sr_2CaCu_2O_{8+\delta}$," J.E. Hoffman, K. McElroy, D.-H. Lee, K.M. Lang, H. Eisaki, S. Uchida, J.C. Davis, *Science* **297**, 1148 (2002).

[3] "A four unit cell periodic pattern of quasi-particle states surrounding vortex cores in $Bi_2Sr_2CaCu_2O_{8+\delta}$," J.E. Hoffman, E.W. Hudson, K.M. Lang, V. Madhavan, H. Eisaki, S. Uchida, J.C. Davis, *Science* **295**, 466 (2002).

[4] "Imaging the granular structure of high-T_c superconductivity in underdoped $Bi_2Sr_2CaCu_2O_{8+\delta}$," K.M. Lang, V. Madhavan, J.E. Hoffman, E.W. Hudson, H.Eisaki, S. Uchida, J.C. Davis, *Nature* **415**, 412 (2002).

Invited Talks

- "Scanning Tunneling Spectroscopy of High Temperature Cuprate Superconductors." Condensed Matter Seminar, Caltech Physics Department, 23 May 2003.
- "Wavefunction Imaging in High Temperature Cuprate Superconductors." Condensed Matter Seminar, University of California, Los Angeles Physics Department, 21 May 2003.
- "Wavefunction Imaging in High Temperature Cuprate Superconductors." Condensed Matter Seminar, University of California, Berkeley Physics Department, 28 April 2003.
- "Wavefunction Imaging in High Temperature Cuprate Superconductors." Yale University Applied Physics Department, 17 April 2003.
- "Wavefunction Imaging in High Temperature Cuprate Superconductors." Harvard University Physics Department, 3 April 2003.
- "Quasiparticle Interference in $Bi_2Sr_2CaCu_2O_{8+\delta}$." Aspen Center for Physics, conference on Condensed Matter Physics: Complex Quantum Order, Aspen, Colorado, 11 February 2003.
- "Imaging Quasiparticle Interference in $Bi_2Sr_2CaCu_2O_{8+\delta}$." International Conference on Physics and Chemistry of Molecular and Oxide Superconductors (MOS), Hsinchu, Taiwan, 14 August 2002.
- "Incommensurate Conductance Modulations from Quasiparticle Scattering in $Bi_2Sr_2CaCu_2O_{8+\delta}$." Stanford University Applied Physics Department, 15 July 2002.
- "Checkerboards in $Bi_2Sr_2CaCu_2O_{8+\delta}$." Stanford University Applied Physics Department, 28 May 2002.
- "Imaging Quasiparticle Interference in $Bi_2Sr_2CaCu_2O_{8+\delta}$." Condensed Matter Seminar, M.I.T. Physics Department, 17 April 2002.
- "Introduction to the Scientific Community." MATHCOUNTS National Competition, Washington, D.C., May 1998.
- "Networking for Student Success." College Board National Forum, New York, NY, November 1996.

Research

- **UHV-compatible, Scanning Tunneling Microscope Construction, J.C. Davis Group, Physics Department, UC Berkeley, 2001-2003.** I have designed, purchased, assembled, debugged, and operated a cryogenic high-resolution STM system, which achieved atomic resolution on the cuprate superconductor $Bi_2La_xSr_{2-x}Cu0_{4+\delta}$.
- **Scanning Tunneling Microscopy of High-T_c Superconductors, J.C. Davis Group, Physics Department, UC Berkeley, 2000-2003.** I have used a 4 K scanning tunneling microscope with sub-Ångstrom resolution to probe the local density of states of $Bi_2Sr_2CaCu_2O_{8+\delta}$. Specific studies have included: the effect of Ni and Zn impurities and their relation to local superconducting gap magnitude, electronic structure of magnetic vortices, and long-range quasiparticle interference patterns due to disorder scattering. I have applied the technique of Fourier-transform scanning tunneling spectroscopy for the first time to the cuprates, using an STM to provide simultaneous real-space and momentum-space information about the quasiparticles.
- **Branching Fractions in J/Ψ Production, Fermi National Laboratory, Summer 1999.** I wrote code to analyze over one million potential J/Ψ events to determine what fraction of the actual J/Ψ particles resulted from decay of a B-meson.
- **Femtosecond Laser Catalysis of Chemical Reactions on a Platinum Surface, E. Mazur Group, Physics Department, Harvard University, Summer 1996-Winter 1998.** Using a femtosecond laser in a UHV chamber I studied reactions of carbon, oxygen, methyl iodide, and benzene on a platinum surface.

Community Service

- Coordinator, Society for Women in Physical Sciences, UC Berkeley, 2000-2001.
- Mentor, Society for Women in Physical Sciences, UC Berkeley, 1999-2000.
- Counselor, Research Science Institute, MIT, Summer 1997.

Chapter 1

Introduction

A superconductor is a material which exhibits the following two properties:

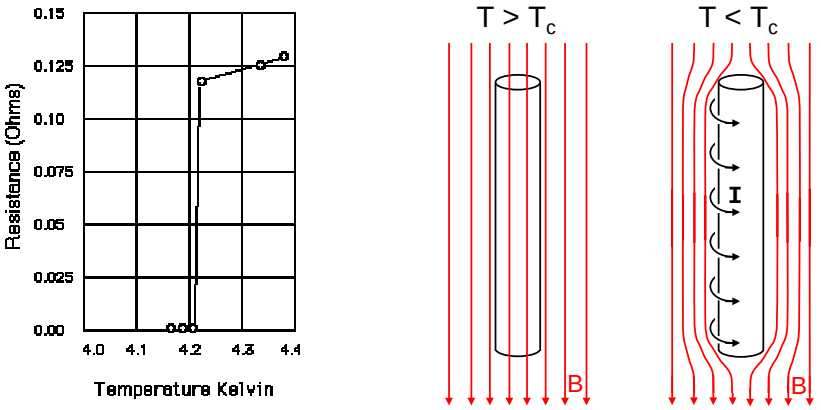

(a) Vanishing resistance (b) Meissner effect

Figure 1.1: Two requirements for superconductivity: (a) vanishing of electrical resistivity below a critical temperature T_c, discovered in mercury by Kamerlingh-Onnes[1] in 1911; and (b) expulsion of magnetic flux below a critical field H_c, discovered by Meissner and Ochsenfeld[2] in 1933.[a]

[a] I attempted to find an original figure from the Meissner paper, to match this famous original figure from the Kamerlingh-Onnes paper. To my surprise, I found that despite reporting one of the most important results in experimental condensed matter physics, the original Meissner paper exists only in German, is a mere 3/4 of a page long, and contains no figures and no numerical data.

1.1 Conventional Superconductors

The phenomenon of superconductivity was first discovered in mercury by Kamerlingh Onnes[1] in 1911. As legend has it, Kamerlingh Onnes at first attributed the sudden drop in resistivity to an experimental error, such as an accidental short circuit. But careful repetition assured him that he had indeed discovered a new electronic phase. The discovery of vanishing resistivity in several other elements such as tin and lead soon followed.

The second, equally surprising characteristic of superconductivity, expulsion of magnetic flux from the superconducting state, was discovered by Meissner and Ochsenfeld in 1933.[2] Over the next several decades, theorists struggled to find a microscopic theory for superconductivity. Major advances were made with the London theory[3] in 1935 and the Ginzburg-Landau theory[4] in 1950. But it was not until 1957, a whole 46 years after the original experimental discovery of superconductivity, that a universally accepted microscopic theory of the phenomenon was put forth by Bardeen, Cooper, and Schrieffer.[5]

The basic idea of BCS theory is that electrons (fermions) pair via phonon coupling, and the pairs (bosons) condense into a single coherent ground state which allows the electrons to move cooperatively through the crystal without losing their forward momentum. The underlying points of the theory are that the Fermi surface is unstable to infinitesimal attractive forces,[6] and phonon coupling provides such an attractive force.[7] Therefore, the total energy of the system can be reduced by allowing electrons to pair, which causes an increase in kinetic energy but a much larger decrease in potential energy. The paired electrons have equal and opposite momentum, and must scatter in tandem, so the total momentum of the electrons in the system (i.e. the current) is conserved by scattering; thus the superconductivity.

Two of the key experimental facts that led to the BCS understanding were:

1. The density of states is gapped at the Fermi surface. This was determined experimentally first by the measurement of an exponential specific heat.[8, 9] This led to the realization that some kind of pairing is occurring (i.e. electrons are thermally activated across a gap with Boltzmann probability). The gap was later confirmed by electromagnetic absorption in aluminum[10] and lead.[11, 12]

2. Phonons are involved. This was shown experimentally by the isotope effect:[13, 14] the critical temperature T_c was found to vary as the inverse square root of the nuclear mass. Since the phonon frequency varies as $\sqrt{k/M}$, the discovery of the isotope effect led to the realization that phonons are involved.

Armed with these and other experimental facts, BCS were finally able to put the whole picture together. Numerous details were filled in over the next few decades, but the problem of superconductivity was largely considered solved by BCS in 1957.

1.2 High-Temperature Superconductors

For obvious technological reasons, the search continued for materials which could superconduct at higher temperatures. Despite much work, for decades the highest T_c's belonged to Nb_3Sn (18K) then Nb_3Ge (23K), and the field was considered by many to be at a dead end. A history of the increase in record T_c is shown in figure 1.2.

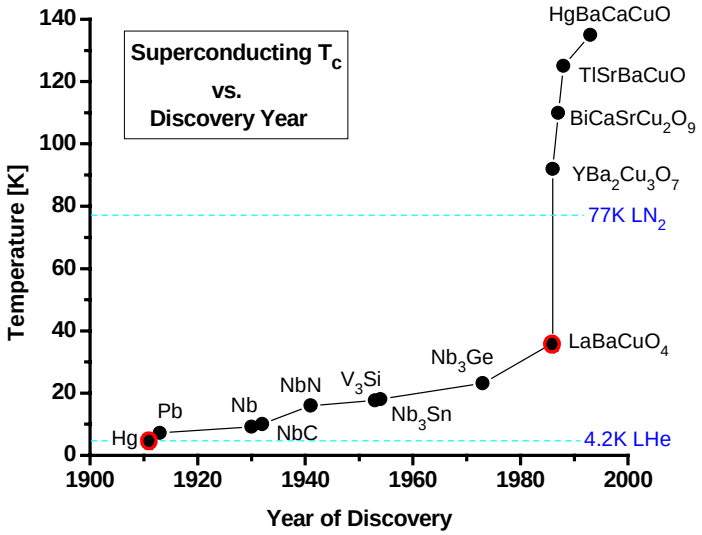

Figure 1.2: Highest T_c discovery history. (Points circled in red garnered a Nobel Prize for their discoverers: Kamerlingh-Onnes in 1913 and Bednorz & Müller in 1987.)

1.2.1 Discovery and Initial Questions

Three decades after BCS, in 1986, a startling discovery reopened the field of superconductivity research. Bednorz and Müller, working at IBM in Switzerland, discovered a new class of superconducting materials starting with LaBaCuO, which is superconducting up to 30 K.[15] The following year, the liquid nitrogen temperature barrier (77 K) was broken with the discovery of $YBa_2Cu_3O_{7-\delta}$, superconducting at 90 K.[16] Soon a whole host of related materials were found. Since the common component in all these new high temperature superconductors is a CuO_2 plane, these materials are referred to as the "cuprates."

The discovery of superconductivity in the cuprates was surprising for several reasons. No previous oxide superconductors had ever been found. Furthermore, in their stoichiometric form (with no additional oxygen or other dopant atoms added) these materials are antiferromagnetic Mott insulators. It is conventional wisdom that magnetism cannot coexist with superconductivity. For example, Abrikosov and Gor'kov showed that magnetic impurities disrupt superconductivity and depress T_c.[17, 18]

The obvious differences between these new high-temperature superconductors (HTSCs) and the old conventional superconductors created a great deal of excitement. Rapidly, all the old experiments which had lead to the unifying theory of conventional superconductors were repeated. But the results were often confusing and/or contradictory.

Pairing

It is now generally agreed that there is a gap in the density of states, but instead of the simple symmetric s-wave gap found in conventional superconductors, the gap is $d_{x^2-y^2}$-wave. This was shown by flux modulation measurements in a YBCO DC-SQUID[19] and then more unambiguously by flux quantization in a tri-crystal YBCO junction.[20] In simple terms, this $d_{x^2-y^2}$-wave gap means that electrons traveling different directions in the crystal feel a different pairing potential.

As would be expected from the gap in the density of states, it is generally agreed that electrons are paired. It was shown unambiguously by measurement of $h/2e$ flux quanta,[21] which indicates that the charge carriers have charge $2e$.

It is not generally agreed what causes the pairing. Of course the first thing to look for is phonons, but tests for the isotope effect have been inconclusive, in part because it's not clear which phonons are key. The cuprate crystal structures are much more complicated than the conventional superconductors, with typically four or five different elements per unit cell. Different atoms are involved in different phonons, so it's not obvious which isotope should be varied. No clear dependence of T_c on isotope has been found.

Because magnetism is known to play a role in the crystal at low carrier concentration, many argue strongly that electron pairing in high temperature superconductivity is caused by magnons or other magnetic consequences. But there are also strong arguments that pairing is indeed caused by phonons.[22]

Doping

Perhaps the most notable complicating factor in the high-T_c superconductors is the existence of a whole new parameter which can be tuned: carrier concentration. This leads to a 3-dimensional phase diagram rather than the simple temperature vs. B-field phase diagram of the conventional superconductors. In HTSC materials, the stoichiometric parent compounds are insulators, and it is not until charge carriers are added that these materials become superconducting. Typically charge carriers in the form of holes are added by doping oxygen interstitially (e.g. $Bi_2Sr_2CaCu_2O_{8+\delta}$), by substituting a monovalent atom with a divalent atom (e.g. replacing La with Sr in $La_{2-x}Sr_xCuO_4$), or by removal of oxygen from their stoichiometric positions (e.g. $YBa_2Cu_3O_{7-\delta}$). In any case, the carrier concentration is an important variable upon which the properties of the material depend strongly. We now have a 3-dimensional phase diagram, as shown in figure 1.3.

There have also been discovered many electron-doped superconductors, with a phase diagram that is approximately the mirror image of the hole-doped materials. But the T_c's of the electron-doped materials are not as high, and these materials will not be discussed in this thesis.

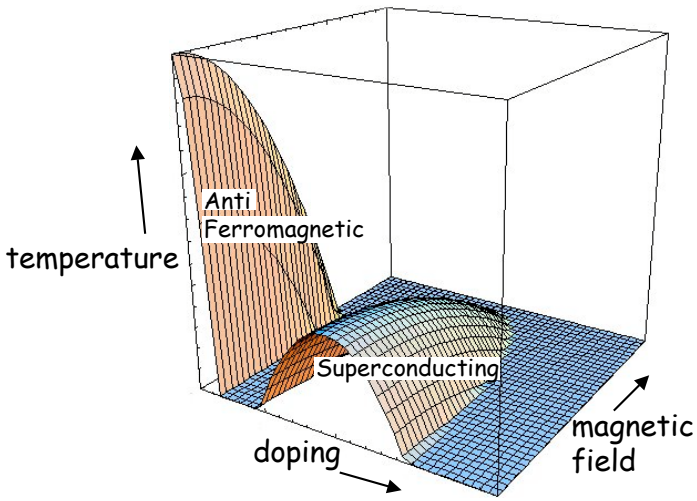

Figure 1.3: High-T_c 3-dimensional phase diagram. The state of the system is parameterized by carrier concentration (doping), temperature, and magnetic field. Two known phases are antiferromagnetism (at low doping) and superconductivity; little is known about the electronic structure throughout the rest of phase space.

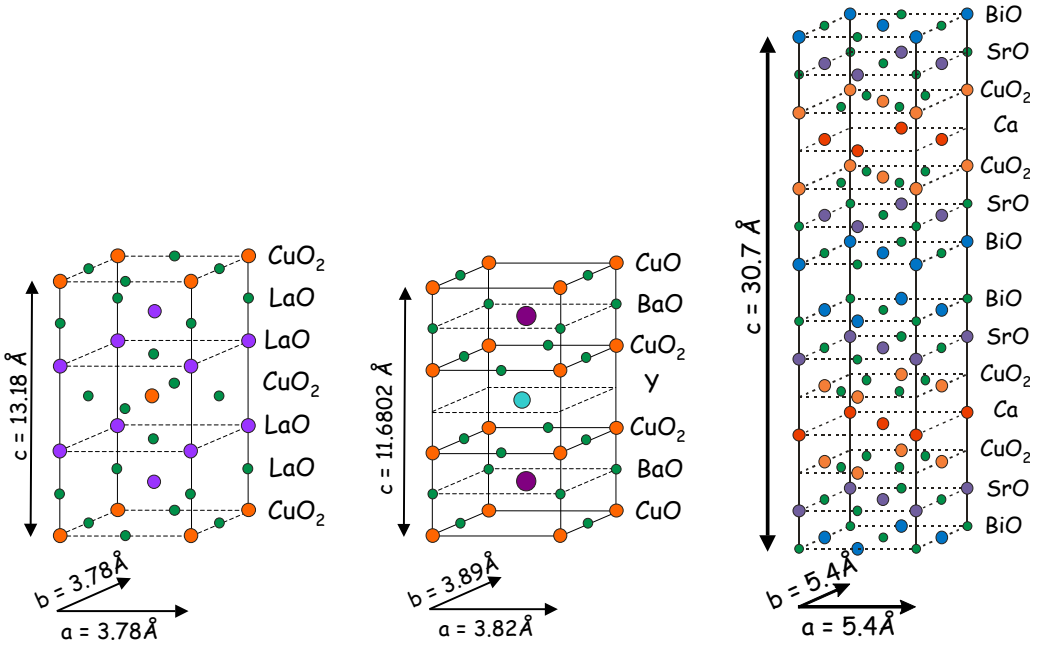

(a) LSCO (b) YBCO (c) BSCCO

Figure 1.4: Structure of the three high-T_c cuprate superconductor families: (a) $La_{2-x}Sr_xCuO_4$, (b) $YBa_2Cu_3O_{7-\delta}$, and (c) $Bi_2Sr_2CaCu_2O_{8+\delta}$.

1.2.2 Materials and the Proliferation of Experiments

There are three main families of hole-doped high temperature superconductors studied today. However, much of the confusion in the study of HTSC results from the fact that each material is accessible to different experimental techniques. For example, it is easy to measure the electronic density of states of $Bi_2Sr_2CaCu_2O_{8+\delta}$, but harder to measure its magnetic properties. In the quest to find a unifying theory for all HTSC, it is tempting to treat these three families as one material, and combine the experimental results from all families. Because of this common practice, the field of high-T_c research is rife with conflict and apparent contradictions.

A good summary of the zoology of many of the known hole-doped HTSC materials along with an explanation of the variation in their T_c's is given by Eisaki *et al.*[23]

$La_{2-x}Sr_xCuO_4$

The lanthanum family of high-T_c's was the first family of materials to be discovered, by Bednorz and Müller in 1986.[15] The structure of LSCO is shown in figure 1.4(a).

LSCO is physically the hardest of the three materials, and with stronger bonds it is easier to grow large (> 1 cm!) single crystals. Neutron scattering experiments, which probe the magnetic structure of the material, are typically limited to studying LSCO because of their requirement for large single crystals.

But LSCO has not been successfully studied with an STM, because so far there has been no successful recipe to obtain an atomically flat surface with tunnel access through an insulating layer to the relevant unperturbed CuO_2 plane.

$YBa_2Cu_3O_{7-\delta}$

The discovery of YBCO followed that of LSCO within a year.[16] YBCO was the first material to break the 77 K (liquid nitrogen) temperature boundary. The optimal T_c is now $\sim$ 90 K. The structure of YBCO is shown in figure 1.4(b). YBCO has perhaps been the most highly studied because it is the cleanest and most ordered crystal. But studies of YBCO can also be quite confusing because there are two CuO planes: the square plane and the chain plane. By analogy with the other HTSC families, it is thought that the superconductivity originates in the square plane, but it is hard to isolate the behaviors of the planes.

Furthermore, the one-dimensional chains complicate the study of YBCO crystals, because as-grown crystals display many domains, separated by "twin boundaries" in which the chains run orthogonal directions. YBCO crystals may be "de-twinned" by application of pressure, for more careful studies, but many existing results on YBCO are ambiguous due to twin domains.

YBCO is not an ideal material for STM studies, because it typically cleaves on the chain plane. Very nice studies can be made of the chain planes with an STM,[24] but this is not usually thought to access the intrinsic superconducting properties of the material.

YBCO has typically been used in nuclear magnetic resonance (NMR) studies, which probe the spatial distribution of magnetic field. This is because YBCO is so well ordered that all atoms of a particular species will live in the same electronic environment (not true for BSCCO or LSCO).

$Bi_2Sr_2CaCu_2O_{8+\delta}$

Finally we come to BSCCO, the favorite material for STM and ARPES. BSCCO was discovered in 1988.[25] BSCCO itself can have one, two, or three CuO planes, where

T_c increases with the number of planes. Bismuth can also be replaced with thallium or mercury, which results in the highest T_c material known (142K).

BSCCO competes with YBCO as the most technologically useful material. YBCO has been used in magnetic field applications because it is easier to pin flux. YBCO can be used to grow high-T_c SQUIDS with grain-boundary Josephson junctions. Their higher operating temperature than conventional SQUIDs makes them useful in the study of living biological materials. BSCCO has been more useful so far in bulk applications: it has been formed into superconducting wires (with silver) and placed into the Detroit power grid, but problems in maintaining vacuum have delayed the success of this operation.

The structure of BSCCO is shown in figure 1.4(c). Surface sensitive techniques such as STM and ARPES can study BSCCO because it cleaves easily between layers, leaving an atomically flat surface for study, and, it is thought, direct tunnel access to the relevant unperturbed CuO_2 plane. However, the down-side of the easy cleavability of BSCCO is that the weak bonds make it very difficult to grow large single crystals. Therefore, magnetic experiments such as neutron scattering, which require large crystals for measurable signals, are challenging at best, and often impossible.

1.2.3 Phase Space and the Proliferation of Theories

Because these materials have three tunable parameters (temperature T, magnetic field B, and carrier concentration p), there is a vast expanse of unexplored phase space available for theoretical prediction. We already know there are at least three phases present: antiferromagnetic, superconducting, and neither. But what other phases exist, and how do they interact? For example, is antiferromagnetism competing with superconductivity or is it somehow helping? Since doping p is tunable at zero temperature, are some phases connected by quantum critical points?[26]

The more experiments published, the more hints of new phases, transitions, and quantum critical points seem to pop up, which in turn incites theorists to even more creative predictions. A sampling of the predicted phases includes:

1. resonating valance bond (RVB) state by Anderson (1987)[27]

2. staggered flux phase (SFP) by Affleck and Marston (1988);[28, 29, 30]
   later work relating to SFP as a "spin gap" phase by Wen *et al.* (1996);[31]
   and SFP in vortices by Kishine *et al.* (2001)[32]

3. stripes by Zaanen and Gunnarson (1989);[33]
   later Kivelson and Emery and Zachar (1998)[34, 35] and White and Scalapino (1998)[36]

4. multiple "stripe" and "checkers" phases of various periodicities by Löw *et al.* (1994)[37]

5. $SO(5)$ theory by S.-C. Zhang (1997)[38]

6. spin density wave (SDW) by Vojta and Sachdev (1999)[39];
   coexisting SDW + superconductivity by Demler *et al.* (2001)[40]

7. time-reversal symmetry breaking phase by Varma (2000)[41]

8. d-density wave (DDW) phase by Chakravarty *et al.* (2001)[42]

9. fractionalized nodal liquid (superconductivity without pairing) by Senthil *et al.* (2001)[43]

10. QED3 phase by Franz *et al.* (2002)[44]

11. gossamer superconductivity by Laughlin (2002)[45]

Both the staggered flux phase and the d-density wave phase may fit reasonably well with most existing data. At low energies, both the staggered flux phase[30] and the d-density wave phase[42] have the same single particle spectrum as a d-wave superconductor, so experiments which measure density of states may support the existence of SFP or DDW phases. The idea of a spin density wave phase also finds strong support from neutron scattering experiments, and almost certainly plays a key role in some areas of phase space. The quantitative predictions of Demler *et al.*[40] for coexisting SDW + superconductivity in a magnetic field are particularly well matched by elastic neutron scattering experiments.[46]

One phase which has garnered a lot of recent attention and vocal supporters is electronic "stripes", a phase in which the doped holes self-segregate into one-dimensional charge rivers spaced approximately four unit cells apart. There is no doubt that some form of stripes do exist in materials closely related to high temperature superconductors,[47] but it appears that stripes are at their strongest where superconductivity is itself suppressed. Some vehemently argue that stripes are a necessary part of the mechanism of high temperature superconductivity itself,[48] while some believe that stripes are an unrelated or even competing part of the phase diagram.

1.3 Organization of this Thesis

In this thesis, I will report on experiments we have done with a scanning tunneling microscope to elucidate the nature of the superconducting quasiparticles in $Bi_2Sr_2CaCu_2O_{8+\delta}$. From these results we can make inferences about the phases present in the material across a range of doping and magnetic field. All measurements reported in this thesis were obtained at 4.2 K and far below the upper critical field H_{c2}, so the material was always in a bulk superconducting state.

In chapter 2, I will describe the measurements one can make with a scanning tunneling microscope. The measurements reported in this thesis were all obtained with a home-built STM mounted on a high vacuum, 250 mK ^{3}He fridge, constructed by Shuheng Pan and Eric Hudson, in the Davis group at Berkeley.[49] (I have also modified this design and built a UHV-compatible STM to be used for variable temperature studies. Details of this construction can be found in Appendix C and details of the vibration environment required for proper functioning of an STM can be found in Appendix B.) In addition, I will briefly summarize some other experimental techniques, such as angle-resolved photoemission spectroscopy, neutron scattering, and nuclear magnetic resonance, which can be used to measure or infer complementary information about the density of states.

In chapter 3, I will discuss the relationship between $\vec{R}$-space and $\vec{k}$-space in BSCCO. I will describe Fourier transform scanning tunneling spectroscopy (FT-STS), or how an STM can actually access both $\vec{R}$- and $\vec{k}$-space simultaneously. FT-STS is used to investigate the nature of quasiparticles in optimally doped $Bi_2Sr_2CaCu_2O_{8+\delta}$ at 4.2 K in zero applied field. From these studies I conclude that there is no need to invoke an alternative phase to explain results in optimally doped BSCCO.

In chapter 4, I will talk about extending the search for alternative phases, using an applied magnetic field. Although H_{c2} is too large for us to destroy bulk superconductivity, we can use our local probe to investigate the modified electronic structure within a single vortex. Here we find a periodic modulation of the electronic density of states which may signify the onset of a new phase.

In chapter 5, I will talk about extending the search for alternative phases into the underdoped side of the phase diagram. Although extremely underdoped crystals are not available for bulk studies, I will give brief evidence for inhomogeneity in underdoped samples, which enables access to nanoscale patches of far underdoped regions of phase space. I will describe the use of both intentionally introduced impurities and native defects to probe the electronic structure of the far underdoped phase.

Finally, I conclude that although no alternative phases are needed to explain the behavior of $Bi_2Sr_2CaCu_2O_{8+\delta}$ at low temperature, zero magnetic field, and optimal doping, there are definitely some interesting phases lurking just away from optimal doping along all three axes of phase space. The use of STM as a local probe has enabled me to obtain information about two directions in phase space (low doping and high field) for which bulk samples are currently unavailable. In both cases, I find evidence for a starkly different electronic structure than the simple d-wave superconducting order.

Forty-six years elapsed between the original discovery of low-temperature superconductivity in 1911 and its explanation by BCS in 1957. Maybe by the year 1986 + 46 = 2032 there will be enough experimental information available for a brilliant trio of scientists to present an underlying theory for these even more complex high-T_c materials.

Figure 1.5: Perhaps the future solvers of high-temperature superconductivity are somewhere in this crowd. (Photo taken at the first International Conference on Women in Physics in Paris, France in 2002, attended by more than 250 women physicists from around the world.)

Chapter 2

Materials and Techniques

This thesis documents the use of a scanning tunneling microscope (STM) to study the high temperature superconductor $Bi_2Sr_2CaCu_2O_{8+\delta}$ (BSCCO). This chapter introduces both the material BSCCO, and the scanning tunneling microscope which can be used to measure its density of states. I also explain the relationship between STM and several other experimental techniques, such as angle-resolved photoemission spectroscopy, neutron scattering, and nuclear magnetic resonance, which can be used to measure or infer complementary information about the density of states.

2.1 $Bi_2Sr_2CaCu_2O_{8+\delta}$

We choose to study BSCCO with our STM, because BSCCO has weak bonds between the two BiO layers, so it can be easily cleaved to achieve an atomically flat surface. The structure of BSCCO is shown in figure 2.1(a).

Because an STM rasters a sharp tip within a few Ångstroms of the sample surface, it is essential that the surface be atomically flat. One loose atom on the surface could hop to the tip and cause the tip to become energetically unstable. The atom will flop around in several closely spaced energy states so that no further useful information can be obtained from the sample surface because it is swamped by spurious effects from the tip. The following are two requirements for STM study of a surface: (1) The surface must cleave exactly between layers, leaving no residual chunks of a mostly missing layer. (2) The surface must be free from other contaminants, for example helium or water molecules which may land on it.

To achieve a satisfactory surface, we cleave the BSCCO sample while it is surrounded

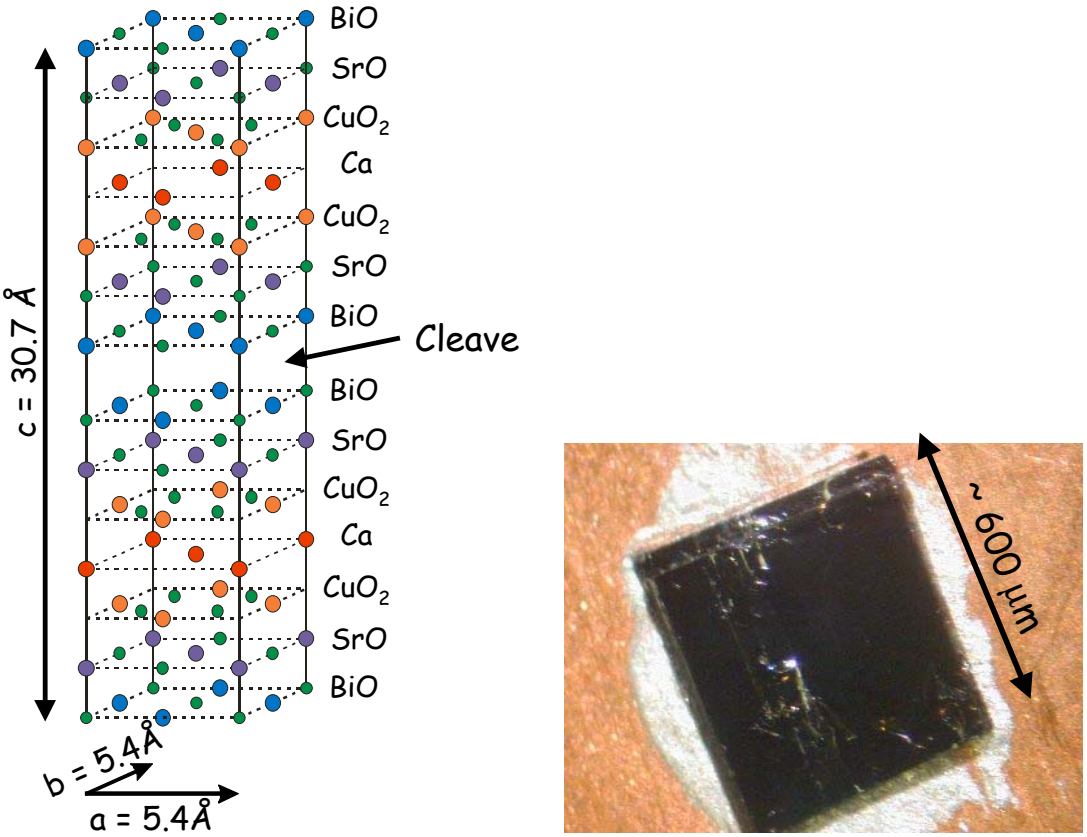

(a) (b)

Figure 2.1: (a) Chemical structure of $Bi_2Sr_2CaCu_2O_{8+\delta}$. The sample cleaves easily between the two BiO layers, and we image the exposed BiO layer. Note that two layers beneath every Bi atom (blue) lies a Cu atom (orange). (b) Photograph of a cleaved BSCCO sample, glued with conducting epoxy to a copper sample holder. The samples we use are typically ∼1 mm square and ∼10s of μm thick.

by a cryogenic UHV environment. Cleaving is mechanically simple. First we glue a small sample to the copper sample holder, then we glue a small rod to the other side of the sample. When the whole setup has been inserted into the correct cryogenic UHV environment, we knock the rod off, and it splits the BSCCO sample in two, exposing an uncontaminated surface. A photo of a cleaved surface (after the experiment, now sitting in air) is shown in figure 2.1(b). The rod is typically knocked off by swinging another rod perpendicular to it just before the sample is inserted into the STM.

In practice, there are many details, such as use of the correct glue to avoid cracking when exposed to cold temperatures, or shattering the BSCCO due to differential thermal contraction. The temperature may also vary: BSCCO may be cleaved in a cryogenic UHV

environment without itself actually being at a cryogenic temperature, if it is suspended from a hot rod to room temperature. Another variable is the speed at which the cleaving occurs. No controlled tests have been carried out, but the speed of cleaving must influence the local temperature at the cleaved surface, and could in the future be tuned to increase the success rate of cleaves.

One concern is whether the violent act of cleaving locally heats the surface and/or causes some kind of surface redistribution. It is apparent from topographic measurements that the bismuth atoms remain ordered as expected upon cleaving, but is possible that this violent action has some effect on the redistribution of the oxygen dopant atoms, which are so far invisible to STM.

The related technique of angle-resolved photoemission spectroscopy (ARPES) is not as surface sensitive as STM, but it is still somewhat surface sensitive. A surface reconstruction resulting in different electronic surface states would prevent ARPES from seeing the true bulk density of states. However, a few unwanted junk molecules on the surface, or a flaky or terraced cleave, would probably not preclude a good ARPES measurement, as they would preclude any kind of STM measurement.

Therefore, at the present time, BSCCO is the preferred material for study by STM and ARPES, although ARPES has successfully studied many other HTSC materials, and even STM is starting to branch out as more reproducible cleaving recipes are slowly figured out for other materials.

The BSCCO crystals studied in this thesis were grown by the floating zone method with superconducting transition temperatures ranging between underdoped (T_c = 65 K) and slightly overdoped (T_c = 85 K). The samples are cleaved at the BiO plane in cryogenic ultra high vacuum and immediately inserted into the STM head.

If all the interesting interactions of the superconductivity are thought to occur in the CuO plane, one might ask why are we satisfied with studying the BiO plane? Two layers beneath the BiO plane is the CuO plane. So in order to access the CuO plane, we need to tunnel through the BiO and SrO planes. Luckily, it is thought that both of these planes are insulating (or at least semi-conducting with a large gap)[50] so they can be treated as an extension of the vacuum tunneling barrier. In fact, their presence on top of the CuO layer of interest may be a blessing in disguise, because they protect the oxygen dopant atoms on *both* sides of the CuO plane, and thus preserve the charge carrier concentration in the CuO plane. If the top BiO layer were removed in the act of cleaving, the CuO plane would likely lose half of its charge carriers.

2.2 Scanning Tunneling Microscopy

The scanning tunneling microscope was invented in 1982 by Binnig and Rohrer,[51] for which they shared the 1986 Nobel Prize in Physics. The instrument consists of a sharp conducting tip which is scanned with respect to a flat conducting sample. When a voltage V is applied between tip and sample, a current will flow, and this current can be measured as a function of (x, y) location and as a function of V. This is illustrated schematically in figure 2.2.

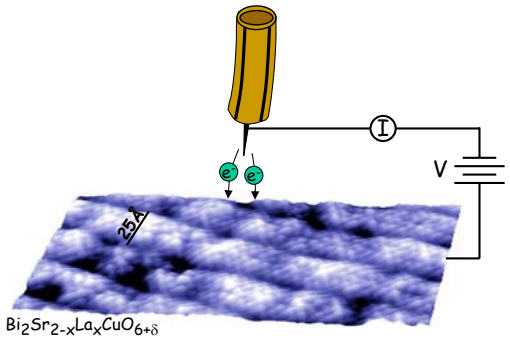

Figure 2.2: Schematic of STM tip and sample. The tunneling current I is measured as the sample bias voltage V and/or the (x, y) position of the tip are varied.

2.2.1 Calculation of Tunneling Current

The current which flows between the tip and the sample can be calculated by time-dependent perturbation theory. If the sample is biased by a negative voltage $-V$ with respect to the tip, this effectively raises the Fermi level of the sample electrons with respect to the tip electrons. Electrons will tend to flow out of the filled states of the sample, into the empty states of the tip. This situation is illustrated in figure 2.3. The elastic tunneling current from the sample to the tip for states of energy ε (with respect to the Fermi level of the sample) is:

$$I_{\text{sample}\to\text{tip}} = -2e \cdot \frac{2\pi}{\hbar}|M|^2 \underbrace{(\rho_s(\varepsilon)\cdot f(\varepsilon))}_{\substack{\#\text{ filled sample states} \\ \text{for tunneling from}}} \underbrace{(\rho_t(\varepsilon+eV)\cdot[1-f(\varepsilon+eV)])}_{\substack{\#\text{ empty tip states} \\ \text{for tunneling to}}} \tag{2.1}$$

where the factor of 2 out front is for spin, $-e$ is the electron charge (we are tunneling single electrons, not quasiparticles or Cooper pairs), $2\pi/\hbar$ comes from time-dependent perturba-

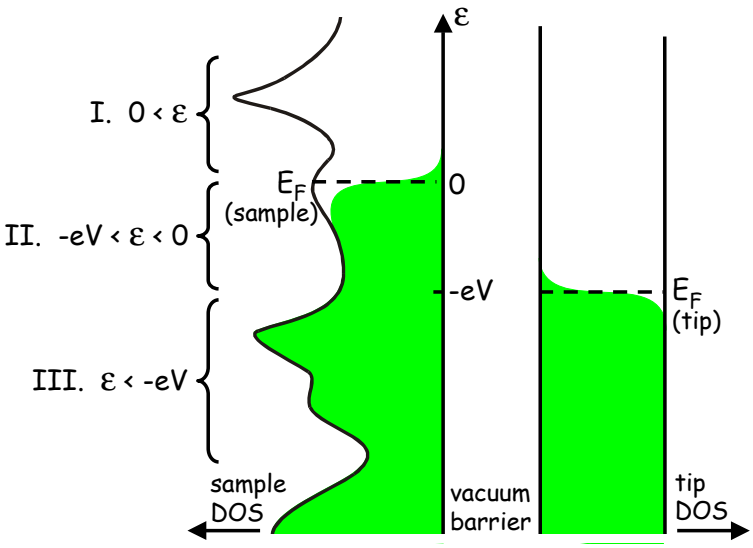

Figure 2.3: Schematic of tip-sample tunneling. Energy is along the vertical axis, and density of states of the sample and tip are shown along the horizontal axes. Filled states are shown in green. In this case, a negative bias voltage $-V$ has been applied to the sample, which effectively raises its Fermi level by eV with respect to the Fermi level of the tip. This allows for filled states on the left (sample) to tunnel into empty states on the right (tip). The tunneling current is measured by an external circuit.

tion theory, $|M|^2$ is the matrix element, $\rho_{s(t)}(\varepsilon)$ is the density of states of the sample (tip), and $f(\varepsilon)$ is the Fermi distribution:

$$f(\varepsilon) = \frac{1}{1 + e^{\varepsilon/k_B T}} \tag{2.2}$$

Though the dominant tunneling current for negative sample voltage $-V$ will be from sample to tip, there will also be a smaller tunneling current of electrons from tip to sample:

$$I_{\text{tip}\to\text{sample}} = -2e \cdot \frac{2\pi}{\hbar} |M|^2 \underbrace{(\rho_t(\varepsilon + eV) \cdot f(\varepsilon + eV))}_{\substack{\#\text{ filled tip states} \\ \text{for tunneling from}}} \underbrace{(\rho_s(\varepsilon) \cdot [1 - f(\varepsilon)])}_{\substack{\#\text{ empty sample states} \\ \text{for tunneling to}}} \tag{2.3}$$

When we sum these, and integrate over all energies ε, we arrive at the total tunneling current from sample to tip:

$$I = -\frac{4\pi e}{\hbar}\int_{-\varepsilon_F(\text{tip})}^{\infty} |M|^2 \rho_s(\varepsilon)\rho_t(\varepsilon+eV)\left\{f(\varepsilon)\left[1-f(\varepsilon+eV)\right]-\left[1-f(\varepsilon)\right]f(\varepsilon+eV)\right\}d\varepsilon \tag{2.4}$$

We can simplify this expression in several ways. First, all measurements reported in this thesis were taken at $T = 4.2$ K. At this low temperature, the Fermi function cuts off very sharply at the Fermi surface, with a cutoff width of $k_BT = 0.36$ meV. (For reference, the width of the band in BSCCO is several eV, and many of the features studied in this thesis have widths on order several meV.)

In the approximation of a perfectly abrupt cutoff, the integral breaks into 3 parts (where ε is still referenced to the Fermi surface of the sample):

I. $\underline{0 < \varepsilon}$

$$\begin{aligned} &f(\varepsilon) \approx 0; \quad f(\varepsilon+eV) \approx 0 \\ &\Rightarrow f(\varepsilon)\left[1-f(\varepsilon+eV)\right]-\left[1-f(\varepsilon)\right]f(\varepsilon+eV) \approx 0\cdot 1 - 1\cdot 0 = 0 \end{aligned} \tag{2.5}$$

II. $\underline{-eV < \varepsilon < 0}$

$$\begin{aligned} &f(\varepsilon) \approx 1; \quad f(\varepsilon+eV) \approx 0 \\ &\Rightarrow f(\varepsilon)\left[1-f(\varepsilon+eV)\right]-\left[1-f(\varepsilon)\right]f(\varepsilon+eV) \approx 1\cdot 1 - 0\cdot 0 = 1 \end{aligned} \tag{2.6}$$

III. $\underline{\varepsilon < -eV}$

$$\begin{aligned} &f(\varepsilon) \approx 1; \quad f(\varepsilon+eV) \approx 1 \\ &\Rightarrow f(\varepsilon)\left[1-f(\varepsilon+eV)\right]-\left[1-f(\varepsilon)\right]f(\varepsilon+eV) \approx 1\cdot 0 - 0\cdot 1 = 0 \end{aligned} \tag{2.7}$$

Therefore, the relevant range of ε over which we must integrate to find the tunneling current is reduced to $-eV < \varepsilon < 0$. (Likewise, if we had applied a positive bias voltage V to the sample, our range of integration would be $0 < \varepsilon < eV$.) So we are left with approximately:

$$I \approx -\frac{4\pi e}{\hbar}\int_{-eV}^{0} |M|^2 \rho_s(\varepsilon)\rho_t(\varepsilon+eV)d\varepsilon \tag{2.8}$$

In reality equation 2.8 will be modified by an apparent smearing of energy features with $\approx k_BT$ width.

Second, we pick a tip material which has a flat density of states within the energy range of the Fermi surface that we wish to study. For example, if we wish to study the sample density of states within 200 meV of the Fermi surface, then the measured tunneling current will be a convolution of the density of states of the tip and sample in this energy range. So we pick a tip material which has a flat density of states in this range, so that $\rho_t(\varepsilon + eV)$ can be treated as a constant and taken outside the integral.

$$I \approx \frac{4\pi e}{\hbar}\rho_t(0)\int_{-eV}^{0}|M|^2\rho_s(\varepsilon)d\varepsilon \tag{2.9}$$

In practice, most of the measurements reported in this thesis were taken with a tungsten tip, sharpened in situ by field emission onto a gold surface. Tungsten is thought to have a flat density of states near its Fermi surface. As an extra check of this assumption, one can verify that density of states spectra taken with a tungsten tip are flat from -200meV to +200meV at a number of locations on the gold surface (because gold definitely has a flat density of states in this energy range). Other common tip materials include Pt and PtIr.

Bardeen first laid out a basic theory for vacuum tunneling in 1961.[52] Perhaps most importantly, he showed that under the realistic assumptions that (1) the tip and the sample each have their own independent density of states, (2) each of their wavefunctions fall exponentially to zero in the tunneling barrier, and (3) the overlap is small enough (i.e. tip-sample separation is large enough) that each side is insignificantly influenced by the tail of the wavefunction from the other side, then the matrix element for tunneling will be virtually independent of the energy difference between the two sides of the barrier. The matrix will remain unchanged even if one side transitions from the normal state to the superconducting state. In other words, to a reasonable approximation, we can take the matrix element outside the integral and treat it as a constant. Cohen *et al.* in 1962 reformulated this tunneling theory in a slightly easier to read fashion, in terms of a tunneling Hamiltonian.[53]

$$I \approx \frac{4\pi e}{\hbar}|M|^2\rho_t(0)\int_{-eV}^{0}\rho_s(\varepsilon)d\varepsilon \tag{2.10}$$

But what is $|M|^2$? The matrix element comes from the assumption that both tip and sample wavefunctions fall off exponentially into the vacuum gap. Basically, we assume that the vacuum barrier is a square barrier, and we do a WKB approximation. In reality, there will be some tilt to the top of the barrier, but the tilt will be the applied voltage (on order 100 meV) while the height of the barrier will be on order the energy required to remove an electron from a metal, i.e. the work function, of several eV. Therefore, the tilt of the barrier

will be much smaller than the height of the barrier, and can be ignored.

WKB says that the tunneling probability through a square barrier will be $|M|^2 = e^{-2\gamma}$ with γ given by:

$$\begin{aligned} \gamma &= \int_0^s \sqrt{\frac{2m\varphi}{\hbar^2}} dx \\ &= \frac{s}{\hbar}\sqrt{2m\varphi} \end{aligned} \tag{2.11}$$

where m is the mass of the electron, s is the width of the barrier (tip-sample separation), and φ is the height of the barrier, which is actually some mixture of the work functions of the tip and sample.

We can measure the work function by recording the tunneling current as a function of tip-sample separation.

$$I \propto e^{-2s\sqrt{2m\varphi}/\hbar} \tag{2.12}$$

Therefore, we can measure φ from the slope of $\ln I$ vs. s. Typically, we find $\varphi \approx$ 3-4 eV. The higher φ, the more the tunneling current will vary for a given change in s, therefore a higher φ gives a better resolution tip.

Lang made specific calculations in 1987 with a Na atom tip,[54] to show the crossover regime between point contact (where we expect Bardeen's assumptions to break down and universal conductance phenomena to dominate) and vacuum tunneling, where we expect wavefunctions on either side to fall off exponentially. He found for the simplest-to-calculate case of a sodium atom on the end of the tip, this crossover regime occurs around 5-8 Å (nuclear distance between closest tip and sample atoms).

Empirically, our tunneling experiments are occurring in the exponential regime, so we may guess that nucleus-to-nucleus tip-sample separation s exceeds 8 Å. However, due to the exponential fall-off, we have no way of measuring the absolute value of s. This at times causes us much grief, because there is no way to know for sure if we are making measurements at a constant tip-sample separation. So if we see variation from one point on the sample surface to another, we can't be sure whether the variation is due to intrinsic inhomogeneities in the sample at the specific energy of measurement, or due to a varying tip-sample separation.

In summary, the tunneling current is fairly well approximated by:

$$I \approx \frac{4\pi e}{\hbar} e^{-s\sqrt{\frac{8m\varphi}{\hbar^2}}} \rho_t(0) \int_{-eV}^{0} \rho_s(\varepsilon) d\varepsilon \tag{2.13}$$

2.2.2 Measurement Types

Our STM holds the tip at virtual ground, and applies a bias voltage to the sample. The tunneling current is measured from the tip. The tip sits at the end of a piezo tube scanner (with 4 quadrants $\pm x$ and $\pm y$ on the outside, and a single electrode for z on the inside), which can control its motion with sub-Ångstrom precision in 3 directions. The voltage output to the scanner is ± 220 V, with a 16-bit DAC, which is sent through a simple RC filter with rolloff around 3 kHz, to remove high frequency noise leaking out from the electronic control unit. This gives a bit size of $440V/2^{16} \sim 6.7$ mV and a spatial control resolution of approximately 0.03 Å at 4.2K (with a 200 nm total scan range).

We can measure tunneling current as a function of 4 variables: x, y, z, and V. In practice, we attempt to keep z constant by employing a feedback loop to keep the tunneling current constant at a fixed bias voltage. Assuming that z is constant, we then take measurements as a function of x, y, and V.

Topography

The most common mode of STM measurement employed by STM groups around the world is a topography. In this mode, we raster the tip across the surface at a fixed sample bias voltage $-V_{\text{set}}$, and employ a feedback loop which controls the voltage on the z piezo to keep the tunneling current constant at I_{set}. By recording the voltage to the z piezo, we can effectively map the height of the surface.

It's actually not clear what we mean by the "height" of the surface. One obvious suggestion would be some contour of constant charge density. However, as we can see from equation 2.13, the tunneling current does not depend on the total charge density, but only the charge density within eV below the Fermi surface, where $-V$ is the applied bias voltage.

One might argue then that we should apply an arbitrarily large voltage so that we can capture more of the charge density, but we then run into two problems: (1) BSCCO is a fragile compound with weak bonds, and if we apply a large voltage locally, pieces of the surface will literally rip off. (2) If V is too high (on order φ), our tunneling approximation breaks down.

So we are stuck with this somewhat arbitrary definition of the "height of the surface" as the tip-sample separation for which tunneling current is fixed at a particular constant value I_{set} for a particular applied bias voltage V_{set}. In practice we usually choose to fix the current at -100 pA, for a bias voltage of -100 mV. This is arbitrary, but gains some validity from the fact that we do see atoms and other structural features as expected, even over a wider range of choices of I_{set} and V_{set}. The most widely varying density of states features of our BSCCO samples seem to be within 75 meV of the Fermi level.

Density of states

From equation 2.13 we see that if we hold the tip-sample separation constant, at a given (x, y) location, and put a negative bias voltage $-V$ on the sample, we have:

$$I = I_0 \int_{-eV}^{0} \rho_s(\varepsilon) d\varepsilon \tag{2.14}$$

In other words, we can measure the integral of the density of states, down to any energy $-eV$, by varying $-V$. Note that for a negative bias voltage on the sample, we are tunneling electrons from sample to tip, and we are measuring the integrated density of full states below the Fermi level in the sample. For a positive bias voltage on the sample, we are tunneling electrons from tip to sample, and we are measuring the integrated density of empty states above the Fermi level in the sample.

OK, that's nice, we have the integrated density of states (IDOS). But it would be much nicer to just have the density of states (DOS). After acquiring an IDOS vs. V curve, we could take a numerical derivative of our data to get the DOS. But taking a derivative numerically is a horribly noisy thing to do. It is much better to measure the derivative directly.

So we employ a lock-in amplifier to modulate the bias voltage by dV (typically a few mV) around a voltage V of interest. As a result of the voltage modulation dV we can measure a current modulation dI at the same frequency. We call this dI/dV the conductance $g(V)$. Now, we can write:

$$g(V) \equiv \frac{dI}{dV} \propto \text{DOS}(eV) \tag{2.15}$$

Therefore, by using a lock-in and varying V, we can map out an entire density of states curve.

The energy resolution is limited by the amplitude of the wiggle (until the modulation becomes less than $\approx k_B T = 0.36$ meV). So ideally, we could make the voltage modulation smaller than 0.36 mV. But in practice, we can't get enough signal-to-noise at this low amplitude without prohibitively long averaging times. Most of the data reported in this thesis was measured with a 2 mV RMS modulation, therefore blurring our energy resolution by approximately 5.6 meV.

Linecut

In the previous section, we discussed a single DOS curve at a single location. Since we have (x, y) control over the location of our tip using the piezo tube scanner, we can measure DOS curves anywhere we want. Some samples, like good metals (without impurities), should have a completely homogenous DOS everywhere.

But some more interesting samples, for example BSCCO, are inhomogeneous. For example, we can measure a full DOS curve at every point along a straight line, spaced a few Å apart, and we see a "linecut".

DOS map

What we have discussed so far is a 3-dimensional data set: 2 spatial dimensions x and y (by varying the position of the tip) and 1 energy dimension (by varying V). We can view this 3-dimensional data set as a series of DOS-vs-energy curves at every location (x, y), or we could view it as a series of 2-dim DOS-maps at each energy eV. Mapping the DOS at a specific energy is a good visual way to see the inhomogeneities in the density of states. The various ways of viewing the STM measurements are shown in figure 2.4.

Most of the action in the density of states due to the superconducting gap happens within the energy range -100 meV to +100 meV. Most energy features, for example due to impurity resonances, have widths on order a few meV. So in order to get a good picture of the density of states, a minimal spectra has 101 points, which gives 2 meV energy resolution from -100 meV to +100 meV.

The high temperature superconductors have a short coherence length, $\xi \sim 10 - 20$ Å. Therefore, the density of states may be changing significantly on this short length scale. So in order to capture spatial variations in the density of states, we require spatial resolution at least one pixel per 5 Å.

Therefore, for a minimal survey of the density of states in a ~ 500 Å square area, we

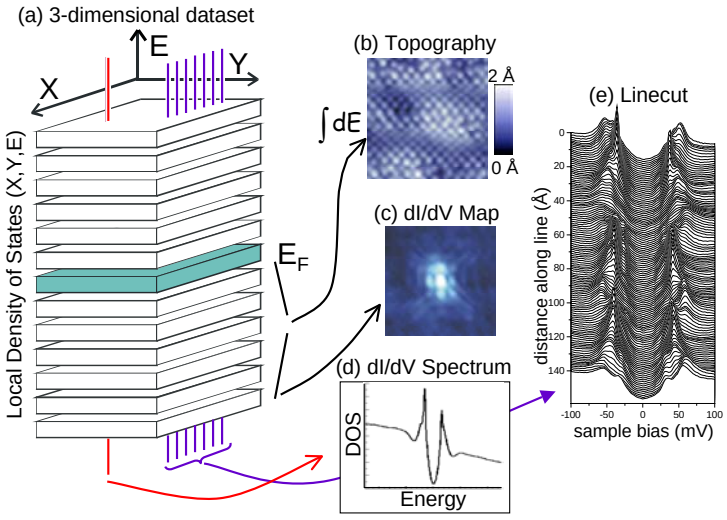

Figure 2.4: (a) An STM has access to an essentially 3-dimensional dataset: two spatial dimensions (x, y) and energy E. This 3-dimensional data space can be explored in 4 different ways (b)-(e). (b) Topography: the tip height z is adjusted through a feedback loop to maintain a constant current I_{set} at a constant bias voltage V_{set}; recording the tip height effectively maps out the height of the surface. (c) dI/dV map: the density of states at a fixed energy E is mapped as a function of position (x, y) on the sample surface. (d) dI/dV spectrum: the density of states as a function of energy is measured at a single point on the sample surface. (e) Linecut: the density of states as a function of energy is mapped at several points along a line on the sample surface.

require 101 (energy) $\times$ 128 $\times$ 128 (spatial), or greater than 10^6 measurements! Even at a meager 100 ms per measurement, such a DOS map requires almost 48 hours. Even making a single measurement in 100 ms is no small feat, because each measurement requires changing the DC bias to a new value V, modulating a small AC bias dV on top, and locking in to the new dI, which necessarily takes several frequency cycles to stabilize after the change in DC bias V. The AC modulation frequency for maps is typically $\sim$ 1.1 kHz, and other carefully optimized parameters such as ramp time, wait time, and measurement averaging time can be found in Eric Hudson's PhD thesis.[55]

Of course, a more detailed DOS map with higher spatial resolution for identification of smaller features (such as short wavelength DOS standing waves, or impurity resonances) may require 101 (energy) $\times$ 512 $\times$ 512 (spatial) measurements, which takes 16 times longer. Therefore the spatial registry must remain locked in place for up to a month (spanning multiple tip retractions for liquid helium transfers)!

2.2.3 Noise Considerations

Vibration Noise

Vibration noise can affect the STM measurement two ways: (1) change in the tip-sample separation, which is amplified exponentially in the tunneling current, and (2) motion of the wire carrying the tip current, which capacitively couples to its environment and therefore causes current spikes when moved. The latter issue can be addressed by carefully clamping all of the wires in place, so that they cannot move with respect to each other due to helium boiling vibrations or external building vibrations. Measurement of external building vibration noise is discussed in more detail in Appendix B.

Electronic Noise

In practice, after fastidious attention to vibration isolation, the largest source of noise is electronic noise. The current preamplifier has a gain of 10^9 which means that the op-amp has a feedback resistor of 1 GΩ. The Johnson noise at room temperature is $0.13\sqrt{R(\Omega)}\text{nV}/\sqrt{\text{Hz}} = 4.11\mu\text{V}/\sqrt{\text{Hz}}$.

In topographic mode, we are essentially integrating over a 3 kHz bandwidth, which amounts to 0.23 mV of rms noise. This is only 0.23 pA of effective current noise, which is generally not a problem in topographic mode where our setpoint current is typically $I_{\text{set}} =$ 100 pA.

In dI/dV mode, the effect of the noise is limited to a band around the frequency of bias voltage modulation. Typically the effective width of this band with feasible averaging times is $\sim$ 100 Hz. The rms voltage noise is therefore 41 μV which means an effective minimum current noise of only 0.04 pA. In fact, due to other imperfections in the electronics, the current noise can be somewhat higher than this. When attempting to measure small features in the density of states, this can be a significant problem.

This current noise could be improved by putting the current preamplifier down on the fridge at 4.2 K. Then the Johnson noise would be reduced by a factor $\sqrt{300\text{K}/4\text{K}} = 8.66$.

Capacitive Coupling

Our STM holds the tip at virtual ground, and applies a bias voltage to the sample. The tunneling current is measured from the tip. Many successful STMs instead bias the tip and measure the tunneling current from the sample. However, the current measurement is

the most sensitive part of the whole operation, and most subject to noise from capacitive pickup. It is necessary to shield the current-measurement side with a ground plane from as many angles as possible, for example to prevent capacitive pickup from the high and rapidly sweeping voltages on the scan piezo. Since the tip is more geometrically compact than the sample (& attached sample holder), and thus easier to shield, it seems logistically easier to bias the sample and measure the tip current.

2.2.4 Inhomogeneity in $\vec{R}$-space vs. Anisotropy in $\vec{k}$-space

An STM is an excellent tool for measuring the density of states as a function of position with sub-Å resolution. Real-space resolution is important for the study of BSCCO in the following experiments: quasiparticle scattering imaging (discussed in chapter 3), magnetic vortex imaging (discussed in chapter 4), and impurity imaging (discussed in chapter 5).

But what about momentum space?

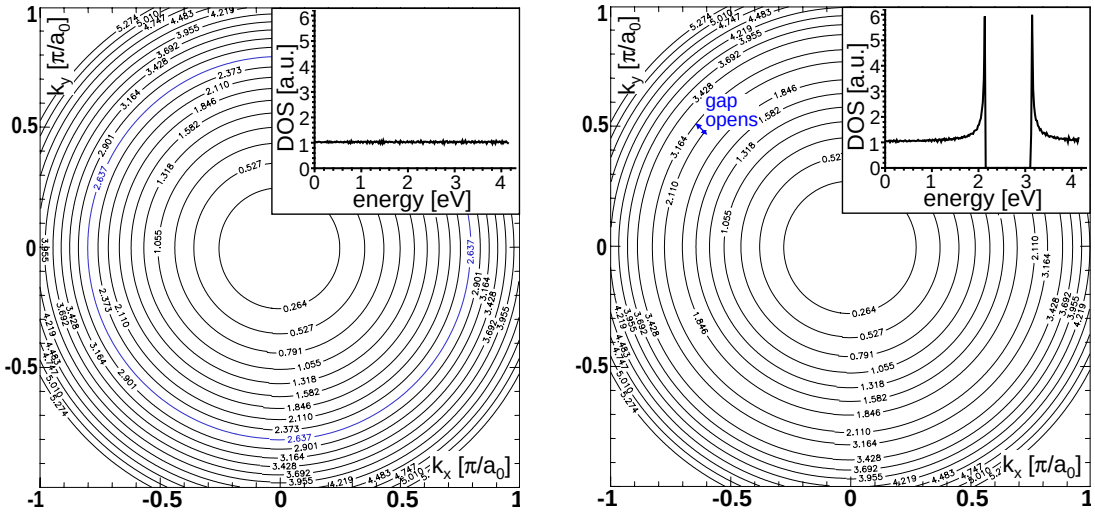

(a) Normal state.

(b) Superconducting state (Δ = 500 meV).

Figure 2.5: Isotropic band structure and density of states for a hypothetical perfect s-wave superconductor. (a) The blue line shows the Fermi surface in the normal state. (b) The Fermi surface is completely gapped in the superconducting state. The magnitude of the superconducting gap, $\Delta = 500$ meV, has been exaggerated for visual clarity. The density of states curves shown in the insets are calculated by numerical integration from the band structure contour maps.

An STM tip collects (emits) electrons from (to) all directions in the sample indiscriminately. Therefore, the DOS curves measured by an STM are an average over $\vec{k}$-space.

Why do we care? For many materials, we don't. For example, a conventional low-temperature superconductor has an isotropic s-wave order parameter. This means that the electrons bound into Cooper pairs have an isotropic wave function. They don't care which direction they're traveling; they still see the same binding energy. The energy landscape in the first Brillouin zone for an ideal isotropic s-wave superconductor in the normal and superconducting states (with an exaggerated large gap for clarity) is shown in figure 2.5. The corresponding density of states (found by numerical integration over the contour map) is shown in the insets. When we drop into the superconducting state, we merely push the contours of constant energy (circles) closer together at the Fermi level. The contour corresponding to the Fermi level itself disappears; there are no more states at that energy due to the opening of the superconducting gap. The density of states is the same in every direction; i.e. no matter which direction $\hat{k}$ we take a cut out from zero energy in the center, we see the same thing.

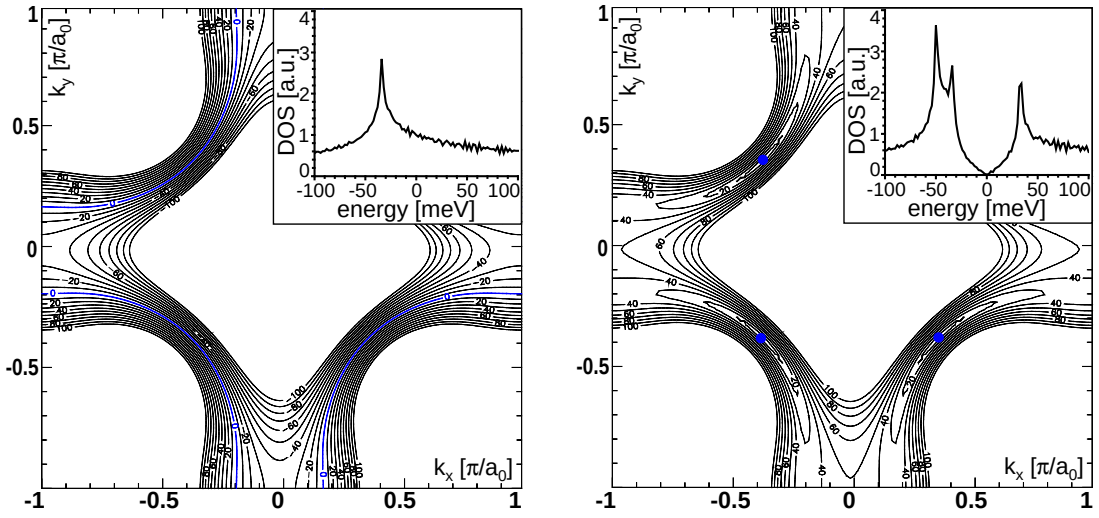

(a) Normal state.

(b) Superconducting state ($\Delta = 36$ meV).

Figure 2.6: Anisotropic band structure and density of states for BSCCO, a $d_{x^2-y^2}$-wave superconductor. The blue line shows the Fermi surface in the normal state (a); the Fermi surface is gapped in the superconducting state (b) except for four nodal points, shown as blue dots. The band structure and magnitude of the superconducting gap $\Delta = 36$ meV are realistic for optimally doped BSCCO. The density of states curves shown in the insets are calculated by numerical integration from the band structure contour maps.

However, BSCCO is a d-wave superconductor; the bound electrons in the Cooper pairs have d-wave, four-fold symmetry. This means that the energy landscape is different in different directions. Figure 2.6 shows the energy landscape of BSCCO in the normal state and in the superconducting state.

In BSCCO, an electron entering the tip from one direction may see a 10 meV square gap, while an electron entering from another direction may see a 30 meV square gap. What we measure with an STM is a sum of all these processes from every direction. The average of all the square gaps gives us a V-shaped gap. Therefore, each individual STM spectrum forfeits the $\vec{k}$-space information. The BSCCO cross-shaped energy landscape in $\vec{k}$-space shown in figure 2.6 was actually deduced from angle-resolved photoemission (ARPES), not from STM.

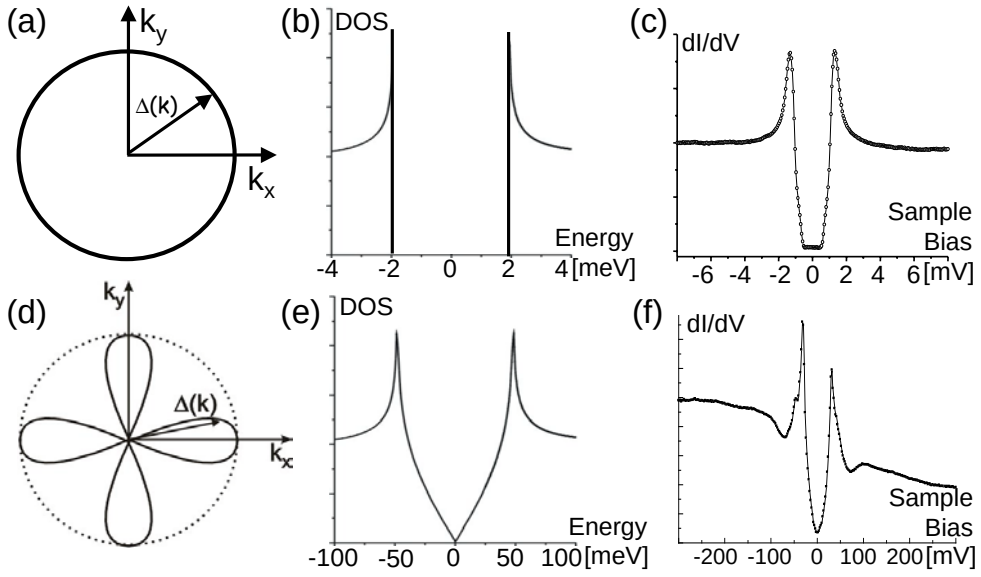

Figure 2.7: Demonstration of the density of states, as seen by an STM, averaged over $\vec{k}$ for s-wave and d-wave superconductors. (a) Gap $\Delta(\vec{k})$ is constant as a function of angle for an s-wave superconductor. (b) Therefore when the STM averages over angle, the resultant density of states still shows a square gap. (c) Real data:[49] density-of-states spectrum on s-wave superconductor $NbSe_2$. The imperfection of the square gap is due in part to thermal broadening, and in part to the very slight anisotropy in the $NbSe_2$ s-wave gap. (d) Gap $\Delta(\vec{k})$ is angle-dependent for a d-wave superconductor. (e) Therefore, when the STM averages over angle, it combines square-gapped spectra with all different values of Δ, and the resultant average shows a V-shaped gap. (f) Real data: typical density-of-states spectrum on d-wave superconductor BSCCO.

2.3 Other Experimental Techniques

There are many other experimental techniques which provide complementary information about the cuprates. In order to better understand the relevant results of these experiments, I will summarize the basic techniques here.

2.3.1 Angle-Resolved Photoemission Spectroscopy

ARPES is a technique for measuring the DOS of a sample with momentum resolution instead of spatial resolution. ARPES takes advantage of the photoelectric effect: shoot in photons with a well known energy, then measure the direction and energy of the emitted electrons. A schematic of the experiment geometry (courtesy of Z.-X. Shen) is shown in figure 2.8. Conservation of energy and momentum allows reconstruction of the energy-momentum relation (dispersion relation) of the electrons within the crystal.

$$E_{\text{kin}} = h\nu - \phi - |E_B| \tag{2.16}$$

$$\vec{p}_{\|} = \hbar\vec{k}_{\|} = \sqrt{2m_e E_{\text{kin}}}\sin\vartheta \tag{2.17}$$

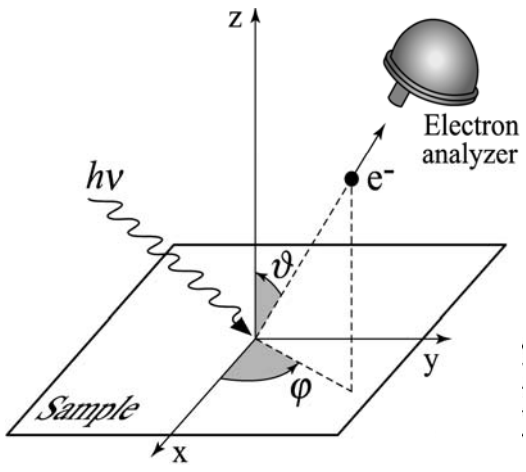

Figure 2.8: Angle-resolved photoemission spectroscopy (ARPES) experimental geometry. Figure borrowed from Damascelli *et al.*[56] The incoming photon has significant energy $h\nu$ but negligible momentum. The energy and momentum of the outgoing electron are measured with a high-resolution Scienta detector (the hemisphere shown).

A few caveats:

(1) ARPES works well only on 2-dimensional materials. If the electrons in the material are moving around with an unknown z component to their momentum as well as the x and y components, then it is impossible to reconstruct the dispersion relation: there are too few measurables, and too many variables.

(2) ARPES spatially averages. Therefore, all of the compelling reasons for studying the spatial dependence of BSCCO DOS (such as electronic inhomogeneity, vortices, and impurities) are unaddressed. Spatial averaging can also create apparent spurious effects in the data. For example, suppose we had some short-length-scale segregation between two different phases. Suppose that one phase had a narrow gap width with sharp coherence peaks, while the other had a wide gap with rounded gap-edge peaks. If we spatially average, we will come up with an intermediate spectrum that looks nothing like any true spectrum in the crystal.

Spatially averaging can be deceiving in more subtle ways. Suppose we have a continuous distribution of gap widths Δ, each with sharp coherence peaks. But if we spatially average, we will arrive at a spectrum with broader coherence peaks. The width of the coherence peak is inversely proportional to the quasiparticle lifetime. So an ARPES measurement on an inhomogeneous surface could give a false impression of a very short quasiparticle lifetime. But ARPES experiments on BSCCO do see long quasiparticle lifetimes in some parts of $\vec{k}$-space and short quasiparticle lifetimes in other parts.

(3) ARPES measures only filled states (i.e. states with $\varepsilon < \varepsilon_F$), not empty states above the Fermi level. This is because ARPES measures only photo-ejected electrons; an electron can only be ejected at a certain energy if there was a filled state in the crystal at the corresponding energy to begin with. Unlike STM, ARPES cannot measure empty states by reversing the process and putting electrons back into the sample.

(4) ARPES cannot work in a magnetic field, because it depends on the ejected electrons traveling in a straight line from the sample to the detector at the angle of interest.

Fermi surface

Despite these caveats, ARPES has been tremendously successful at mapping out the Fermi surface of many 2-dimensional materials, such as high-T_c superconductors, by measuring number of ejected electrons vs. energy at many different detector angles.

What ARPES actually measures is the spectral function $A(\vec{k}, \omega)$ times the Fermi func-

tion $f(\omega)$ times some matrix element $I_0(\vec{k}, \nu, A)$ which may have some $\vec{k}$ and A dependence and also some dependence on ν, the energy of the incoming photon. A more detailed discussion of the ARPES matrix element may be found in a comprehensive review of ARPES on high-T_c superconductors by Damascelli *et al.*[56] In practice, ARPES experiments typically make measurements at several different incoming photon energies and polarizations, to verify that any effects they may be seeing are not dependent on a specific incoming photon energy $h\nu$. As for matrix-element dependence on $\vec{k}$ and A, several approximations show these should not be so large as to overwhelm the useful $A(\vec{k}, \omega)$ information.

For our purposes, we note that both STM and ARPES have matrix elements which may influence experimental results. But the important point is that the matrix elements have totally different physical origins and totally different forms and dependencies for the two experiments. So if the same result can be found from both STM and ARPES, then we can probably conclude that the matrix elements are not affecting our ability to extract the density-of-states information from either experiment.

So let's assume ARPES is just measuring the spectral function times the Fermi function. By measuring this spectral function along a line in $\vec{k}$-space which crosses the Fermi surface, they will see a peak in emitted electron intensity which disperses towards the Fermi level, then disappears as $\vec{k}$ (i.e. the angle of the detector) passes through the Fermi surface. The intensity disappears above the Fermi surface, because the Fermi surface is *defined* as the location above which there are no more filled electron states. And if there are no filled electron states, then no electrons can be ejected. So by mapping the locations in $\vec{k}$-space at which the intensity peaks disappear, ARPES can map the location of the Fermi surface. ARPES also maps the dispersion E vs. k for the electrons below the Fermi surface.

Below T_c

Below T_c in a d-wave superconductor, things get more interesting because an anisotropic gap opens up in the density of states at the Fermi level. ARPES can measure the energy of the gap as a function of position in $\vec{k}$-space by using gold (in contact with the BSCCO) as a reference for the real Fermi level, and noting the shift in the energy where the BSCCO peak disappears vs. the gold peak. What they find is that below T_c, the gap is zero only at 4 points, along the a and b crystal axes (the "nodal" points), and largest along the x and y axes (the "anti-nodal" direction). The angle dependence of the gap has been mapped out by Ding, *et al.*[57] and other groups.[58, 59, 60, 61, 62, 63]

In summary, we have from STM the energy landscape of BSCCO in $\vec{R}$-space, and from

ARPES the energy landscape of BSCCO in $\vec{k}$-space.

2.3.2 Neutron Scattering

Neutron scattering is the best way to obtain $\vec{k}$-space information about the magnetic properties of a material. A good introduction to the experimental techniques of neutron scattering can be found in a conference presentation by Boothroyd.[64]

Neutron scattering is a bulk probe with no spatial resolution (but with the benefit that it is definitely not sensitive to surface effects or to the specifics of cleaving procedure). Neutrons are so weakly interacting that a sample of size ~ 1 cm^3 is required for adequate signal strength. Therefore most neutron scattering experiments are performed on LSCO, the best material for growth of large crystals.

Neutrons can probe two different aspects of a crystal: the locations of the atomic nuclei, or the magnetic structure of the electrons. Elastic neutron interactions with the nuclei give us Bragg diffraction peaks, which enable determination of the crystal structure. Inelastic neutron interactions with the nuclei give the phonon dispersion relations of the crystal.

For comparison with STM searches for alternative phases in HTSCs, the neutron interactions with the electron spins are more relevant. These elastic and inelastic interactions measure the static and dynamic electron spin ordering in the crystal, respectively. Specifically, neutron scattering off electron spins measures the magnetic susceptibility as a function of $\vec{k}$-space.

The neutron scattering setup is similar to ARPES: columnated, monochromatic neutrons are incident on the cuprate crystal parallel to the CuO_2 plane. The energy-resolved neutron detector is then moved through a range of solid angles above the crystal, and the number of incident neutrons are counted for each solid angle interval $d\Omega$ and (in the case of inelastic neutron scattering) each energy interval dE.

Inelastic Neutron Scattering

An inelastic neutron scattering event involves both a momentum transfer and an energy transfer:

$$\hbar\mathbf{Q} = \hbar(k_i - k_f) \tag{2.18}$$

$$\hbar\omega = E_i - E_f = \hbar^2(k_i^2 - k_f^2)/2m \tag{2.19}$$

The scattering event is therefore characterized by $(\mathbf{Q}, \omega)$. The scattering probability is represented by the differential cross-section:

$$\frac{d^2\sigma}{d\Omega dE_f} = \frac{k_f}{k_i} S(\mathbf{Q}, \omega) \tag{2.20}$$

The k_f/k_i factor is sometimes important, for example if the neutron loses a lot of energy ($k_f \ll k_i$) then the intensity is much reduced. But $S(\mathbf{Q}, \omega)$ contains all the physics of the system, and is given by the fluctuation-dissipation theorem:

$$S(\mathbf{Q}, \omega) \propto \underbrace{\frac{1}{1 - e^{-\hbar\omega/k_B T}}}_{\text{Bose factor}} \underbrace{\text{Im}\{\chi(\mathbf{Q}, \omega)\}}_{\chi''(\mathbf{Q}, \omega)} \tag{2.21}$$

where $\chi(\mathbf{Q}, \omega)$ is magnetic susceptibility, i.e.:

$$M(\mathbf{Q}, \omega) = \chi(\mathbf{Q}, \omega) H(\mathbf{Q}, \omega) \tag{2.22}$$

Inelastic neutron scattering has been used to look for dynamic spin fluctuations in LSCO[65] and YBCO[66] and recently even BSCCO[67] (albeit with much larger linewidths than LSCO or YBCO).

Elastic Neutron Scattering

Elastic neutron scattering is really just a special case of inelastic neutron scattering, with $\omega = 0$. Therefore, elastic neutron scattering measures the static spin ordering. The technique is analogous to mapping the positions of nuclei in crystals using X-ray or neutron diffraction, except it is the static spins of the electrons which are being mapped.

Studies of static spin ordering have been carried out in LSCO[46] and LCO.[68]

2.3.3 Nuclear Magnetic Resonance

Nuclear magnetic resonance (NMR) can explore the spatial distribution of magnetic field within a sample. Reviews of NMR on high-T_c superconductors have been written by Rigamonti *et al.*[69] and Berthier *et al.*[70]

For a material such as BSCCO with a complicated unit cell, NMR can individually access the magnetic environment at each atomic species, because each species will have a

different Larmor precession frequency. The linewidth around the central frequency for each species will give information about the degree of disorder and local field distribution in the sample. In fact, large NMR linewidths in BSCCO were some of the first evidence for gross electronic inhomogeneity.

NMR also measures the inverse spin-lattice relaxation time $1/T_1$, which is a measure of spin fluctuations. NMR studies showing additional spin susceptibility at low temperature in BSCCO indicated strong electronic disorder.[71] Since YBCO is a more ordered crystal than BSCCO (the oxygen dopants fit into known crystal lattice sites in the chain plain, instead of squishing in interstitially like BSCCO), the narrower linewidths in YBCO make it easier to extract quantitative NMR information. Therefore, most NMR studies on the cuprates have been carried out on YBCO.

NMR is very useful for studies of vortices in superconductors. The Larmor frequency of the probe nucleus is a measure of the local field. Therefore, the full Larmor lineshape can be seen as a sort of "histogram" of atomic locations relative to the vortex center.[72] This can be used to determine the spatial symmetry of the vortex lattice (triangular, square, etc.), or the properties of quasiparticles existing in different local fields.

2.4 Summary

In summary, this thesis documents the use of a scanning tunneling microscope (STM) to study the real-space dependence of the density-of-states in $Bi_2Sr_2CaCu_2O_{8+\delta}$ (BSCCO), with sub-Å resolution. Angle-resolved photoemission spectroscopy (ARPES) is a complementary technique which accesses the $\vec{k}$-space dependence of the density-of-states in BSCCO. Both STM and ARPES are surface sensitive techniques which require clean, flat surfaces for effective study. Of the 3 families of hole-doped high-T_c superconductors, BSCCO is easiest to cleave and produce such a clean, flat surface.

Neutron scattering and nuclear magnetic resonance (NMR) are two more techniques which access the magnetic information in a crystal. Both are bulk probes, insensitive to surface effects. Neutron scattering measures the dynamic and static spin ordering in the crystal in $\vec{k}$-space, and is typically limited in application to large single crystals ($\sim$ 1 cm) such as the lanthanum family of cuprates. NMR measures the distribution of magnetic fields in a sample, and is a useful tool for studying vortices. NMR is typically most effective on well-ordered crystals such as $YBa_2Cu_3O_{7-\delta}$ (YBCO).

Chapter 3

Quasiparticle Interference

This chapter details the use of Fourier-transform scanning tunneling spectroscopy (FT-STS) to yield simultaneous real space and momentum space information in the high temperature superconductor $Bi_2Sr_2CaCu_2O_{8+\delta}$ (BSCCO). Because quasiparticles in BSCCO are both inhomogeneous and highly correlated, a full understanding of their properties will require knowledge of both their $\vec{R}$-space and $\vec{k}$-space behavior. This work represents the first application of FT-STS to a cuprate superconductor. The trick of this analysis technique is to take advantage of scattering, which leads to interference patterns in the quasiparticle density of states that can be imaged with scanning tunneling microscopy and spectroscopy. By Fourier-transforming then inverting the real-space interference patterns, we can access the $\vec{k}$-space information in the sample.

In this work, FT-STS is applied to optimally doped BSCCO samples at $T = 4.2$ K, with $B = 0$ Tesla. The BSCCO phase space explored in this chapter is shown in figure 3.1.

3.1 Basic Scattering Explanation

In an ideal metal, the Landau quasiparticle eigenstates are Bloch wavefunctions characterized by wavevector $\vec{k}$ and energy ε. As discussed in chapter 2, their dispersion relation, $\varepsilon(\vec{k})$, can be measured with momentum resolved techniques such as angle resolved photoemission spectroscopy (ARPES). By contrast, real space imaging techniques, such as scanning tunneling microscopy (STM), cannot be used to measure $\varepsilon(\vec{k})$. This is because the local density of states LDOS(E) spectrum at a single location $\vec{r}$ is related to the $\vec{k}$-space eigenstates $\Psi_k(\vec{r})$ by

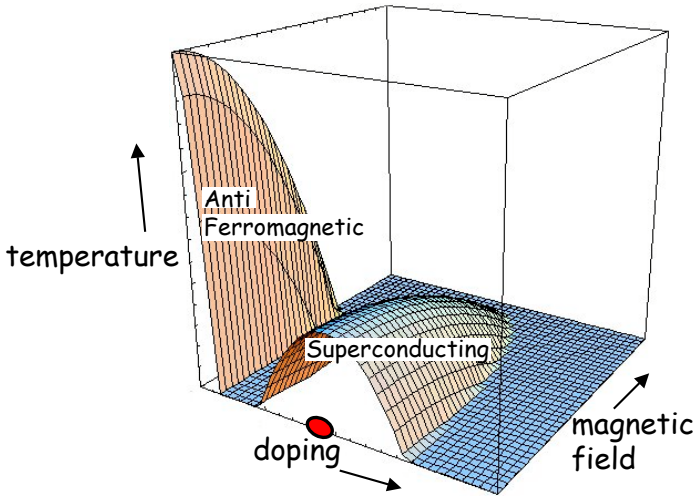

Figure 3.1: A schematic phase diagram of $Bi_2Sr_2CaCu_2O_{8+\delta}$. The red circle shows the area in phase space covered in this chapter. Optimally doped samples are studied at $T = 4.2$ K, with $B = 0$ Tesla.

$$\mathrm{LDOS}(E, \vec{r}) \propto \sum_k |\Psi_k(\vec{r})|^2 \delta(E - \varepsilon(\vec{k})) \tag{3.1}$$

Substitution of a Bloch wavefunction into Eqn. 3.1 shows LDOS(E) to be spatially uniform.

Sources of disorder such as impurities or crystal defects cause elastic scattering which mixes eigenstates of different $\vec{k}$ but the same $\varepsilon(\vec{k})$. In other words, elastic scattering mixes states that are located on the same quasiparticle contour of constant energy (CCE) in $\vec{k}$-space. When scattering mixes states $\vec{k_1}$ and $\vec{k_2}$, the result is a standing wave in the quasiparticle wavefunction Ψ_k of wavevector $\vec{q}_{\mathrm{wfn}} = (\vec{k_1} - \vec{k_2})/2$. Since LDOS is proportional to the norm of the quasiparticle wavefunction $|\Psi_k|^2$, the LDOS will contain an interference pattern with wavevector $\vec{q} = \vec{k_1} - \vec{k_2}$, or wavelength $\lambda = 2\pi/q$. LDOS modulations can be observed by STM as spatial modulations of the differential tunneling conductance dI/dV.

The Bogoliubov quasiparticles in a BCS superconductor are also Bloch states, but with dispersion

$$E_{\pm}(\vec{k}) = \pm\sqrt{\varepsilon(\vec{k})^2 + \Delta(\vec{k})^2} \tag{3.2}$$

where $|\Delta(\vec{k})|$ is the $\vec{k}$-dependent magnitude of the energy gap at the Fermi surface (CCE for $\varepsilon(\vec{k}) = 0$ in the normal state). Elastic scattering of Bogoliubov quasiparticles can also result in conductance modulations. The trick we employ is to measure the wavelengths of

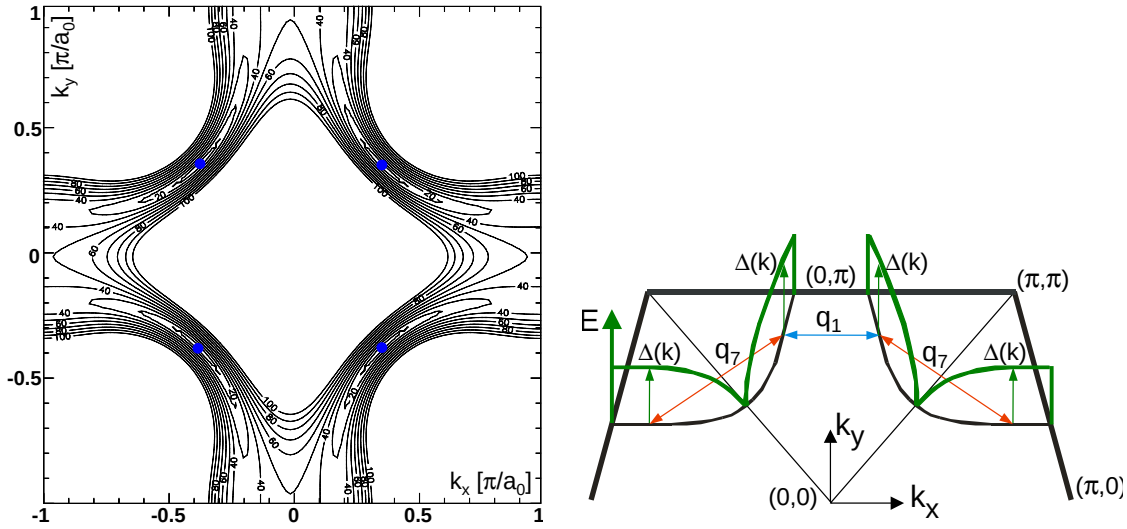

(a) contour map (b) perspective view

Figure 3.2: Brillouin zone schematic. (a) Contour map of the energy landscape in the first Brillouin zone of BSCCO in the superconducting state. At the four gap nodes (shown in blue), quasiparticle states exist down to zero energy while, at other $\vec{k}_{FS}$, a quasiparticle energy $E = |\Delta(\vec{k}_{FS})|$ is required to create the first excitation. (b) A perspective view of half the first Brillouin zone. The superconducting energy gap $|\Delta(\vec{k}_{FS})|$ (green) is shown as a function of the location $\vec{k}_{FS}$ along the normal state Fermi surface (black). Vectors connecting areas of the normal state Fermi surface with identical $|\Delta|$ are shown and labeled by blue and red arrows depending on the type of elastic scattering process at $E = |\Delta|$ that connects them.

the conductance modulations as a function of energy, and use the $\vec{k}$-space symmetries of the band structure (as determined by ARPES) to work backwards to a quantitative map of certain CCE in $\vec{k}$-space.

At low temperatures in BSCCO, a $\vec{k}$-dependent energy gap $\Delta(\vec{k})$ opens on the Fermi surface and new quasiparticles appear. As discussed in chapter 2, both the Fermi surface location in momentum-space, $\vec{k}_{\rm FS}$, and its energy gap at these locations, $|\Delta(\vec{k}_{\rm FS})|$, have been comprehensively studied by ARPES. In Fig. 3.2, we reproduce the superconducting energy landscape in $\vec{k}$-space as a contour map, and also as a perspective map with energy along the z-axis. The latter view perhaps makes it more clear that the energy gap rises from 0 meV at the four nodal points up to a maximum at the edges of the Brillouin zone.

3.1.1 Octet Model

A glance at figure 3.2(a) shows that the CCE are complicated. If there is elastic scattering from every point on a given CCE to every other point, there will be density of states modulations of all wavevectors; these will be impossible to untangle. But it turns out that the elastic scattering is dominated by just a few wavevectors.

In a simple metal, the amplitude of scattering obeys Fermi's golden rule:

$$w(i \to f) \propto \frac{2\pi}{\hbar}|V(\vec{q})|^2 n_i(E_i, \vec{k}_i) n_f(E_f, \vec{k}_f) \tag{3.3}$$

where $E_i = E_f$ for elastic scattering, $\vec{q} = \vec{k}_f - \vec{k}_i$, and $V(\vec{q})$ is the Fourier component of the scattering potential at wavevector $\vec{q}$. For simplicity, we will start with the assumption that $V(\vec{q})$ is relatively flat in $\vec{q}$.

In a superconductor there is an additional complication from coherence factors:[73]

$$w(i \to f) \propto \frac{2\pi}{\hbar}(u_{k_i} u_{k_f} \pm v_{k_i} v_{k_f})|V(\vec{q})|^2 n_i(E_i, \vec{k}_i) n_f(E_f, \vec{k}_f) \tag{3.4}$$

where the minus sign is for non-magnetic scatterers, the plus sign is for magnetic scatterers, and u_k and v_k for a d-wave superconductor are given by:

$$v_k^2 = \frac{1}{2}\left[1 - \frac{\varepsilon_{\mathbf{k}}}{\sqrt{\Delta_k^2 + \varepsilon_k^2}}\right]; \qquad u_k^2 = 1 - v_k^2 \tag{3.5}$$

It is apparent from equations 3.3 and 3.4 that a particular wavevector $\vec{q}$ can dominate the quasiparticle interference at energy E, if the $\vec{k}$-pairs on the CCE connected by $\vec{q}$ have a large joint density of states (joint-DOS). So we need to ask, for a given energy E, which locations in the Brillouin zone have the largest DOS for that energy? The density of states is given by:

$$\mathrm{DOS}(E) = n(E) \propto \frac{1}{|\bigtriangledown_k(E)|} \tag{3.6}$$

Therefore, the largest DOS will occur where the gradient $|\bigtriangledown_k(E)|$ is smallest, i.e. where the contours are farthest apart. Because the Brillouin zone has 4 axes of reflection, there will be 8 equivalent locations of highest DOS for a given non-zero energy E. These locations will be at the end of the "banana"-shaped contours, as shown in figure 3.3. The highest joint-DOS

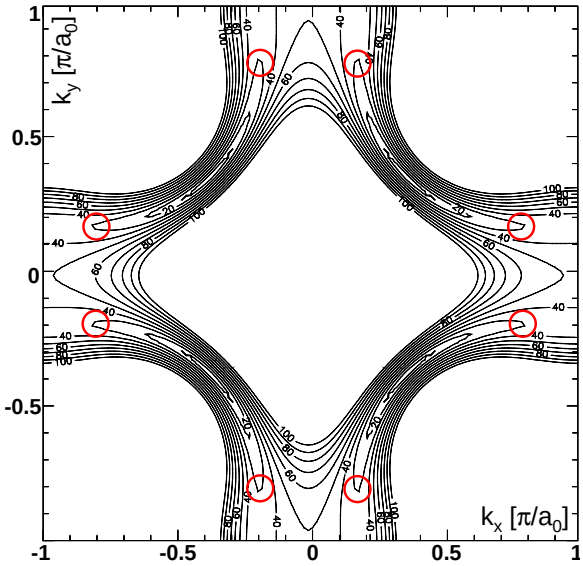

Figure 3.3: Contours of constant energy up to 100 meV in the first Brillouin zone of BSCCO in the superconducting state. At a given energy, say $E = 30$ meV, the largest contribution to the DOS will come from the eight points where the slope in this "energy landscape" is shallowest, i.e. from within the eight red circles at the ends of the four 30 meV "banana"-shaped contours.

for quasiparticle scattering at this energy occurs at the $\vec{q}$-vectors connecting these eight points. We therefore expect the interference-induced conductance modulations to dominate at these connecting $\vec{q}$-vectors.

For a given octet at a given energy, there will be 8×7=56 $\vec{q}$-vectors connecting the 8 points, but symmetry reduces the set of unique $\vec{q}$-vectors to 32. However, since the $\vec{q}$-vector manifests itself in our STM images as a modulation at a given wavelength, we cannot distinguish between $+\vec{q}$ and $-\vec{q}$. This further reduces the number of independent $\vec{q}$-vectors we can measure to 16. In fact, because of the 8-fold symmetry of the Brillouin zone, there are theoretically only 6 truly independent vectors, but we can measure some of them several times, rotated by 90°, or flipped across an axis of symmetry, and thus we can make 16 independent measurements. The symmetry of these scattering $\vec{q}$-vectors is demonstrated in figure 3.4.

3.1.2 Dispersion

Figure 3.3 shows the relevant octet of points for energy $E = 30$ meV, and figure 3.4 shows the expected scattering wavevectors for that energy. But this octet will move as a

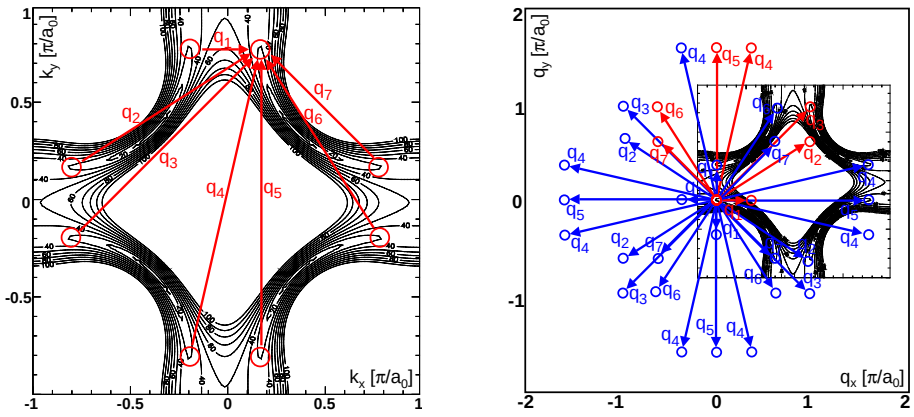

(a) (b)

Figure 3.4: Expected scattering wavevectors from octet model. (a) The octet of $\vec{k}$-states with highest DOS, and seven labeled $\vec{q}$-vectors connecting one point to all its partners. (b) The symmetrized set of $\vec{q}$-vectors we would expect to see in a $\vec{q}$-space area twice the size of the Brillouin zone. Note that the scale is not the same in (a) and (b): (a) is just the first Brillouin zone, while (b) is two Brillouin zones across.

function of energy; the bananas get longer with increasing energy. For example, we expect $\vec{q_1}$ to decrease with increasing energy, while we expect $\vec{q_7}$ to increase with increasing energy. A schematic of the dispersion is shown in figure 3.5.

3.1.3 Joint-DOS Calculation

The previous two sections presents the simplest of all possible models: for a given energy we deal with only eight points in $\vec{k}$-space. We can make a slightly more complicated (but equally naïve) check by actually calculating the joint-DOS for the whole Brillouin zone, thereby taking into account points that aren't at the ends of the bananas. We can also include the coherence factors, which will tell us which points in $\vec{q}$-space may be due to potential or magnetic scattering.

We start with Norman's tight-binding parameterization of the normal state band structure of BSCCO for $p = 0.17$ hole doping.[74]

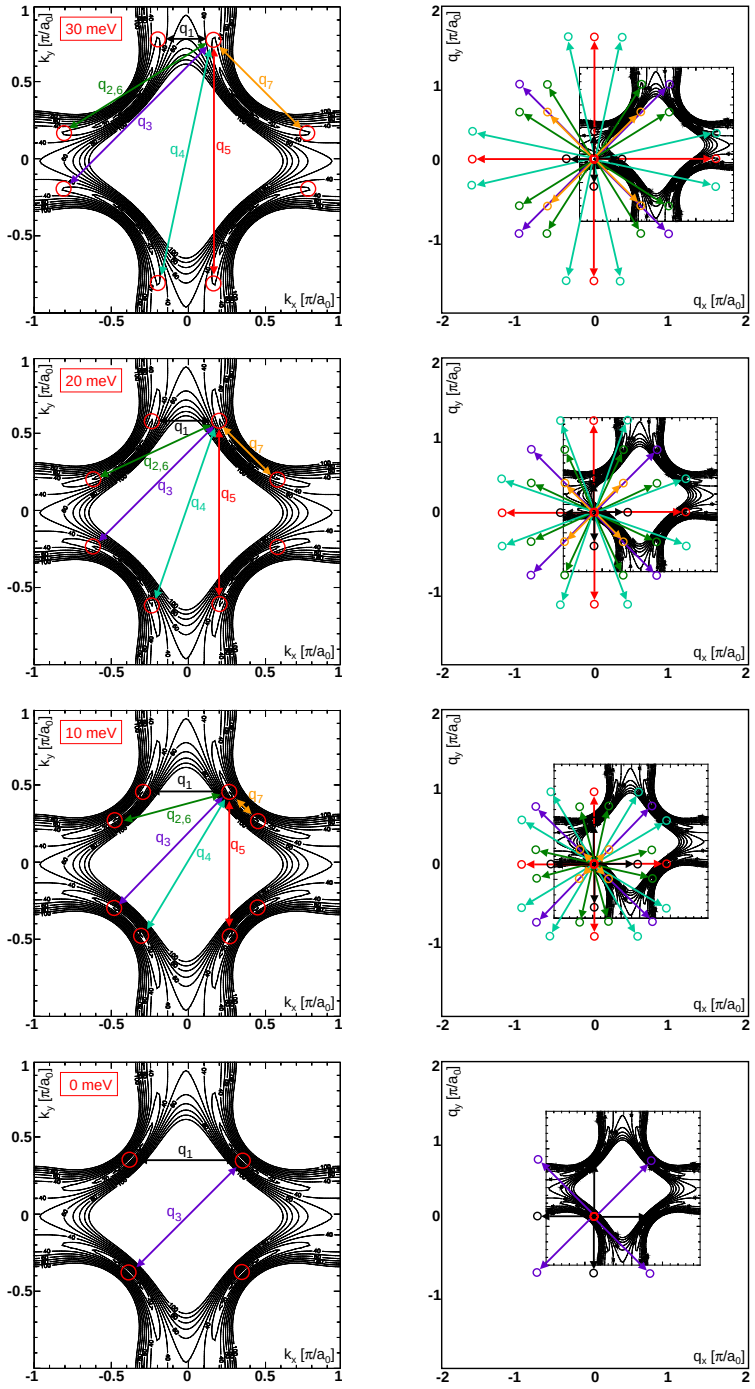

Figure 3.5: Column (a): The octet of $\vec{k}$-states with highest DOS, at 4 different energies, with a representative set of $\vec{q}$-vectors connecting them. Column (b): The full symmetrized set of 32 $\vec{q}$-states we would expect to see at the corresponding energies. Note the scale difference between column (a) and column (b).

$$\begin{aligned}\varepsilon(\vec{k}) &= t_0 \\ &\quad + t_1 * [\cos(k_x) + \cos(k_y)]/2 \\ &\quad + t_2 * \cos(k_x)\cos(k_y) \\ &\quad + t_3 * [\cos(2k_x) + \cos(2k_y)]/2 \\ &\quad + t_4 * [\cos(2k_x)\cos(k_y) + \cos(k_x)\cos(2k_y)]/2 \\ &\quad + t_5 * \cos(2k_x)\cos(2k_y) \end{aligned} \tag{3.7}$$

where the t_i are given in table 3.1. (Note that this does not include bilayer splitting, because at the time of publication (1995) bilayer splitting had not been observed in BSCCO.)

Norman has given several different BSCCO parameterizations[a] in different papers:

1. Tight-binding fit by Radtke *et al.*[75] to normal state ARPES data from Dessau *et al.*[58] measured in 1993.

2. Tight binding fit by Norman *et al.*[74] to new normal state ARPES data measured in 1995 by Ding *et al.*[80] on an instrument with higher energy resolution. However, it should be noted that this data still did not show any bilayer splitting (which has since been observed,[81] but only in overdoped $Bi_2Sr_2CaCu_2O_{8+\delta}$) and also the superconducting part of this data showed two nodes in the gap, at 35° and 55°, rather than the single node at 45° which we now know to exist, due to the $d_{x^2-y^2}$ pairing. Because this was a fit to normal state data, it probably doesn't matter that the gap data was wrong. This parameterization agrees well with data in another paper by Ding *et al.*,[82] which also shows no bilayer splitting.

3. Some modifications were made to these parameters by Norman *et al.*:[83] the energy contours near the anti-nodal points were flattened, and the nodal points were moved away from (0,0) to compensate. These changes were made to investigate the effects of nesting, but they do not necessarily agree with experimental data.

4. Norman has a later paper giving an alternative set of t_i's,[84] which is discussed further by Escrig *et al.*[85] These alternative parameters are less appropriate because they

[a] Analogous parameters for YBCO have been given in several papers:

1. Norman parameterization by Radtke *et al.*[75] based on Campuzano data from 1993.[76, 77]
2. More recent experimental results from ARPES.[78]
3. Calculated results from a slave-boson approach, which include only the terms t_0, t_1, and t_2.[79]

Parameters for LSCO have also been given by Radtke *et al.*[75]

represent a "bare" dispersion without any interactions; the real material would of course be renormalized by interactions. These changes were made so that these theorists could investigate what kind of interactions might restore the parameters to their experimental values.

The most relevant set of t_i's is therefore from the second paper[74] and is reproduced in the second column of table 3.1. However, Norman cautions that the normal state peaks as detected by ARPES are quite broad, so "the accuracy of the dispersion may not be completely adequate." Furthermore, "the dispersion is definitely renormalized in the superconducting state relative to the normal state."[b]

Note that the column 2 parameterization we are using was a fit to a sample with $p = 17\%$ doping. This is close to optimally doped. It corresponds to an average gap of 36 meV, so we will use $\Delta_0 = 36$ meV when we impose a gap on the normal state parameterization.

We can check the doping of the parameterization simply by adding up the area of the hole pocket. The undoped Mott insulator has an exactly half-filled band, so the hole pocket area would be 50% of the total first Brillouin zone area. For a doped crystal band structure, the fractional area of the hole pocket will be $f > 0.5$. Then the doping can be defined as $p \equiv 2 \times (f - 0.5)$. I have verified that the column 2 parameterization does indeed correspond to $p = 17\%$ doping. To a reasonable approximation, the parameterization can be adjusted to reflect a different doping level simply by adjusting the parameter t_0 to expand or contract the hole pocket to the correct area.[c]

t_i	function	Radtke 1994	Norman 1995	Norman 2000	Eschrig 2000
t_0	1	0.0607	0.1305	0.0879	0.0989
t_1	$\frac{1}{2}[\cos(k_x) + \cos(k_y)]$	-0.525	-0.5951	-0.5547	-0.5908
t_2	$\cos(k_x)\cos(k_y)$	0.1	0.1636	0.1327	0.0962
t_3	$\frac{1}{2}[\cos(2k_x) + \cos(2k_y)]$	0.0287	-0.0519	0.0132	-0.1306
t_4	$\frac{1}{2}[\cos(2k_x)\cos(k_y) + \cos(k_x)\cos(2k_y)]$	-0.175	-0.1117	-0.1849	-0.0507
t_5	$\cos(2k_x)\cos(2k_y)$	0.0107	0.0510	0.0265	0.0939

Table 3.1: Several different parameterizations of the $Bi_2Sr_2CaCu_2O_{8+\delta}$ normal state band structure. I will use the second column in all further calculations, which is for a hole doping close to optimally doped of $p = 17\%$, which corresponds to an average gap of $\Delta_0 \sim 36$ meV.

[b] Norman: private communication, 2002
[c] Norman: private communication, 2002

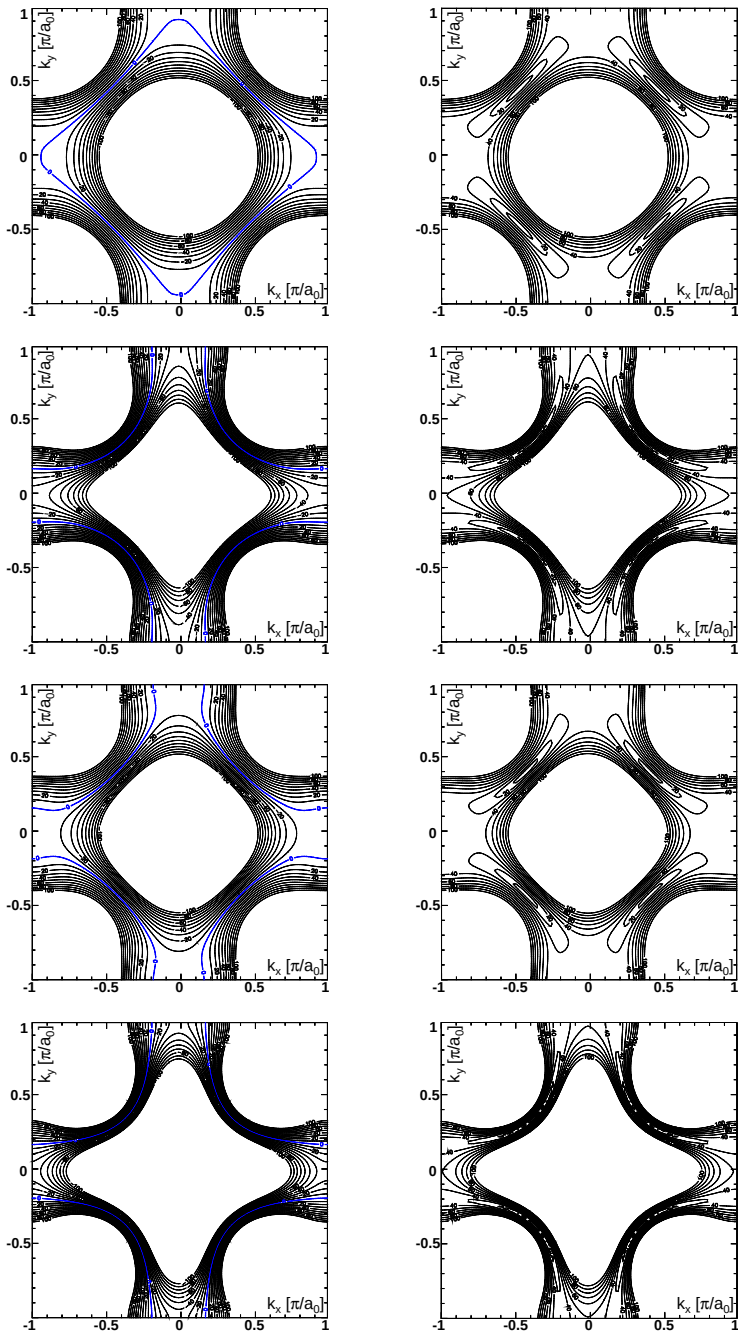

(a) normal (b) superconducting

Figure 3.6: Comparison of band structure parameterizations. Column (a) is the normal state and column (b) is the superconducting state. Rows 1–4 in this figure represent columns 3–6 in table 3.1, respectively.

To find the superconducting state band structure, we need a formula for the superconducting gap as a function of angle, Δ_k. Several possibilities exist in the literature. Theorists[86] tend to use:

$$\Delta_k = \Delta_0[\cos(k_y) - \cos(k_x)]/2 \tag{3.8}$$

The ARPES community parameterizes the gap as a function of angle from the (π, π) point (the Y point) in the first Brillouin zone. The lowest order terms consistent with $d_{x^2-y^2}$ symmetry are $\cos(2\theta)$ and $\cos(6\theta)$. Therefore, Δ_k can be written as:

$$\Delta_k = \Delta_0[B\cos(2\theta) + (1-B)\cos(6\theta)] \tag{3.9}$$

where B is a parameter which depends on doping, according to table 3.2.[63] The comparison between the two methods of gap calculation (and several values of B) is shown in figure 3.7.

doping	T_c	B value
OD	80 K	1.0
OD	87 K	0.96
UD	83 K	0.92
UD	75 K	0.89
UD	75 K	0.885 (2^{nd} sample)
UD	80 K	0.88

Table 3.2: Mesot parameterization of $Bi_2Sr_2CaCu_2O_{8+\delta}$ superconducting gap Δ_k.[63]

We can perform another check on the validity of Norman's parameterization by comparing directly to our own data. After imposing the superconducting gap, we can integrate the density of states from Norman's entire first Brillouin zone. We should arrive at a spectrum very similar to that observed via STM with a 36 meV gap. The actual comparison is shown in figure 3.8.

We can also include the coherence factors u_k and v_k. Again, there are several different sign and phase conventions for parameterizing these. I use the sign convention according to equation 3.35 in Tinkham:[73]

$$v_k^2 = \frac{1}{2}\left[1 - \frac{\varepsilon_{\mathbf{k}}}{\sqrt{\Delta_k^2 + \varepsilon_k^2}}\right]; \qquad u_k^2 = 1 - v_k^2 \tag{3.10}$$

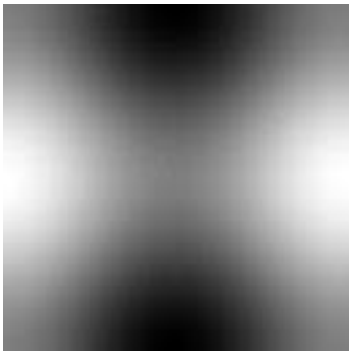

(a) $\Delta_0[\cos(k_y) - \cos(k_x)]/2$

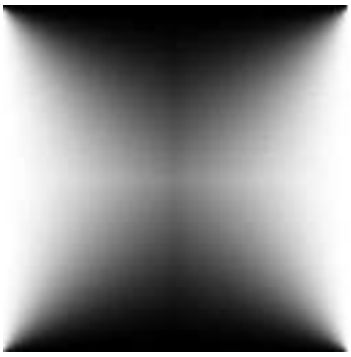

(b) $B = 1$

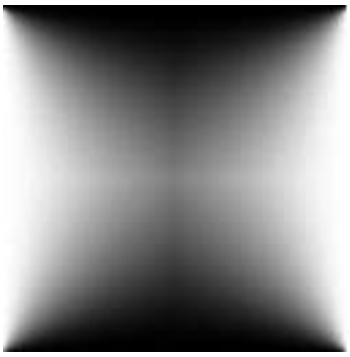

(c) $B = 0.96$

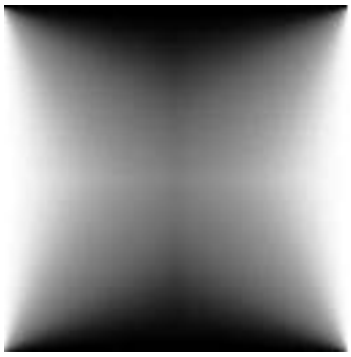

(d) $B = 0.88$

Figure 3.7: Comparison of several possible parameterizations of a d-wave superconducting gap. (a) Theorist version of a d-wave gap, calculated using eqn 3.8. Experimentalist version of a d-wave gap, with (b) $B = 1$, (c) $B = 0.96$, and (d) $B = 0.88$. From this point forward, for our calculations, we will use the gap shown in 3.7(a).

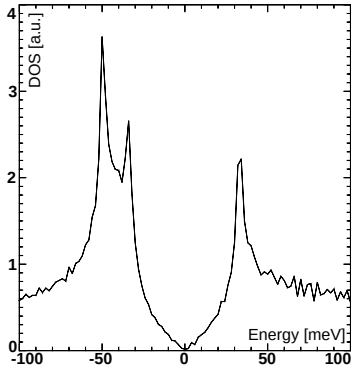

(a) calculation

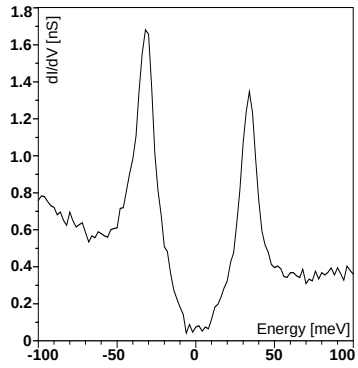

(b) raw data

Figure 3.8: Density of states comparison: (a) calculation by numerical integration over Norman's tight-binding band structure parameterization vs. (b) typical STM spectrum on the surface of BSCCO (raw data).

These parameterizations of u_k and v_k are shown in figure 3.9.

(a) u_k (b) v_k

Figure 3.9: (a) u_k and (b) v_k for a $d_{x^2-y^2}$-wave superconductor, according to Tinkham[73] and equation 3.8.

Finally, having decided all our conventions, we may begin the calculation. The joint-DOS was calculated on a 512×512 pixel array, using the normal state band structure parameterization given in column 2 of table 3.1, with gap given by equation 3.8 and $\Delta_0 = 36$ meV. The basic plan is for each energy, to make a 3-dimensional "histogram" of all allowed scattering $\vec{q}$'s. In other words, for each pair of states at $\vec{k_1}$ and $\vec{k_2}$ which can elastically scatter, we will add one to the 3-dimensional histogram at energy $\varepsilon(\vec{k_1}) = \varepsilon(\vec{k_2})$ and location $\vec{q} = \vec{k_1} - \vec{k_2}$.

The experiment was performed at temperature $T = 4.2$ K which gives an energy broadening of $\sim 4k_BT = 1.44$ meV. (One factor of 2, because the Fermi function step function is smeared by approximately k_BT on either side of ε_F, and the other factor of 2 because we have thermal broadening in both the initial and final states.) So in the calculation, I allow $\vec{k}$-states to "elastically" scatter to other $\vec{k}$-states whose energy would differ by up to 1.44 meV in the zero temperature band structure. For example, if $\varepsilon(\vec{k_1}) = 10$ meV and $\varepsilon(\vec{k_2}) = 11.44$ meV, I include $\vec{q} = \vec{k_2} - \vec{k_1}$ in the count of the scattering wavevectors.

The experiment was performed with a bias voltage modulation of 2 mV RMS, or 5.6 mV peak-to-peak. But energy maps were taken with a 2 meV spacing. So for each pair of states $\vec{k_1}$ and $\vec{k_2}$ which can "elastically" scatter (subject to finite temperature broadening), I add one to the histogram in each energy layer within 2.8 meV of $\varepsilon(\vec{k_1})$ or $\varepsilon(\vec{k_2})$. In other words, some scattering $\vec{q}$'s are double-counted in several energy layers, which simulates the real experimental conditions.

For the simplest joint-DOS calculation, I ignore the coherence factors u_k and v_k, and simply add one to the histogram at the appropriate energy and $\vec{q}$ for each allowed pair $\vec{k_1}$

and $\vec{k_2}$. These results are shown in column (a) of figure 3.10. These results confirm visually that the joint-DOS is actually dominated by the banana octet.

The algorithm used was:

```
compute the normal state energy contour map in a 256 x 256 pixel array
impose the superconducting gap
compute the 256 x 256 pixel u_k and v_k arrays
allocate 3 different 512 x 512 pixel x nEnergies arrays
  to hold the results of the plain joint-DOS,
  potential scattering, and magnetic scattering

for each point k1 in the Brillouin zone {
  for each point k2 in the Brillouin zone {
    if ( |e(k1)-e(k2)| < 4 k_B T ) then {
      q = k1 - k2
      for each energy E {
        if |E - ( e(k1)+e(k2) )/2| < 4 k_B T + e dV {
          add 1 to jdos(E)
          add u_k1 * u_k2 + v_k1 * v_k2 to mag(E)
          add u_k1 * u_k2 - v_k1 * v_k2 to pot(E)
} } } } }
```

Note that realistic parameter choices are essential to arriving at this result. First, if we don't use a high enough resolution $x \times y$ grid, we arrive at confusing results. The real material, of course, has a grid of infinite resolution. [Note that our STM measurements sample at finite resolution, but the interference patterns themselves do have infinite resolution.] So our 512×512 pixel grid comes closest to approximating the real situation. Results from smaller grids are shown in figure 3.11. Secondly, if we don't use realistic energy broadening parameters, we arrive at confusing results. The real material is sitting at $T = 4.2$ K, so there really will be some "elastic" scattering between $\vec{k}$ locations whose energies differ slightly. And the real experiment does include $\vec{q}$ states from a finite energy range in each map, even overlapping with the map at nearest energy. Results from unrealistically small energy broadening parameters are shown in figure 3.12.

One interesting aspect of this calculation is that the most naïve joint DOS calculation shows 16 distinct peaks in $\vec{q}$-space, while magnetic and scalar scattering each show a complementary set of 8 $\vec{q}$-peaks. In the real experiment, we see all 16 peaks, which suggests that we have multiple types of scattering present in the crystal.

However, we caution that even this calculation is exceedingly naïve. We are effectively taking into account only the imaginary part of the Green's function. A full scattering model

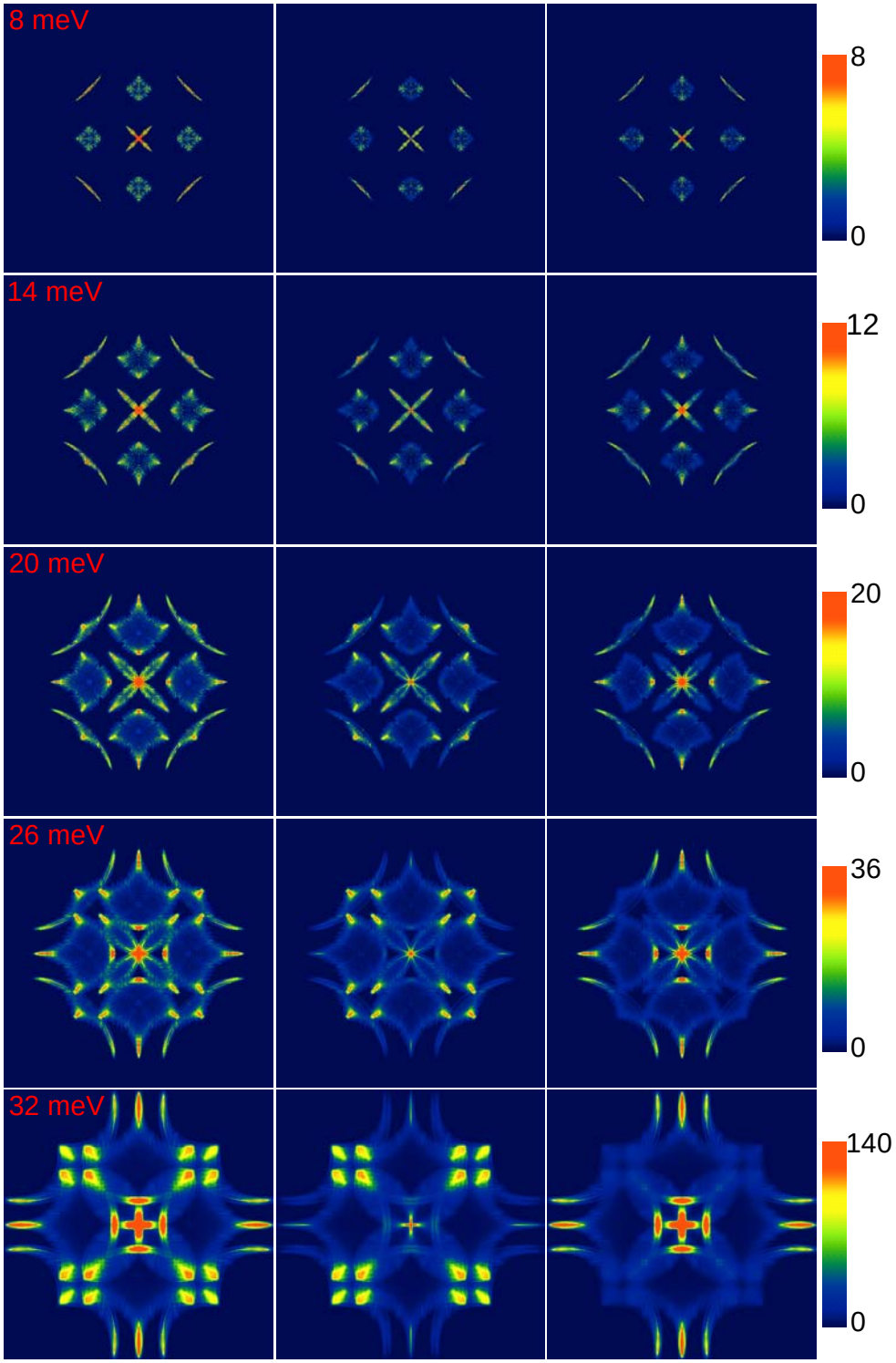

Figure 3.10: The results of a joint-DOS calculation on the full Brillouin zone, with (a) no coherence factor; (b) coherence factor $(u_{k_i}u_{k_f} - v_{k_i}v_{k_f})$ for potential scatterers; and (c) coherence factor $(u_{k_i}u_{k_f} + v_{k_i}v_{k_f})$ for magnetic scatterers. Scalebars show arbitrary units, which are however consistent from one energy to the next.

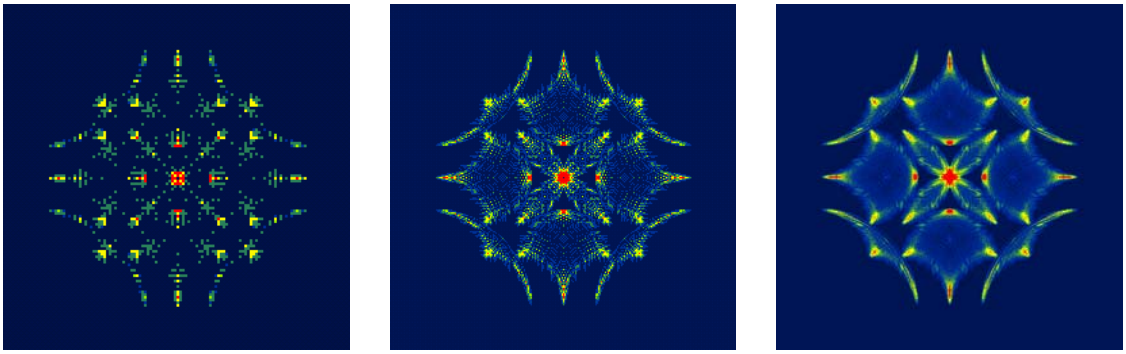

(a) 128 × 128 pixels (b) 256 × 256 pixels (c) 512 × 512 pixels

Figure 3.11: Comparison between joint-DOS calculations with different pixel resolution, at $E = 24$ meV. If the calculation is performed with insufficient pixel resolution, as in (a), the dominant scattering vectors do not stand out as strongly against the background, as they do when the calculation is performed at higher spatial resolution, as in (c).

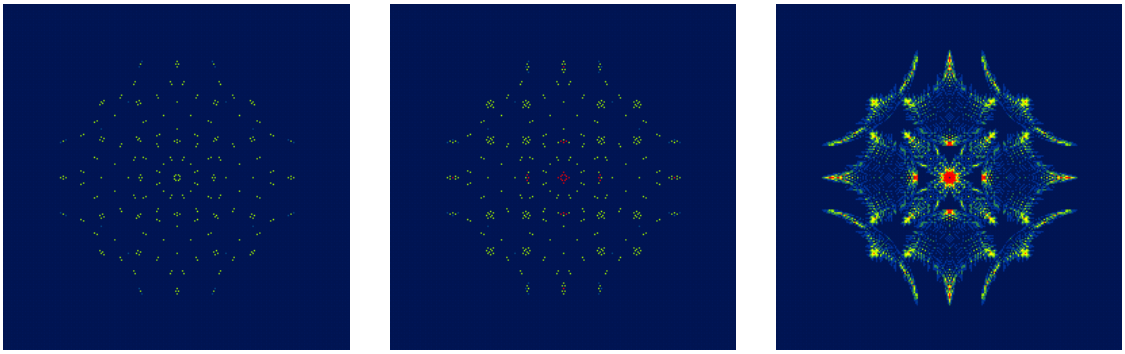

(a) $k_BT = 0.36$ meV; energy resolution 1 meV (b) $2k_BT = 0.72$ meV; energy resolution 2 meV (c) $4k_BT = 1.44$ meV; energy resolution 5.6 meV

Figure 3.12: Comparison of joint-DOS calculations at $E = 24$ meV with different energy broadening. Both thermal broadening and experimental energy resolution increase from (a) to (c). Results in (a) and (b) may be misleading, whereas the broadening parameters and resulting joint-DOS in (c) most closely approximate the real crystal.

would include also the real part of the Green's function, which leads to the appearance of other points in $\vec{q}$-space.[86]

3.2 Data

I will show here the results of high-resolution LDOS imaging at 4.2 K on BSCCO crystals grown by the floating zone method with superconducting transition temperature ranging between underdoped (T_c = 78 K) and slightly overdoped (T_c = 85 K). The samples are cleaved at the BiO plane in cryogenic ultra high vacuum and immediately inserted into the STM head. Atomic resolution is achieved throughout the studies reported here. On these surfaces, we acquire maps of the differential tunneling conductance ($g = dI/dV$) measured at all locations (x, y) in the field of view. Because LDOS($E = eV$) $\propto g(V)$, where V is the sample bias voltage, this results in a two dimensional map of the LDOS at each energy E.

Figure 3.13 shows a topographic image and three LDOS maps for quasiparticle energies centered at 12, 16, and 22 meV, all acquired in the same 650 Å field of view with 1.3 Å spatial resolution. Periodic LDOS modulations are evident in all images (although one also sees remnants of impurity scattering at low energies and of gap disorder at high energies). Notably, quite different spatial patterns and wavelengths are observed at each energy.

At low energies, the strongest modulations run along the a and b axes. At high energies, the strongest modulations run along the x and y axes. At intermediate energies, both orientations are apparent. We expect multiple modulations to be present across all energies, but there is no way they can all be discerned in real space by eye.

A note on image size & resolution

It is important to choose carefully the data image size and resolution. Ideally, all measurements would be instantaneous, and we would have time to measure an arbitrarily large field of view with arbitrarily fine resolution. But in practice, we are limited by measurement time. Doubling the linear dimension of the image quadruples the time, as does doubling the image resolution. So with a finite amount of time to make a measurement, we must prudently balance the advantages of large images and fine resolution.

A large $\vec{R}$-space image leads to fine $\vec{q}$-space resolution, while a fine $\vec{R}$-space resolution leads to large $\vec{q}$-space image. In order to look for weakly dispersing $\vec{q}$-vectors, we need $\vec{q}$-space resolution ~1% of the Brillouin zone, which means that our $\vec{R}$-space image must have extent at least $100a_0$ = 383 Å. In order to see all $\vec{q}$-vectors, we must have $\vec{q}$-space extent

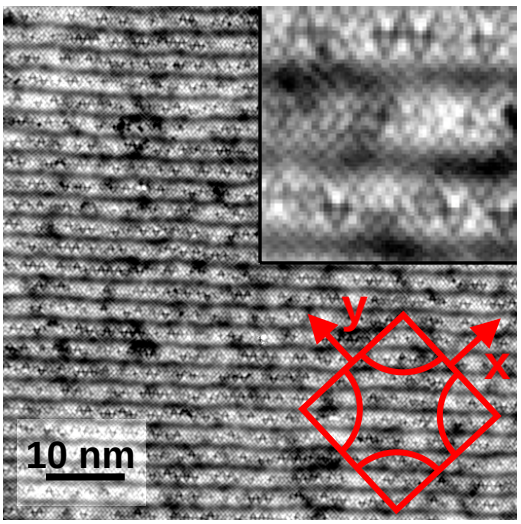

(a) Topography (inset magnification: ×2)

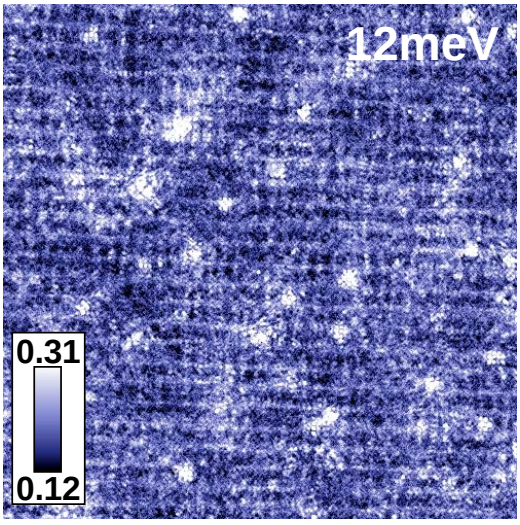

(b) 12 meV LDOS

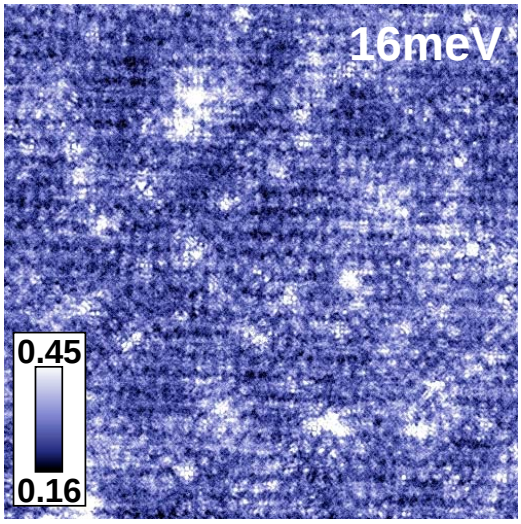

(c) 16 meV LDOS

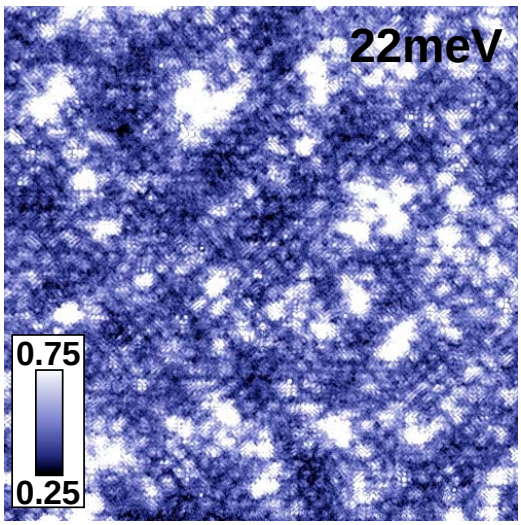

(d) 22 meV LDOS

Figure 3.13: Four unprocessed images of a single 650 Å field of view with 1.3 Å resolution. All measurements reported in this paper were obtained at a junction resistance of 1 GΩ set at a bias voltage of -100 mV, so the total junction conductance is 10^3 picoSiemens (pS). All LDOS images were acquired with a bias modulation amplitude of 2 mV root mean square. From the atomic resolution in (a) one can see the direction of the Cu-O bonds and the incommensurate supermodulation of wavelength $\sim$ 26 Å at 45° to the bonds. A cartoon showing the relative orientation of the Brillouin zone is superimposed in red. The LDOS images show checkerboard-like modulations of the LDOS: (b) 45° to the Cu-O bonds at $\vec{q}_7 \sim 0.21(\pm 2\pi/a_0, \pm 2\pi/a_0)$; (c) both 45° to and along the Cu-O bonds at $\vec{q}_7 \sim 0.25(\pm 2\pi/a_0, \pm 2\pi/a_0)$ but also at $\vec{q}_1 \sim 0.22(0, \pm 2\pi/a_0)$ and $\vec{q}_1 \sim 0.22(\pm 2\pi/a_0, 0)$; (d) along the Cu-O bonds at $\vec{q}_1 \sim 0.20(0, \pm 2\pi/a_0)$ and $\vec{q}_1 \sim 0.20(\pm 2\pi/a_0, 0)$.

at least twice the size of the first Brillouin zone, which means that our $\vec{R}$-space resolution must be at least 1 pixel per $a_0/2 = 1.9$ Å. This relationship is demonstrated in figure 3.14.

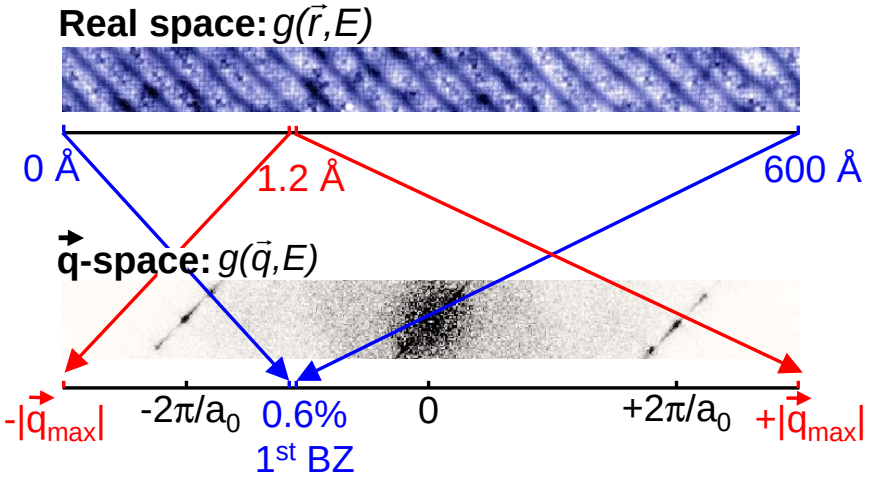

Figure 3.14: Relationship between $\vec{R}$-space and $\vec{q}$-space resolution. By choosing a $\vec{R}$-space image with size 600 Å and resolution 1 pixel per 1.2 Å, we arrive at a $\vec{q}$-space image with size 3 Brillouin zones, and resolution 0.6% of a Brillouin zone.

3.3 Analysis

To explore the evolution of all these LDOS modulations with energy, I compute the magnitude of the Fourier transform, $|\mathrm{FT}(E, \vec{q})|$, shown in figure 3.15. In Fourier space ($\vec{q}$-space) we can clearly visually separate the different coexisting modulations; each appears as a distinct bright spot in the Fourier transform. By comparing these maps with the joint-DOS prediction in figure 3.10, we can already see qualitatively that all the peaks are present and in approximately the correct positions.

In the remainder of this chapter, I will focus on the two inner points $\vec{q_1}$ and $\vec{q_7}$, as labeled in figure 3.4. First, $\vec{q_1}$ is oriented toward the $(\pm\pi, 0)$ and $(0, \pm\pi)$ direction. It appears at finite $|\vec{q}|$ at very low energy and then moves steadily inwards towards $(0, 0)$ (i.e. $|\vec{q_1}|$ decreases as E increases). Second, $\vec{q_7}$ is oriented along the $(\pm\pi, \pm\pi)$ direction. It appears and moves steadily to larger $|\vec{q}|$ with increasing energy (i.e. $|\vec{q_7}|$ increases as E increases). These same phenomena associated with $\vec{q_1}$ and $\vec{q_7}$ have been observed for all eight samples we have studied in this manner, but the exact dispersion of the peaks varies systematically with doping.

In figure 3.16, I plot the measured value of $|\mathrm{FT}(E, \vec{q})|$ versus $|\vec{q}|$ along the $(\pi, 0)$ and

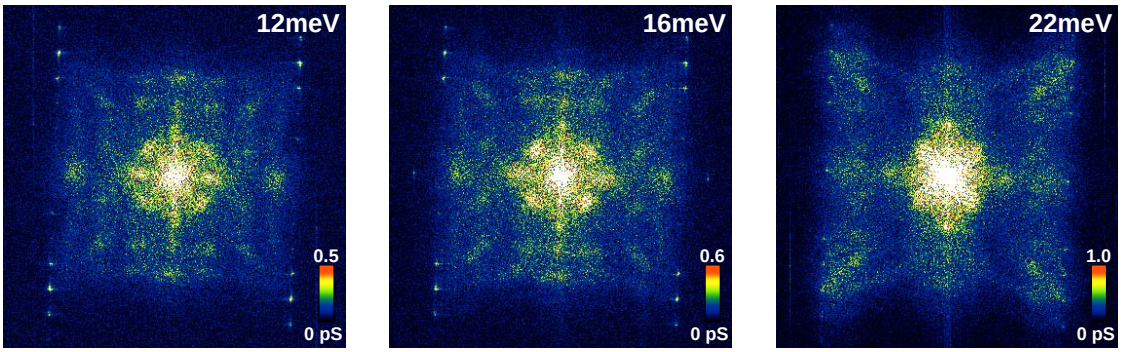

(a) 12 meV |FT(DOS)| (b) 16 meV |FT(DOS)| (c) 22 meV |FT(DOS)|

Figure 3.15: Fourier transforms of the 3 LDOS images shown in figure 3.13. The local maxima in these images represent the dominant $\vec{q}$'s associated with quasiparticle scattering at each energy E. The innermost scattering wavevectors oriented parallel to $(\pm\pi, 0)$ and $(0, \pm\pi)$ become shorter as energy rises. In contrast, the innermost scattering wavevectors oriented parallel to $(\pm\pi, \pm\pi)$ become longer as energy rises. The harmonics of the supermodulation are sharp features observed at the same location in all FT$(E, \vec{q})$ images.

(π, π) directions, at several energies, for an underdoped sample with $\bar{\Delta} = 50.2$ meV. These cuts pass directly through peaks $\vec{q}_1$ and $\vec{q}_7$, respectively. The locations of the $|\mathrm{FT}(E, \vec{q})|$ peaks are measured by fitting an exponential decay plus a Lorentzian. The dispersion in the unprocessed data is obvious. In figure 3.17, I show the energy dependence of the peaks in FT$(E, \vec{q})$ for $\vec{q}$-vectors oriented toward the $(\pi, 0)$ direction $[\vec{q}_1(E)]$, and towards the (π, π) direction $[\vec{q}_7(E)]$. The dispersions of these two types of conductance modulations were analyzed in detail for data for three of the samples. One is underdoped with mean energy gap value $\bar{\Delta} = 50.2$ meV (red squares), the second is near optimal with $\bar{\Delta} = 43.7$ meV (green circles), and the third is slightly overdoped with $\bar{\Delta} = 36.7$ meV (blue triangles). In general, one can see that at fixed E, $\vec{q}_1(E)$ becomes shorter, whereas $\vec{q}_7(E)$ becomes longer, as the doping is increased.

Now we compare our $\vec{q}$-space data quantitatively with the directly measured ARPES $\vec{k}$-space data. Consider first the $\vec{q}_1$ data from the $(\pi, 0)$ direction, which corresponds to the blue arrow in figure 3.2(b). These wavevectors are parallel to $(0, \pm\pi)$ or $(\pm\pi, 0)$ but have different $|\vec{q}_1|$ depending on the value of Δ at the points being connected. We estimate the expected $\vec{q}_1(\Delta)$ in our model using ARPES measurements of $|\Delta(\vec{k})|$ and locations of $\vec{k}_{FS}$.[57] The result is shown as grey bands in figure 3.17(a). The ARPES-derived results and our measured $\vec{q}_1$ are in excellent quantitative agreement. With increasing doping, the measured range of $\vec{q}_1$ becomes systematically shorter, as shown in figure 3.17(a). This would

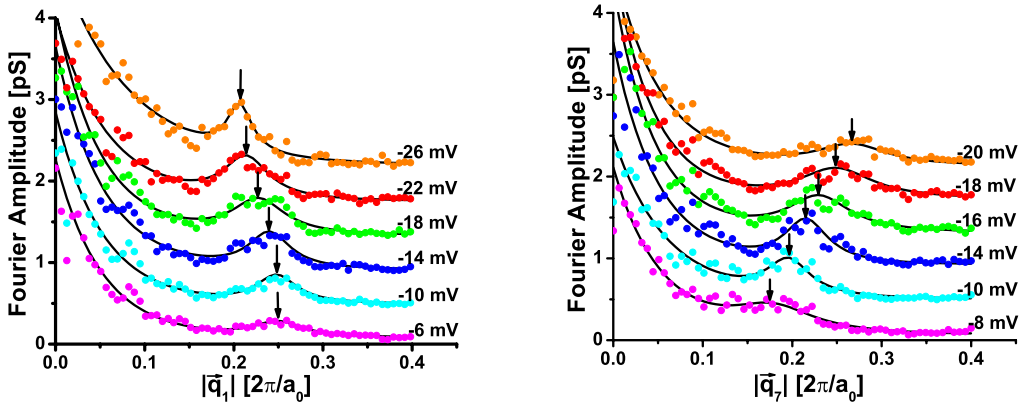

(a) $(\pi, 0)$ direction: $\vec{q_1}$

(b) (π, π) direction: $\vec{q_7}$

Figure 3.16: The amplitude of FT$(E, \vec{q})$ versus $|\vec{q}|$ along (a) the $(\pi, 0)$ direction and (b) the (π, π) direction are shown for six quasiparticle energies. The data are shifted vertically relative to each other by 0.4 pS for clarity. Each solid black line is a fit to an exponential decay from $\vec{q} = 0$ plus a Lorentzian peak. An arrow points to the local maximum in $|\vec{q}|$ for each energy.

be expected if increased hole density expands the hole pocket and moves the almost-parallel sections of the Fermi surface closer together.

Now consider the $\vec{q}_7$ data from the (π, π) direction, which corresponds to the red arrow in figure 3.2(b). The $\vec{q}_7$ peaks evolve very differently with energy than those oriented toward $(\pi, 0)$. Their dispersion has opposite sign and is substantially faster. We consider scattering that connects the same range of $\vec{k}$-states on the Fermi surface as for the $(\pi, 0)$-oriented process, but now diagonally across the inside of the hole pocket by the vector $\vec{q}_7$ parallel to (π, π) (Fig. 1, red arrows). We can again estimate the expected $|\vec{q}_7(\Delta)|$ using ARPES data.[57] The result is shown as a grey band in figure 3.17(b). The ARPES-derived results and our measured $\vec{q}_7(E)$ are in excellent quantitative agreement. Furthermore, with increasing doping, the range of $\vec{q}_7(\Delta)$ moves to higher values, again as expected if increased hole density increases the area of the hole pocket and the distance between relevant sections of the Fermi surface.

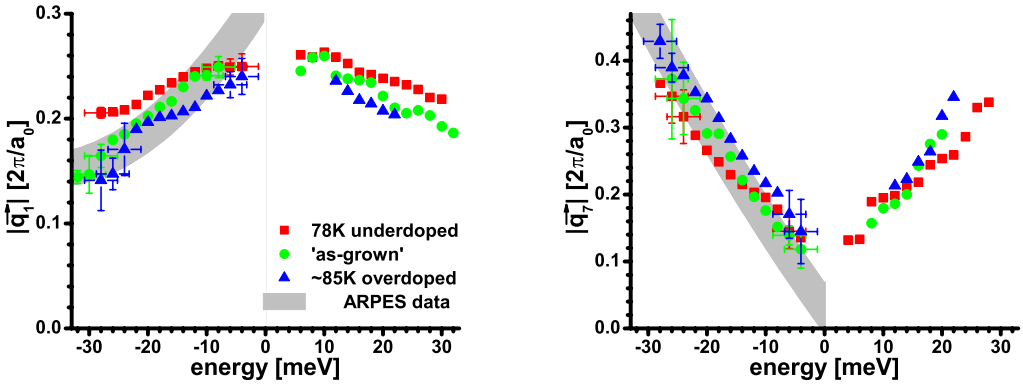

(a) $(\pi, 0)$ direction: $\vec{q_1}$

(b) (π, π) direction: $\vec{q_7}$

Figure 3.17: The measured $\vec{q}(E)$ for (a) the $(\pi, 0)$ direction and (b) the (π, π) direction are plotted for samples of three different dopings. The error bars shown at the end of the data ranges are representative of the uncertainty in identifying the location due to the peak width. The shaded grey bands represent the expected dependence $\vec{q}(E)$ derived from ARPES using the model described in the text. Note that ARPES measures only the electron-like portion of the spectrum. The width of the band represents uncertainties in the published ARPES data. These ARPES data from a $T_c = 87$ K Bi-2212 sample[57] should be compared with data from our similarly doped sample (green circles), which are in excellent agreement with the simplified model.

3.4 Sources of Scattering

Does disorder cause the scattering?

There is much evidence from experiments other than STM that quasiparticle scattering is important in BSCCO. For example, THz spectroscopy shows that low-temperature quasiparticle mean free paths in optimal BSCCO are about two orders of magnitude below that of optimal YBCO,[87] indicating that appreciable quasiparticle scattering exists in BSCCO. ARPES also shows a short quasiparticle lifetime for anti-nodal quasiparticles.[88]

With our spatially resolved tools, we ask what is the range of coherent quasiparticle interference patterns and where are the scattering centers? The smallest $\vec{q}$-space extent of any FT$(E, \vec{q})$ peak in figure 3.16 is $\Delta q \sim 0.1\pi/a_0$. This indicates that the longest coherence length for any modulation is $\ell \sim 80$ Å. Several phenomena such as Ni and Zn impurity resonances with spacing ∼100 Å (visible in figure 3.13), gap disorder with patch size ∼30 Å,[89, 90, 91, 92] or oxygen atoms with spacing ∼13 Å at this nominal doping, may influence this DOS modulation coherence length ℓ.

However, we observe qualitatively the same quasiparticle interference patterns independent of the concentration of Ni or Zn impurities. In fact, we see the quasiparticle interference patterns even in samples with no Ni or Zn impurities. Therefore the Ni and Zn impurities cannot be solely responsible for the quasiparticle interference. All samples have some native point defects, but a direct correlation between the point defects and the quasiparticle interference has not yet been possible.

We can also conclude from the joint-DOS modeling with coherence factors in figure 3.10 that there are significant sources of both magnetic and potential scattering. The experimental data shows all 16 quasiparticle interference peaks in $\vec{q}$-space, while either magnetic or potential scatterers alone would result in only 8 $\vec{q}$-space peaks.

Furthermore, in all samples there are multiple non-dispersing single-pixel "peaks" in the vicinity of each broader, dispersing $\vec{q}_i$ peak. Examples of these single-pixel peaks are shown in figure 3.18 for several samples. These non-dispersing single-pixel peaks can be explained as simply the power spectrum of a random impurity distribution, as described in figure 17 of Capriotti *et al.*[93] The fact that these single-pixel peaks do not appear at the same wave-vector from one sample to the next, or in fact even from the x-axis to the y-axis within the same sample, suggests that they result from disorder rather than from a more fundamental underlying order of fixed wavevector.

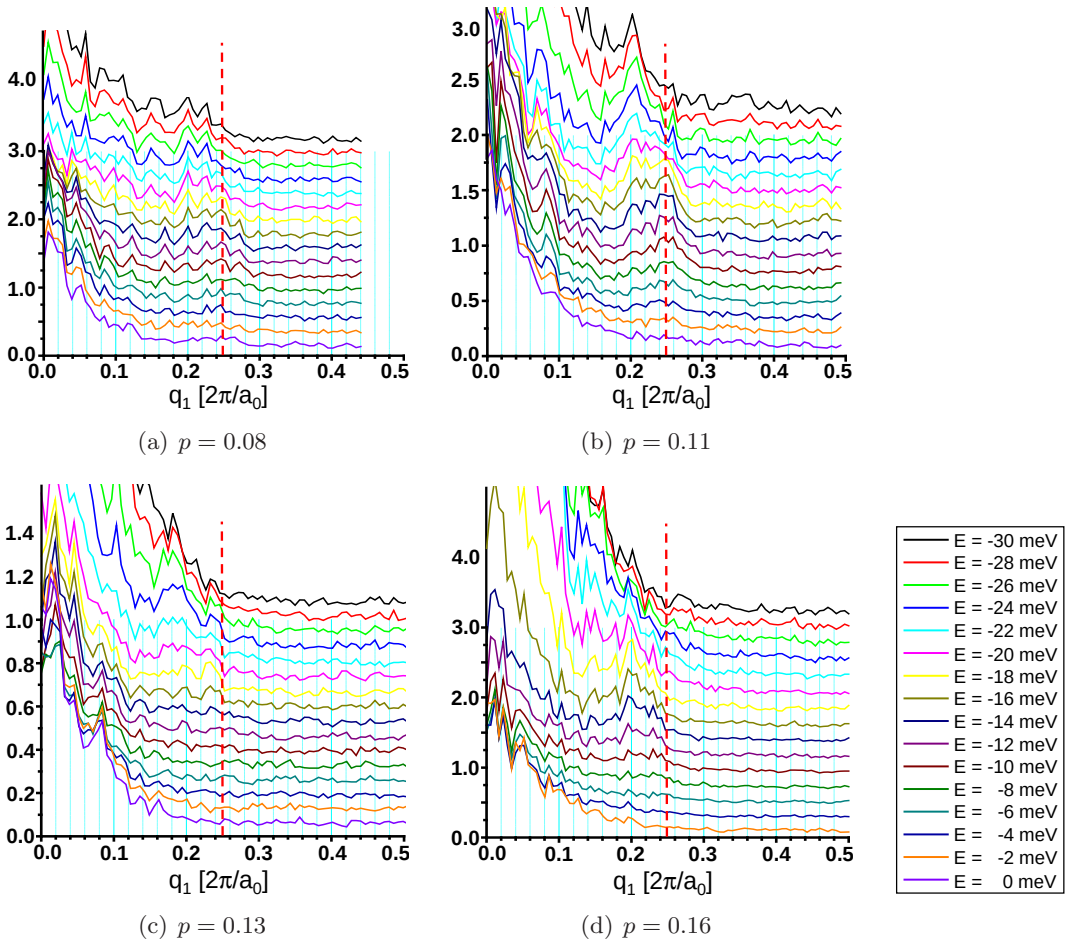

(a) $p = 0.08$ (b) $p = 0.11$

(c) $p = 0.13$ (d) $p = 0.16$

Figure 3.18: Single-pixel, non-dispersing $\vec{q}$-space peaks for four different samples. These peaks result from the power spectrum of the particular random impurity distribution in the field of view measured. A red vertical line is shown in each figure at $\vec{q} = 0.25[2\pi/a_0]$ for reference, to demonstrate that the single-pixel peaks occur at different values of $\vec{q}$ in each sample.

Does order cause the scattering?

We also consider the possibility that the observed quasiparticle interference patterns are caused primarily by scattering off an underlying charge or "stripe" order of fixed wavevector $\vec{q}_0$.[94, 95] According to equation 3.4, reproduced here,

$$w(i \to f) \propto \frac{2\pi}{\hbar}(u_{k_i}u_{k_f} \pm v_{k_i}v_{k_f})|V(\vec{q})|^2 n_i(E_i, \vec{k}_i)n_f(E_f, \vec{k}_f),$$

the scattering intensity is a product of the scattering potential $V(\vec{q})$ and the joint-DOS. If

the scattering potential consists solely of an underlying order of single fixed wavevector $\vec{q}_0$, then $V(\vec{q}) = \delta(\vec{q} - \vec{q}_0)$, so scattering intensity will be non-zero only at $\vec{q} = \vec{q}_0$. However, if the underlying order has a short coherence length L, due to disorder and/or pinning, then the scattering potential $V(\vec{q})$ will consist of a peak of finite width $\delta q \sim 1/L$ centered around $\vec{q}_0$. The scattering intensity will be enhanced at $\vec{q} = \vec{q}_0$, but because of the simultaneous influence of the joint-DOS, the wavevector of maximum scattering intensity may disperse across the range δq.

We can make a few relevant observations as follows. First, in all samples studied, we clearly see 16 dispersing bright spots in $\vec{q}$-space. In order to explain this solely as scattering off underlying order of fixed $\vec{q} = \vec{q}_0$, we would need 16 different underlying orders with 16 different fixed $\vec{q}_0$'s. Furthermore, some of these 16 underlying orders would need a very short coherence length, such that the width δq of the $V(\vec{q}_0)$ peak could accommodate the full dispersion of the joint-DOS wavevectors. The full dispersion is, for some $\vec{q}_i$'s, up to 30% of the Brillouin zone, meaning the underlying "order" would actually be disordered on a three unit cell length scale.

If the scattering is based on random disorder plus susceptibility to an underlying order,[95] we would expect a peak in scattering intensity at a specific $\vec{q}_0$. The intensity of dispersing $\vec{q}_i$'s we observe do peak at certain values. But the peak values appear to vary from one sample to another. For example, the scattering intensity vs. wavevector $\vec{q}_1$ is shown for three samples of different dopings in figure 3.19.

In conclusion, we do not see a single underlying order which has the same fixed wavevector $\vec{q}_0$ in each sample. Even within a single sample, the dispersing modulations we see cannot be explained wholly in terms of scattering off an underlying ordering of fixed wavevector, unless we postulate 16 underlying orders all coincidentally similar to the 16 wavevectors selected by the joint-DOS analysis. Furthermore, we caution against interpreting non-dispersing, high-intensity single pixels as signs of an underlying order; unless they are repeatable from sample to sample they must be just a remnant of the random disorder in each sample, as demonstrated in here in figure 3.18 and in figure 17 of Capriotti *et al.*[93]

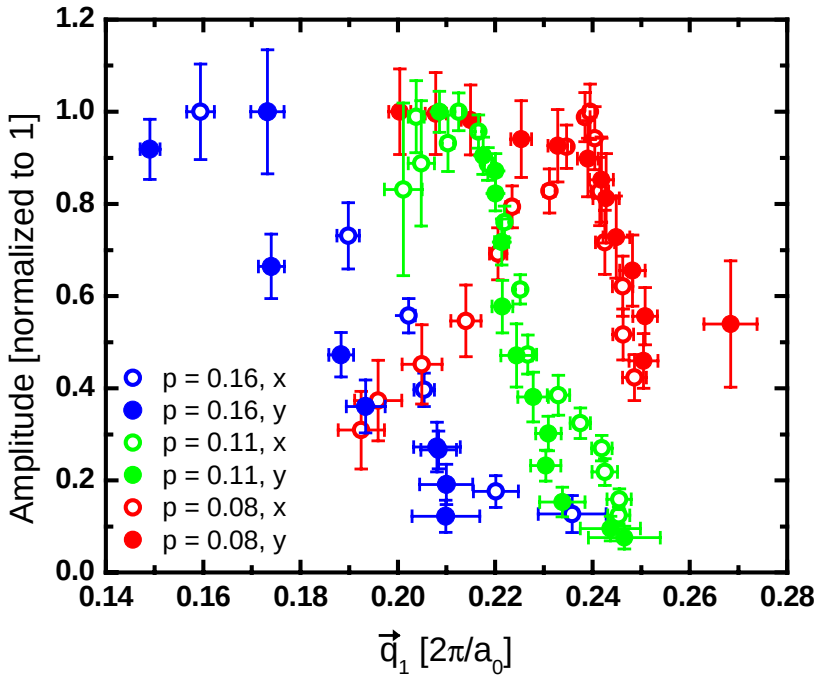

Figure 3.19: Scattering intensity vs. wavevector $\vec{q}_1$ for three samples of different doping. For each dI/dV map at each energy E, the relevant bright spot in $\vec{q}$-space was fit to find both the value of $\vec{q}_1$ and the area A under the $\vec{q}_1$ peak. Here the results are plotted as A vs. $\vec{q}_1$. To account for differences in tips, for each axis of each sample, the largest scattering intensity has been normalized to one. The wavevector $\vec{q}_1$ of maximum scattering intensity A increases with decreasing doping. This figure is, however, somewhat misleading. In order to extract the maximum susceptibility $\propto V(\vec{q})$ from the maximum scattering intensity, we would need to divide out by the joint-DOS. Since the joint-DOS increases with increasing energy, and $\vec{q}_1$ decreases with increasing energy, division by joint-DOS will shift the maximum susceptibility wavevectors to larger values, or shorter wavelengths. A more thorough analysis is needed.

3.5 Review of Related Studies

3.5.1 Prior STM measurements of Quasiparticle Interference

Although this work represents the first application of FT-STS to the cuprates, I would like to credit similar techniques which have previously been applied to other materials. STM studies of conductance modulations allowed the first direct probes of the quantum interference of electronic eigenstates in metals and semiconductors. Quasiparticle interference was first observed in copper at 4 K[96] then in gold at room temperature[97] due to step edges and impurities. Subsequent experiments on Cu and Ag[98] used a model of Friedel

oscillations[99] from a step edge to extract the quasiparticle lifetimes from the spatial decay length of the interference patterns. An experiment on sub-surface impurities in the semiconductor InAs used the energy dependence of the interference patterns surrounding the impurities to find the depth of the impurity below the surface and its scattering cross section.[100] A later experiment focused on a semiconductor 2DEG by studying a thin layer of InAs grown epitaxially on GaAs.[101] Quasiparticle standing waves have been imaged by STM in the conventional superconductor Nb due to adsorbed magnetic Mn or Gd impurity atoms.[102] The method of using LDOS modulations to reconstruct certain CCE in $\vec{k}$-space by analyzing the Fourier transform of the real-space LDOS(E) image has been employed before on anisotropic metals.[98, 103, 104]

3.5.2 Other DOS Modulation Measurements in Cuprates

For the cuprates in general, it had long been proposed that conductance modulations due to quasiparticle scattering should occur, and that both the homogeneous electronic structure and superconducting gap anisotropy could be extracted from measurement of their properties.[105] Dispersing one-dimensional quasiparticle interference patterns have previously been observed in the CuO chains of YBCO[24] due to unknown scatterers (possibly the configuration of the oxygen atoms themselves). However, no attempt was made to Fourier transform these dispersions or to match to a specific band structure in order to find the momentum space properties of the quasiparticles.

Howald *et al.* have observed $4a_0$ periodic LDOS modulations at $E = 25$ meV in BSCCO,[106] similar to the $\vec{q}_1$ modulations reported here, although Howald reports his modulations to be non-dispersing. Howald's modulations have been interpreted as stemming from the simultaneous existence of another electronic ordered-state. This interpretation was based on the apparent static nature of the modulations; however the $\vec{q}$-resolution of Howald's study was not high enough to rule out an unresolved dispersion.

Dung-Hai Lee first proposed the alternative quasiparticle interference explanation[86] for observed DOS modulations in BSCCO, which has been discussed in detail in this chapter. The higher resolution data shown here support the conclusion that observed conductance modulations stem from quasiparticle interference effects. The data in figure 3.15 appears to be due primarily to the quasiparticle interference effect because (i) all modulations have appreciable dispersion, (ii) the dispersions are consistent with scattering between the identified $\vec{k}$-space regions of high joint-DOS, and (iii) the evolution of the dispersions with doping is consistent with expected changes in the Fermi surface. Thus, it appears that quasiparticle band-structure effects play the primary role and must be understood before departures

from them can be ascribed to other order parameters.

Stronger "checkerboard" modulations around magnetic vortex cores[107] have also been observed, and will be discussed in chapter 4. Dispersion has *not* been detected in the vortex modulations, so it remains very likely that these two phenomena, although similar in appearance, actually stem from quite distinct physical origins.

3.5.3 Theories of Quasiparticle Scattering in Cuprates

Byers, Flatte and Scalapino[105] predicted originally in 1993 that quasiparticle scattering would be a useful tool to study the cuprates. Following the first theoretical explanation for our observations and verifying calculation by Wang and Lee,[86] there have been a number of additional theories exploring further details of the problem and providing suggestions for future experiments.

Zhang and Ting[108] commented on the existence of additional $\vec{q}$-space peaks. Pereg-Barnea and Franz[109] commented on the importance of coherence factors, and predicted the quasiparticle interference pattern for a possible QED3 phase. Bena *et al.*[110] predicted the quasiparticle interference pattern for a d-density wave (DDW) phase. Though these calculations provide a valuable ruler against which to measure the continuing search for alternative electronic order, they rely on a limited or unrealistic distribution of scatterers, and have had limited success matching the experimental data so far.

Zhu, Atkinson, and Hirschfeld,[111] working in the ordinary d-wave superconducting state, were able to incorporate a more realistic distribution of scatterers, including point scatters to simulate single atom defects, plus a continuously varying background potential to simulate the inherent gap disorder. This more realistic scattering model led to a much closer match between theory and experiment. However, so many parameters had to be tweaked to match the calculation to experiment, that the authors concluded the $\vec{q}$-vectors of the observed interference patterns were more dependent on incoherent scattering effects than on the joint-DOS. While this calculation has done an admirable job matching theory to experiment, the fact remains that the simple joint-DOS calculation of section 3.1.3 also matches the data quite well.

Podolsky *et al.*[95] has also focused attention on coexisting sources of scattering: both random point defects and underlying charge order. The search for underlying order coexisting with random disorder should revolve around the study of highest intensity $\vec{q}_i$'s, as shown in figure 3.19. The systematic dependence of these highest-intensity wavevectors on sample doping is suggestive of an increased susceptibility to a doping-dependent ordering.

This will be reported in more detail in a future paper by McElroy *et al.*

Vojta and Sachdev originally presented a theory of fluctuating spin density wave (SDW) order in the cuprates.[39] In a following paper, Polkovnikov, Vojta and Sachdev consider dynamic SDW fluctuations as the primary collective degree of freedom and couple it directly to the electrons.[112] The dynamic SDW fluctuations are pinned by disorder and result in a static LDOS modulation at a fixed wavevector whose intensity varies with energy. Following the STM experiments reported here, Polkovnikov, Sachdev and Vojta computed LDOS modulations in a model of electrons scattering off charge density wave order produced by the disorder-induced pinning of the fluctuating SDW, and were able to reproduce "many of the features observed in recent STM experiments."[113] Specifically, they focused on one dispersing wavevector in reasonable qualitative agreement with our observation of $\vec{q}_1$.

Han[114] similarly examines whether the observed dispersing LDOS modulations may be explained by a pinned fluctuating SDW order of fixed wavevector $\mathbf{Q}$. While he does find dispersing LDOS modulations resulting from his fixed wavevector starting point, the directions of the dispersions do not all agree with experiment. He concludes that the single $\mathbf{Q}$ SDW cannot account for our observations.

Andersen[115] shows that the different quasiparticle interference pattern resulting from scattering off two proximate non-magnetic impurities can be used to distinguish between a d–density wave phase, vs. another form of pairing without superconductivity, in the mysterious pseudogap regime.

Voo *et al.*[116] study a quasiparticle interference model on YBCO which has a $d_{x^2-y^2}+s$ order parameter resulting from the well-known orthorhombicity of the unit YBCO cell. They conclude that a single impurity scatterer will produce an anisotropic, quasi-one-dimensional quasiparticle interference pattern very similar in appearance to "stripes" but different in origin. Furthermore, they propose a distinguishing test: increasing the concentration of impurities would weaken a quasiparticle interference pattern because of the phase incoherence of randomly placed impurities. However, increasing the concentration of impurities should increase "stripe"-pinning and make "stripes" stand out more strongly.

Zhu *et al.*[117] point out the coupling between the magnetic resonance peak at energy ~ 40 meV and the superconducting gap Δ_0 at an impurity site. The magnetic resonance peak will have little effect on the impurity spectra at low energies, but at energies $\pm E_1 > \Delta_0$ the impurity will show an alternating modulation pattern of dips and humps in the spectra at $+E_1$ and $-E_1$ on-site, nearest neighbor, next nearest neighbor, etc.

Quasiparticle scattering between high joint-DOS regions of $\vec{k}$-space has now received

direct experimental support as a mechanism for incommensurate, dispersive, spatial modulations of the superconducting electronic structure. Incommensurate, dispersive modulations of the superconducting *magnetic* structure have also been observed in YBCO[66] and LSCO.[118] A related process, similar to our high joint-DOS scattering, in which a quasiparticle is scattered across the Fermi energy into a quasi-hole and vice versa, has been theoretically discussed as a potential explanation.[119, 120, 79, 83] Renewed exploration of such scattering-related explanations for these magnetic phenomena may therefore be appropriate.

3.6 Conclusion

In summary, I show via FT-STS that the dominant DOS modulations in optimally doped BSCCO can be well explained as quasiparticle interference. A simple model of the locations in $\vec{k}$-space of highest joint-DOS, "the octet model" quantitatively explains the data. There is no need to invoke alternative order parameters or other phases to explain the DOS modulations we observe in optimally doped BSCCO. However, this new experimental technique for looking at the cuprates and simultaneously accessing $\vec{R}$-space and $\vec{k}$-space quasiparticle information, has prompted a large body of new theoretical work, which in turn provides further promising directions for related experimental study.

Chapter 4

Vortex Checkerboard

There is no need to invoke alternative order parameters to explain observed DOS modulations in optimally doped $Bi_2Sr_2CaCu_2O_{8+\delta}$. To continue the search for interesting alternative order parameters in BSCCO (which might manifest themselves as DOS modulations), we must search in other areas of the high-T_c phase diagram. In this chapter, I will report on a search for alternative order parameters in BSCCO in high magnetic fields. The relationship of these studies to the phase diagram of BSCCO is shown in figure 4.1.

Scanning tunneling microscopy is used to image the additional quasiparticle states generated by quantized vortices in BSCCO. They exhibit a Cu-O bond oriented "checkerboard" pattern, with four unit cell ($\sim 4a_0$) periodicity and ~ 30 Å decay length. These electronic modulations may be related to the magnetic field-induced, $8a_0$ periodic, spin density modulations of decay length ~ 70 Å discovered in $La_{1.84}Sr_{0.16}CuO_4$.[65] One proposed explanation is a spin density wave localized surrounding each vortex core.[40] General theoretical principles predict that, in the cuprates, a localized spin modulation of wavelength λ should be associated with a corresponding electronic modulation of wavelength $\lambda/2$,[33, 37, 35, 48, 39, 36] in good agreement with our observations.

4.1 Low-T_c and Cuprate Vortex Phenomenology

In conventional s-wave type II superconductors, the superconducting order parameter is suppressed in the cores of quantized magnetic vortices, and recovers over a distance of about one coherence length ξ. Bound quasiparticle states can exist inside these cores[121] with lowest energy given approximately by $E \sim \Delta^2/2\varepsilon_F$, where ε_F is the Fermi energy and Δ is the superconducting gap. Such "core" states at the Fermi energy were first imaged by

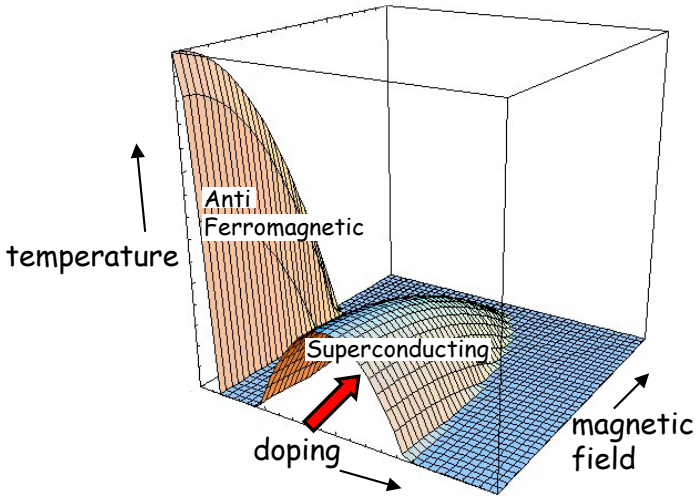

Figure 4.1: A schematic phase diagram of $Bi_2Sr_2CaCu_2O_{8+\delta}$. The red arrow shows the direction in phase space covered in this chapter. Optimally doped samples are studied at $T = 4.2$ K, while the B-field is increased to 7 Tesla.

Hess *et al.* using low temperature STM.[122]

A simple description of a vortex in an s-wave superconductor is a particle-in-a-box. In the vortex core, the superconducting order parameter is destroyed, so the quasiparticle has no binding energy and can exist freely. However, outside the vortex "box", the unattached quasiparticle has energy Δ greater than it would have if joined into a Cooper pair. So we can think of the quasiparticle as sitting in a circular potential well of height Δ and radius ξ. No matter how shallow the well, there will exist at least one bound state, which will decay exponentially outside the box.[123]

However, the cuprate superconductors have a $d_{x^2-y^2}$ order parameter. This means there are four gap nodes, which would imply that there are four holes in the walls of the vortex "box". So we might expect that such a leaky box would contain only scattering states, which decay as a power law with distance. Indeed, initial theoretical efforts focused on the quantized vortex in an otherwise conventional BCS superconductor with $d_{x^2-y^2}$ symmetry.[124, 125, 126, 127, 128] These models included predictions that, because of the gap nodes, the local density of electronic states (LDOS) inside the core is strongly peaked at the Fermi level. This peak, which would appear in tunneling studies as a zero bias conductance peak (ZBCP), should display a four-fold symmetric "star shape" oriented toward the gap nodes, and decaying as a power law with distance.

Scanning tunneling microscopy studies of HTSC vortices have revealed a very different electronic structure from that predicted by the pure d-wave BCS models. Vortices

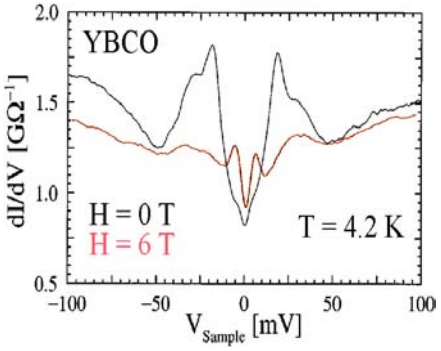

(a) $YBa_2Cu_3O_{7-\delta}$

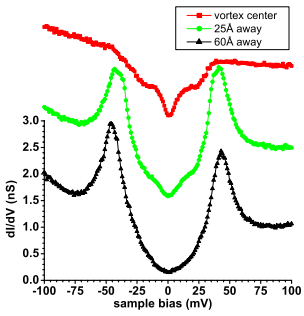

(b) $Bi_2Sr_2CaCu_2O_{8+\delta}$

Figure 4.2: Density of states spectra from (a) $YBa_2Cu_3O_{7-\delta}$ (from Maggio-Aprile *et al.*[129]) and (b) $Bi_2Sr_2CaCu_2O_{8+\delta}$ (adapted from Pan *et al.*[131]) Red traces show spectra inside the vortex cores, while black traces show spectra taken far from the vortices. In (b) we show also a spectrum at an intermediate distance (green trace), outside the vortex "core" but still clearly influenced by the vortex.

in $YBa_2Cu_3O_{7-\delta}$ (YBCO) lack ZBCPs but exhibit additional quasiparticle states at ± 5.5 meV,[129] whereas those in BSCCO also lack ZBCPs.[130] More recently, the additional quasiparticle states at BSCCO vortices were discovered at energies near ± 7 meV.[131] Typical DOS spectra from BSCCO and YBCO vortex cores are shown in figure 4.2.

Thus, a common phenomenology for low energy quasiparticles associated with vortices is becoming apparent. Its features include:

1. The absence of ZBCP's.
2. Low energy quasiparticle states at ± 5.5 meV (YBCO) and ± 7 meV (Bi-2212).
3. A radius for the actual vortex core (where the coherence peaks are absent) of $\sim$10 Å.[131]
4. A radius of up to $\sim$75 Å within which these states are detected, and apparently decay exponentially.[131]
5. The absence of a four-fold symmetric star-shaped LDOS.

In response to these discoveries, theorists began to play with the possibility that the superconducting order parameter has an additional component. For example, a smaller coexisting s component or a d_{xy} component would eliminate the gap nodes and could allow an exponentially decaying bound state to exist. However, these proposed components would have to have magnitude greater than the energy of the bound state (in order for it

to be bound). With bound states at 5.5 meV and 7 meV, the additional order parameter component would thus have magnitude at least 15-20% of the $d_{x^2-y^2}$ gap. It is unlikely that such a large order parameter of different symmetry could have escaped detection by other experimental methods such as ARPES.

So theorists turned to investigations of alternative, non-superconducting order parameters which may be competing with superconductivity, and may be able to appear where superconductivity is weakened or destroyed in and around the vortex core.

4.2 Theories of Alternative Ordered States

Theory indicates that the electronic structure of the cuprates is susceptible to transitions into a variety of ordered states as summarized in section 1.2.3.

Experimentally, antiferromagnetism (AF) and high temperature superconductivity (HTSC) occupy well known regions of the phase diagram, but outside these regions, several unidentified ordered states exist. For example, at low hole densities and above the superconducting transition temperature, the unidentified "pseudogap" state exhibits gapped electronic excitations.[132] Other unidentified ordered states, both insulating[133] and conducting,[134] exist in magnetic fields sufficient to quench superconductivity.

Because the suppression of superconductivity inside a vortex core can allow one of the alternative ordered states to appear there, the electronic structure of HTSC vortices has attracted wide attention.

Zhang[38] and Arovas *et al.*[135] first focused attention on magnetic phenomena associated with HTSC vortices with proposals that a magnetic field induces antiferromagnetic order localized by the core. More generally, new theories describe vortex-induced electronic and magnetic phenomena when the anticipated effects of strong correlations and strong antiferromagnetic spin fluctuations are included.[135, 40, 32, 136, 137] Common elements of their predictions include:

1. The proximity of a phase transition into a magnetic ordered state can be revealed when the superconductivity is weakened by the influence of a vortex.[135, 40, 32, 136, 137]

2. The resulting magnetic order, either spin[135, 40, 136] or orbital,[32, 137] will coexist with superconductivity in some region near the core.

3. This localized magnetic order will generate associated spatial modulations in the quasiparticle density of states.[40, 32, 136, 137]

Theoretical attention was first focused on the regions outside the core by a phenomenological model that proposed that the circulating supercurrents weaken the superconducting order parameter and allow the local appearance of a coexisting spin density wave (SDW) and HTSC phase[40] surrounding the core. In a more recent model, which is an extension of Zhang[38] and Arovas,[135] the effective mass associated with spin fluctuations results in an AF localization length that might be substantially greater than the core radius.[138] An associated appearance of charge density wave order was also predicted[139] whose effects on the HTSC quasiparticles should be detectable in the regions surrounding the vortex core.[40]

4.3 Experimental Evidence for Alternative Ordered States in Magnetic Fields

Other experimental information on the magnetic structure of HTSC vortices is available from inelastic and elastic neutron scattering on the lanthanum-copper-oxide family of high-T_c superconductors, and also nuclear magnetic resonance (NMR) studies on $YBa_2Cu_3O_{7-\delta}$.

4.3.1 Inelastic Neutron Scattering

Near optimum doping, some cuprates show strong inelastic neutron scattering (INS) peaks at the four $\vec{k}$-space points $(1/2 \pm \delta, 1/2)$ and $(1/2, 1/2 \pm \delta)$, where $\delta \sim 1/8$ and $\vec{k}$-space distances are measured in units of $2\pi/a_0$. This demonstrates the existence, in real space, of fluctuating magnetization density with spatial periodicity of $8a_0$ oriented along the Cu-O bond directions, in the superconducting phase. The first evidence for field-induced fluctuating magnetic order in the cuprates came from INS experiments on optimally doped $La_{2-x}Sr_xCuO_4$ (x=0.163) by Lake *et al.*[65] When $La_{1.837}Sr_{0.163}CuO_4$ is cooled into the superconducting state, the scattering intensity at these characteristic $\vec{k}$-space locations disappears at energies below ∼7 meV, opening up a "spin gap." Application of a 7.5 T magnetic field below 10 K causes the scattering intensity to reappear with strength almost equal to that in the normal state. These field-induced spin fluctuations have a spatial periodicity of $8a_0$ and wavevector pointing along the Cu-O bond direction. Their magnetic coherence length L_M is at least $20a_0$ although the vortex core diameter is only $\sim 5a_0$. This implies that magnetic ordering is taking place in the region *surrounding* the core.

4.3.2 Nuclear Magnetic Resonance

NMR studies by Mitrović *et al.*[72] explored the spatial distribution of magnetic fluctuations near the vortex core. NMR is used because $1/T_1$, the inverse spin-lattice relaxation time, is a measure of spin fluctuations, and the Larmor frequency of the probe nucleus is a measure of their locations relative to the vortex center. In near-optimally doped $YBa_2Cu_3O_{7-\delta}$ at $B = 13$ T, the $1/T_1$ of ^{17}O rises rapidly as the core is approached, then diminishes inside the core. This experiment is consistent with vortex-induced spin fluctuations occurring *outside* the core.

Spatially resolved NMR is used by Kakuyanagi *et al.*[140] to probe the magnetism in and around vortex cores of nearly optimally doped $Tl_2Ba_2CuO_{6+\delta}$ ($T_c = 85$ K). The NMR relaxation rate $1/T_1$ at the ^{205}Tl site provides direct evidence that the antiferromagnetic (AF) spin correlation is significantly enhanced in the vortex core region. This AF enhancement near the Tl-2201 vortices is a factor of two orders of magnitude, compared with a factor of 2-3 in YBCO. In the core region, Cu spins show a local AF ordering with moments parallel to the CuO_2 planes and Néel temperature $T_N = 20$ K. Kakuyanagi implies that the AF enhancement extends some distance outside of the vortex core, but claims still that the AF vortex core competes with superconductivity.

4.3.3 Elastic Neutron Scattering

More recently, elastic neutron scattering experiments were performed on related compounds in the lanthanum-copper-oxide family of high-T_c superconductors. While inelastic neutron scattering probes spin dynamics, elastic neutron scattering probes static spin order.

Studies by Khaykovich *et al.*[68] on La_2CuO_{4+y}, found field-induced enhancement of elastic neutron scattering (ENS) intensity at these same incommensurate $\vec{k}$-space locations, but with $L_M > 100a_0$. Thus, field-induced static AF order with $8a_0$ periodicity exists in this material. They were not able to perform measurements in fields above 9 T, but an extrapolation of the observed increase in static spin ordering to higher fields predicted that the whole area of the sample would be spin-ordered at an applied field well below H_{c2}, implying that static AF order and SC can coexist *in the same area* in La_2CuO_{4+y}.

A second elastic neutron scattering experiment was performed by Lake *et al.*[46] on underdoped $La_{2-x}Sr_xCuO_4$ (x=0.10). This experiment showed that static spin order was absent at temperatures $T > T_c$. But below T_c, static spin order increased with decreasing T and with increasing applied field H. At $T = 2$ K and $H = 14.5$ T, the order has an in-plane correlation length of $\zeta > 400$ Å, which is much greater than the vortex core size, and greater

even than the vortex-vortex separation distance of 130 Å, implying again that AF and SC coexist *at the same spatial location* in underdoped LSCO. Perhaps most significantly, Lake showed that the square ordered moment per Cu site increased as $M^2 H/H_{c2} \ln(H_{c2}/H)$ (with $M^2 = 0.12\mu_B^2$ per Cu^{2+}), in excellent quantitative agreement with the coupled SDW + SC theory of Demler *et al.*[40]

4.4 STM Vortex Data in $Bi_2Sr_2CaCu_2O_{8+\delta}$

All of the neutron scattering and NMR data implies a coexisting magnetic order and superconductivity, but since none of these probes are real space probes, there is no direct picture of the two orders coexisting in the same location in the crystal. We need a real space probe like an STM to look for other types of ordering in superconducting regions of the crystal (i.e. regions outside the vortex core). All of the neutron scattering data indicates a spin order with periodicity $8a_0$. We cannot look for spin order directly, but we expect a coupled charge order with period $4a_0$.

To test for DOS modulations on these length scales, we need higher resolution maps of the vortices first imaged by Pan *et al.*[131] For these experiments, I show data from two different crystals: (1) "As-grown" BSCCO crystals are generated by the floating zone method, are slightly overdoped with $T_c = 89$ K, and contain 0.5% substitution of Ni impurity atoms. (2) "As-grown" BSCCO crystals are generated by the floating zone method, are slightly underdoped with $T_c = 84$ K, and contain a nominal 0.6% substitution of Zn impurity atoms. Unprocessed topographies and DOS maps at the vortex state energy +7 meV are shown in figure 4.3.

The most detailed study of the vortices was made using the Ni-doped sample, which will be discussed in the remainder of this chapter. To study effects of the magnetic field B on the superconducting electronic structure, we first acquire zero-field maps of the differential tunneling conductance ($g = dI/dV$) measured at all locations (x, y) in the field of view (FOV) of figure 4.3(b). Because $\mathrm{LDOS}(E = eV) \propto g(V)$ where V is the sample bias voltage, this results in a two dimensional map of the local density of states $\mathrm{LDOS}(E, x, y, B = 0)$. We acquire these LDOS maps at energies ranging from -12 meV to +12 meV in 1 meV increments. The B field is then ramped to its target value and, after any drift has stabilized, we re-measure the topograph with the same resolution. The FOV where the high-field LDOS measurements are to be made is then matched to that in figure 4.3(b) within 1 Å ($\sim 0.25a_0$) by comparing characteristic topographic/spectroscopic features. Finally we acquire the LDOS maps, $\mathrm{LDOS}(E, x, y, B \neq 0)$, at the same series of energies as the zero-field case.

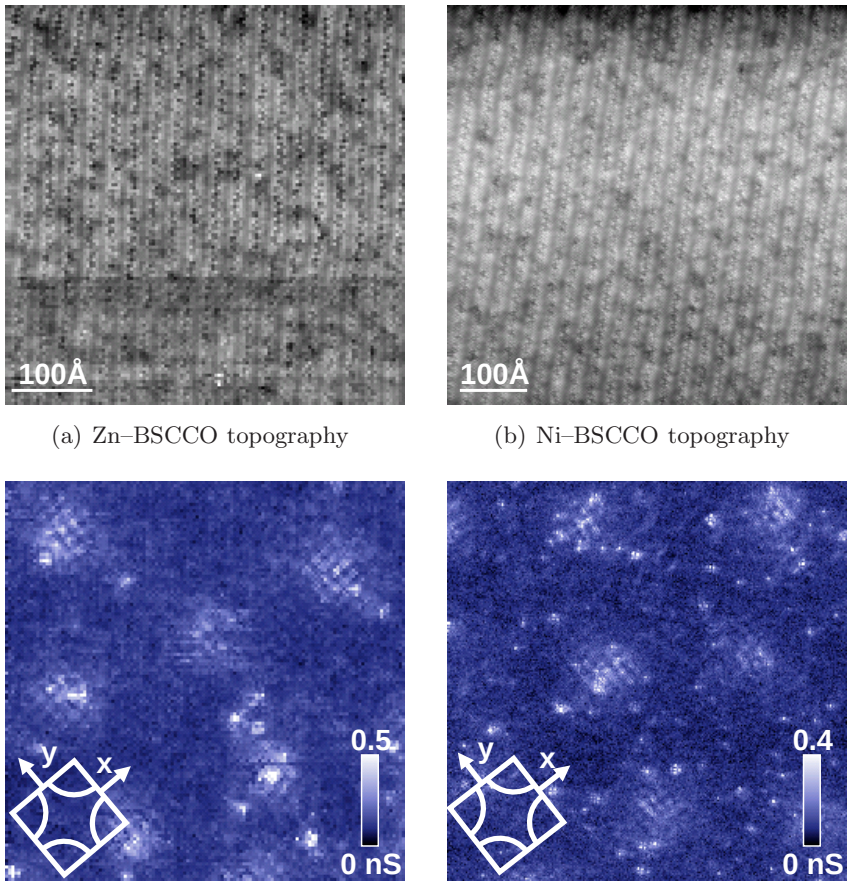

(a) Zn–BSCCO topography

(b) Ni–BSCCO topography

(c) Zn–BSCCO, 8 meV DOS

(d) Ni–BSCCO, 7 meV DOS

Figure 4.3: Raw data: topographies and density of states maps for two distinct samples. Panel (a) shows a topographic image of a 490 Å square area of Zn-doped $Bi_2Sr_2CaCu_2O_{8+\delta}$. Panel (c) shows the DOS in the same area at +8 meV in an applied field $B = 7$ T. Panel (b) shows a topographic image of a 586 Å square area of Ni-doped $Bi_2Sr_2CaCu_2O_{8+\delta}$. Panel (d) shows the DOS in the same area at +7 meV in an applied field $B = 5$ T. In panels (a) and (b), the supermodulation (with wavelength ~ 26 Å) is clearly visible, at 45° to the Cu-O bond directions. In panels (c) and (d), schematics of the Brillouin zone show the x and y crystal axes (whose directions can also be discerned from the raw data in the topographies). In both DOS images (c) and (d), approximately 6 vortices can be seen, with a "checkerboard"-like pattern oriented along the x and y axes with approximately $4a_0$ periodicity. This checkerboard is qualitatively the same in two samples with very different types of impurities (and also in a nominally impurity-free sample, not shown here).

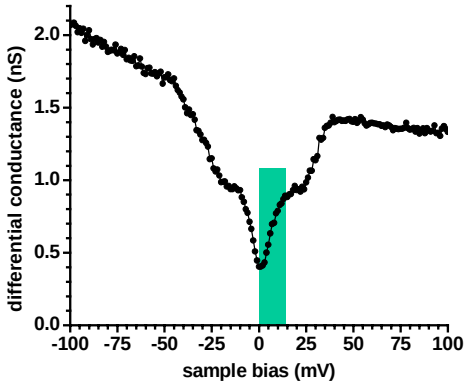

Figure 4.4: The vortex-induced LDOS is centered at energy $E = 7$ meV, but has significant weight over a range of energies around 7 meV. We integrate over energies from 1 to 12 meV to maximize the vortex-induced signal.

4.5 Analysis

We can clearly see the checkerboard ordering inside the vortices in the raw data in figures 4.3(c) and 4.3(d), but other effects (such as the impurity resonances) are distracting and inhibit our ability to obtain an accurate measure of the wavelength of the structure. So we employ several tricks:

1. Integrate the maps over all energies influenced by the vortices, so as to capture all the signal under the peak centered at 7 meV, rather than just the signal from the single energy 7 meV. This is demonstrated in figure 4.4.

2. Subtract the zero-field-integrated data from the field-integrated data, to remove effects from impurities and other inhomogeneities which don't change with field. This is demonstrated in figure 4.5.

3. Take a Fourier transform to obtain an accurate measure of the wavelength. This is demonstrated in figure 4.6(a).

To focus preferentially on B field effects, we define a new type of two dimensional map:

$$S_{E_1}^{E_2}(x,y,B) = \sum_{E_1}^{E_2} \left[\mathrm{LDOS}(E,x,y,B) - \mathrm{LDOS}(E,x,y,0)\right] dE \tag{4.1}$$

which represents the integral of all additional spectral density induced by the B field between the energies E_1 and E_2 at each location (x,y). This technique of combined energy

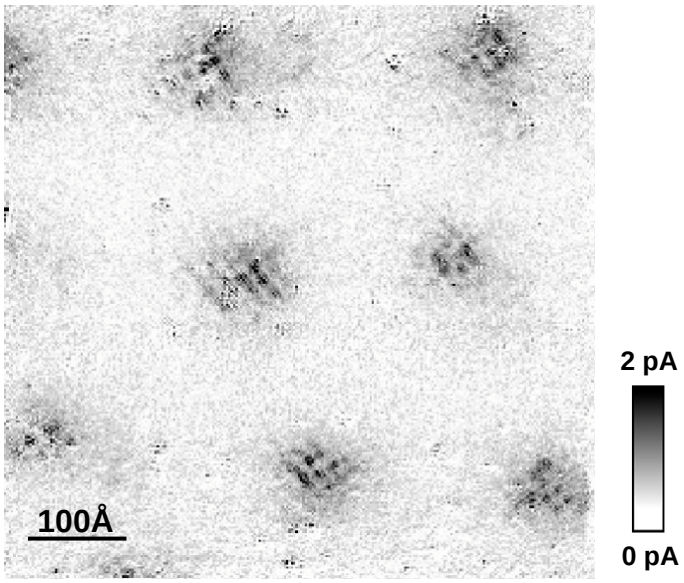

Figure 4.5: A map of $S_1^{12}(x, y, 5)$ showing the additional LDOS induced by the seven vortices. Each vortex is apparent as a "checkerboard" at 45° to the page orientation. Not all are identical, most likely due to the effects of electronic inhomogeneity. The units of $S_1^{12}(x, y, 5)$ are picoAmps because it represents $\sum dI/dV \cdot \Delta V$. In this energy range, the maximum integrated LDOS at a vortex is $\sim$ 3 pA, as compared with the zero field integrated LDOS of $\sim$ 1 pA. The latter is subtracted from the former to give a maximum contrast of $\sim$ 2 pA. We also note that the integrated differential conductance between 0 mV and -200 mV is 200 pA because all measurements reported in this paper were obtained at a junction resistance of 1 GΩ set at a bias voltage of -200 mV.

integration and electronic background subtraction greatly enhances the signal-to-noise ratio of the vortex-induced states. In BSCCO, these states are broadly distributed in energy around ±7 meV,[131] so $S_{\pm 1}^{\pm 12}(x, y, B)$ effectively maps the additional spectral strength under their peaks.

Figure 4.5 is an image of $S_1^{12}(x, y, 5)$ measured in the FOV of figure 4.3(d). The locations of seven vortices are evident as the darker regions of dimension ∼100 Å. Each vortex displays a spatial structure in the integrated LDOS consisting of a "checkerboard" pattern oriented along the Cu-O bonds. We have observed spatial structure with the same periodicity and orientation, in the vortex-induced LDOS on multiple samples and at fields ranging from 2 to 7 Tesla.

In all 35 vortices studied in detail, this spatial and energetic structure exists, but the "checkerboard" is more clearly resolved by the positive-bias peak. This energy asymmetry may be due to the asymmetric set-up condition of the STM which determines the tip height

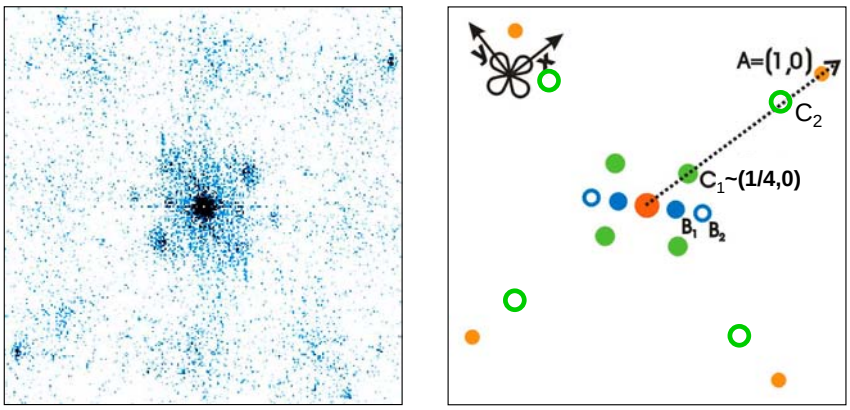

(a) Power spectrum data (b) Power spectrum schematic

Figure 4.6: Fourier transform analysis of vortex-induced LDOS. (A) PS$[S_1^{12}(x,y,5)]$, the two dimensional power spectrum of the $S_1^{12}(x,y,5)$ map shown in figure 4.5. The four points near the edges of the figure are the $\vec{k}$-space locations of the square Bi lattice. The vortex effects surround the $\vec{k}=0$ point at the center of the figure. (B) A schematic of the PS$[S_1^{12}(x,y,5)]$ shown in (A). Distances are measured in units of $2\pi/a_0$. Peaks due to the atoms at $(0,\pm1)$ and $(\pm1,0)$ are labeled A. Peaks due to the supermodulation are observed at B_1 and B_2. The four peaks at C_1 and their companions at C_2 occur only in a magnetic field and represent the vortex-induced effects at k-space locations $(0,\pm1/4)$ and $(\pm1/4,0)$ and $(0,\pm3/4)$ and $(\pm3/4,0)$.

while imaging: the tip height is fixed by requiring the total tunneling current be 100 pA while the sample is biased at -100 mV, thus fixing the integral of the density of states out to -100 meV below the Fermi level. It's possible that if the setup condition instead fixed the integrated density of states up to 100 meV above the Fermi level, we would see the vortex pattern more clearly at negative energies. (We have not yet carried out this experiment.)

We show the power spectrum from the two-dimensional Fourier transform of $S_1^{12}(x,y,5)$, PS$[S_1^{12}(x,y,5)]$ = |FT$[S_1^{12}(x,y,5)]|^2$, in figure 4.6(a) and a labeled schematic of these results in figure 4.6(b). In these $\vec{k}$-space images, the atomic periodicity is detected at the points labeled by A, which by definition are at $(0,\pm1)$ and $(\pm1,0)$. The harmonics of the supermodulation are identified by the symbols B_1 and B_2. These features (A, B_1, and B_2) are observed in the Fourier transforms of all LDOS maps, independent of magnetic field, and they remain as a small background signal in PS$[S_1^{12}(x,y,5)]$ because the zero-field and high-field LDOS images can only be matched to within 1 Å before subtraction. Most importantly, PS$[S_1^{12}(x,y,5)]$ reveals new peaks at the four $\vec{k}$-space points which correspond to the spatial structure of the vortex-induced quasiparticle states. We label their locations C. No peaks of similar spectral weight exist at these points in the two-dimensional Fourier

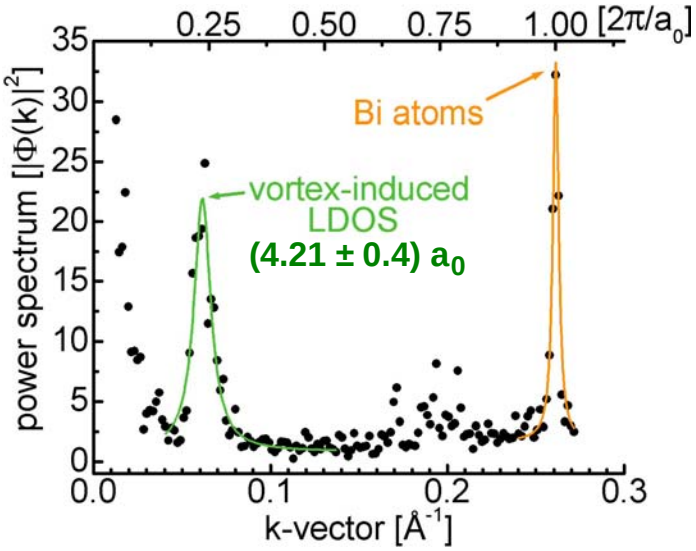

Figure 4.7: A trace of PS$[S_1^{12}(x, y, 5)]$ along the dashed line in figure 4.6(b). The strength of the peak due to vortex-induced states is demonstrated, as is its location in the $\vec{k}$-space unit cell relative to the atomic locations. The spectrum along the line toward (0,1) is equivalent but there is less spectral weight in the peak in PS$[S_1^{12}(x, y, 5)]$ at (0,1/4). Note also the weaker peak at $\sim$ (0, 3/4).

transform of these zero-field LDOS maps.

To quantify these results, we fit a Lorentzian to PS$[S_1^{12}(x, y, 5)]$ at each of the four points labeled C in figure 4.6(b). We find that they occur at k-space radius 0.062 Å^{-1} with width $\sigma = 0.011 \pm 0.002$ Å^{-1}. Figure 4.7 shows the value of PS$[S_1^{12}(x, y, 5)]$ measured along the dashed line in figure 4.6(b). The central peak associated with long wavelength structure, the peak associated with the atoms, and the peak due to the vortex-induced quasiparticle states are all evident. The vortex-induced states identified by this means occur at $(\pm 1/4, 0)$ and $(0, \pm 1/4)$ to within the accuracy of the measurement. Equivalently, the "checkerboard" pattern evident in the LDOS has spatial periodicity $\sim 4a_0$ oriented along the Cu-O bonds. Furthermore, the width σ of the Lorentzian yields a spatial correlation length for these LDOS oscillations of $L = (1/\pi\sigma) \approx 30 \pm 5$ Å (or $L \approx 7.8 \pm 1.3a_0$). This is substantially greater than the measured[131] core radius. It appears in figures 4.3(d) and 4.6(a) that the LDOS oscillations have stronger spectral weight in one Cu-O direction than in the other. The ratio of amplitudes of PS$[S_1^{12}(x, y, 5)]$ between $(\pm 1/4, 0)$ and $(0, \pm 1/4)$ is approximately three. But this could be explained by an asymmetric tip.

4.6 Interpretation

How might our observation of $\sim 4a_0$ periodic B-field-induced electronic structure relate to the spin structure[65, 72, 68, 46] of the HTSC vortex?

Antiferromagnetic Vortex Core

The original suggestion of an AF insulating region inside the core[38, 135] cannot be tested directly by our techniques, although the Fermi-level LDOS measured there is low, as would be expected for an AF insulator.[130, 131] However, the structure we see has periodicity $\sim 4a_0$, so the vortex core must have some additional structure beyond a simple AF state with $2a_0$ periodicity.

Staggered Flux Phase

The staggered flux phase[32] also cannot be directly tested via STM. But its predictions include a $2a_0$ periodic orbital magnetic order. Again, the structure we see has periodicity $\sim 4a_0$ so it cannot be explained by the SFP phase alone.

Stripes

Another possibility is that $8a_0$ periodic "stripes"[33, 37, 35, 48] are localized surrounding the core, but that two orthogonal configurations are apparent in the STM images because of fluctuations in a nematic stripe phase,[34, 141] or because of bilayer effects. This explanation gains some credibility from the fact that an $8a_0$ periodic spin structure is expected to be coupled to a half-wavelength $4a_0$ periodic charge structure, similar to what we observe.

Coexisting Spin Density Wave + Superconductivity

A more recent proposal is that when the HTSC order parameter near a vortex is weakened by circulating superflow, a coexisting SDW+HTSC phase appears, resulting in a local magnetic state $\mathbf{M}(r)$ surrounding the core.[40] A second proposal is that the periodicity, orientation, and spatial extent of the vortex-induced $\mathbf{M}(r)$ are determined by the dispersion and wavevector of the pre-existing zero field AF fluctuations.[138] In both cases, the $8a_0$ spatial periodicity of $\mathbf{M}(r)$ is not fully understood but is consistent with models of evolution of coupled spin and charge modulations in a doped antiferromagnetic Mott insulator.[39, 36]

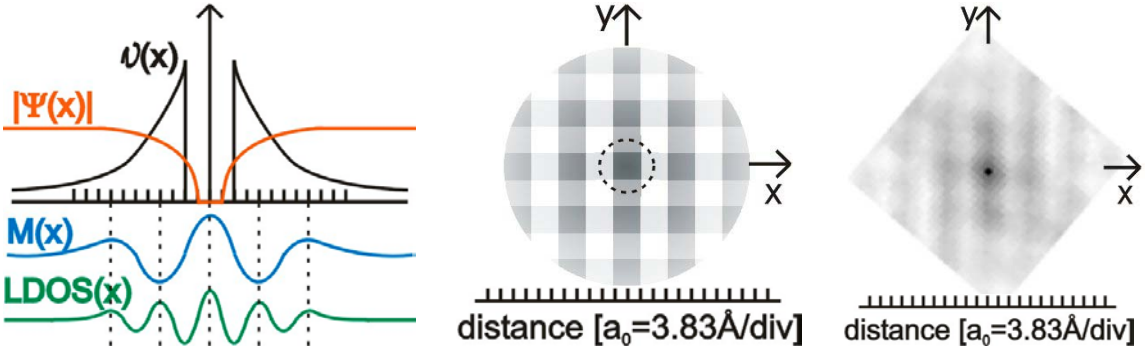

(a) Schematic (b) Schematic (c) Data

Figure 4.8: (a) Superfluid velocity $v(x)$ rises and the HTSC order parameter $|\Psi(x)|$ falls as the core is approached. The periodicity of the spin density modulation deduced from INS[65] is shown schematically as $\mathbf{M}(x)$. The anticipated periodicity of the LDOS modulation due to such an $\mathbf{M}(x)$ is shown schematically as LDOS(x). (b) A schematic of the two-dimensional "checkerboard" of LDOS modulations that would exist at a circularly symmetric vortex core with an $8a_0$ spin modulation as modeled in (a). The dashed line shows the location of the $\sim 5a_0$ diameter vortex core. The dark regions represent higher intensity low energy LDOS due to the presence of a vortex. They are $2a_0$ wide and separated by $4a_0$. (c) The two dimensional autocorrelation of a region of $S_1^{12}(x, y, 5)$ that contains one vortex. Its dimensions are scaled to match the scale of (a), and it is rotated relative to figure 4.3(d) so that the Cu-O bond directions are here horizontal and vertical.

Figure 4.8(a) shows a schematic of the superflow field and the magnetization $\mathbf{M}(r)$ localized at the vortex. Almost all microscopic models predict that magnetic order localized near a vortex will create characteristic perturbations to the quasiparticle LDOS.[40, 32, 136, 137, 139] In addition, general theoretical principles about coupled charge- and spin-density-wave order parameters[33, 37, 35, 48, 39, 36] indicate that spatial variations in $\mathbf{M}(r)$ must have double the wavelength of any associated variations in the LDOS(r). Thus, the perturbations to the LDOS(r) near a vortex should have $4a_0$ periodicity and the same orientation and spatial extent as $\mathbf{M}(r)$ as represented schematically in figure 4.8(a). In an LDOS image this would become apparent as a checkerboard pattern, shown schematically in figure 4.8(b). In figure 4.8(c), we show the autocorrelation of a region of figure 4.3(d) that contains one vortex, to display the spatial structure of the BSCCO vortex-induced LDOS. It is in good agreement with the quasiparticle response described by figures 4.8(a) and 4.8(b). Therefore, assuming equivalent vortex phenomena in LSCO, YBCO and BSCCO, the combined results from INS, ENS, NMR, and STM could lead to an internally consistent new picture for the electronic and magnetic structure of the HTSC vortex

4.7 Further Questions

Unfortunately we are unable to distinguish between the various scenarios in the previous section. Some questions we would like to ask in future experiments to address these scenarios are summarized here.

4.7.1 One-Dimensionality

Some degree of one-dimensionality is evident in these incommensurate LDOS modulations because one Cu-O direction has stronger spectral intensity than the other by a factor of approximately two.

However, this could easily be caused by a tip effect. An asymmetric tip will blur the DOS in one direction, but may still allow very high resolution in the orthogonal direction. The best way to check for an asymmetric tip is to image an isolated impurity with high resolution. If it appears distorted, then it's likely the tip is asymmetric. Another check is to look at the autocorrelation of an image: a double tip will show peaks in the autocorrelation at the length scale of the double tip.

Another possibility is that there is just so much disorder in the system (from at least 100 Ni atoms in the FOV, plus at least 10 other impurities of uncertain origin) that the pinning forces distort the vortices.

The best way to check for asymmetry would be to look at vortices far from impurities, with a tip which has been previously checked for asymmetry by imaging a single isolated impurity.

4.7.2 Dispersion

The vortex-induced modulations are the same orientation and a very similar wavelength to the $\vec{q}_1$ modulations discussed in the previous chapter. In fact, the wavelength of the $\vec{q}_1$ modulations disperses through the apparently static wavelength found here for the vortex modulations (although not at 7 meV). So we must ask, have we missed detecting a dispersion because we have integrated over the whole range of relevant energies from 1 meV to 12 meV?

The $\vec{q}_1$ peak disperses only weakly: from 0.22 to 0.25 of the Brillouin zone. In order to see this weak dispersion, we need $\vec{q}$-space resolution at least 1% of the Brillouin zone, which means we need a real field of view of size at least $100a_0 \approx 400$ Å. But the vortices are only ~ 100 Å, which gives us a $\vec{q}$-space resolution $\sim 4\%$ of the Brillouin zone. Even though

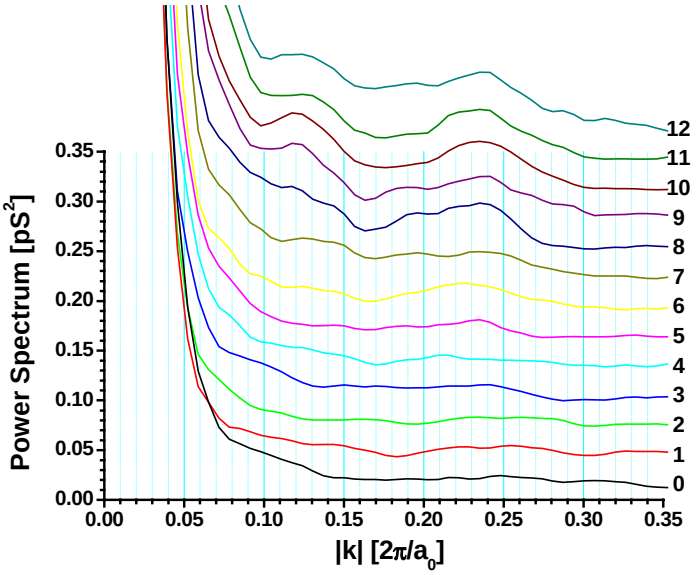

Figure 4.9: Search for dispersion in vortices. The non-integrated vortex power spectrum, extracted along the line in figure 4.6(b), is shown in figure for energies from 0 meV to 12 meV. The curves are smoothed for visual clarity.

we have seven vortices in our field of view, our resolution is increased only by a factor of $\sim \sqrt{7} = 2.6$. This would likely not be enough to definitively measure a dispersion. The non-integrated vortex power spectrum, extracted along the line in figure 4.6(b), is shown in figure 4.9 for energies from 0 meV to 12 meV.

The search for a dispersion of the vortex resonance is so far inconclusive. One possibility to detect or rule out a dispersion in the future might come from imaging vortices in higher magnetic fields. If, as neutron scattering experiments imply, the magnetic-field induced ordering comprises a larger and larger fraction of the area as the field is increased, until the ordering covers the whole area, then it is possible that we could achieve more $\vec{k}$-space resolution in high fields. In the foreseeable future, the highest possible field for this type of slow, high-resolution STM measurement is approximately 15 T.

4.7.3 Charge Density Wave

One way to check for a charge density wave is to look for a spatial phase flip across the Fermi level ε_F. The data shown here are not sufficiently well-resolved to determine whether there is a phase flip. Spatial resolution is only 1 pixel per 2 Å, but also there are too many impurities influencing the pinning and making it difficult to see clearly.

More importantly, these data were taken only with a negative setup condition (requiring the total current to be constant at a fixed negative bias voltage). These data should be retaken at higher spatial resolution, and with both positive and negative setup conditions, ideally on a sample with fewer impurities, to resolve the question of the phase flip and test definitively for a charge density wave.

Matsuba *et al.*[142] recently showed the first STM images of an ordered vortex lattice in BSCCO, which implies that their vortices are unpinned. Although their images are lower resolution, they do offer some support for the quasiparticle checkerboard we observed, and specifically for the increased strength and clarity of the positive-energy states. This is intriguing because they used an opposite setup condition: they required a constant current with a *positive* bias of +0.5 V on the sample, instead of a *negative* bias of -0.1 V as we used. Despite the opposite setup condition they also saw increased intensity for the positive-energy states. Before we draw any conclusions from this, we emphasize that the same group should measure both setup conditions in the same area of the same sample.

4.7.4 Field Dependence

The neutron scattering experiments all show an increase in spin ordering (both static order and fluctuating order, in different related compounds) on increasing applied B-field. It would be very useful to look at our vortex-induced DOS ordering as a function of applied B-field to see if it increases in strength with the same field dependence. STM is not a very reliable measure of absolute DOS amplitude, due to the tricky normalization procedure and related uncertainty of tip-sample separation. However, a careful study could be made of multiple fields on the same field of view with a few reliable impurity resonances to calibrate and cross-normalize the amplitude of maps taken at different field strengths. Or, the impurity resonances themselves may change with applied B-field, so another background signal might be needed instead for normalization. But as long as we can guard against a tip change while ramping the B-field, it seems likely that such a study is possible and will be very useful.

The Demler theory of coexisting spin density wave order plus superconductivity gives a clear quantitative prediction for the increase of SDW order with increasing applied H-field:

$$M^2 \propto H/H_{c2} \ln(H_{c2}/H) \tag{4.2}$$

Equation 4.2 governs spin ordering, but STM is sensitive to charge ordering. However, the two are predicted to be coupled, so we should do a careful study to look for an increase

in vortex-induced DOS modulations following equation 4.2. This would lend extra support to Lake's finding[92] that the static spin order obeys Demler's prediction,[40] and also give evidence to support the common assumption that the spin and charge order are coupled in the cuprates.

4.7.5 Doping Dependence

Ando and Boebinger have led experiments to investigate the transport properties of $La_{2-x}Sr_xCuO_4$, across a range of dopings x, in magnetic fields sufficient to quench superconductivity. They have found a significant crossover from unusual insulating behavior in underdoped,[133] to conducting in overdoped,[134] in very high magnetic fields.

We have so far investigated vortices in BSCCO samples only very close to optimally doped. It will be very important to look for differences in the induced order in further underdoped samples. If the induced order really is a charge density wave of some sort, we might expect it to be significantly enhanced in underdoped samples.

A recent experiment by Hoogenboom *et al.*[143] shows that the energy of the vortex-induced state varies systematically with the local gap in the neighborhood of the vortex. For larger local Δ (i. e. more underdoped) the vortex-induced resonance also has larger energy. However, the error bars on this study are large, and the import of the result is not clear, since the gap inhomogeneity has a length scale of ∼30 Å while the vortex-induced resonances appear over a ∼100 Å length scale, so the vortex-induced resonance may be influenced by several regions of very different local Δ. It would be useful to look again at this result with a number of samples of wider variation in bulk doping.

4.8 Conclusion

The vortex-induced electronic structure has some superficial similarities to quasiparticle interference. Both display $\sim 4a_0$ periodic CuO bond-oriented order. At $\sim$ 7 meV, the density of states pattern surrounding the vortex looks quite similar by eye to the quasiparticle interference density of states pattern filling all space in zero applied field at $\sim$ 10–20 meV.

However the vortex electronic structure is 10–100 times stronger than the quasiparticle interference. Also, while the zero-field quasiparticle interference varies with energy, the vortex electronic structure apparently doesn't disperse, although we can't know for sure from existing data. Furthermore, the quasiparticle interference shows 16 $\vec{q}$-space peaks, while the vortex structure shows only 4: $(1/4, 0)$, $(0, 1/4)$, $(3/4, 0)$, and $(0, 3/4)$. Since the

vortex electronic structure appears where we know the SC to be destroyed, it seems very likely that the vortex-induced electronic structure is evidence of another competing order. If so, it would be the first real-space image of a new periodic electronic state in the cuprates.

Independent of models of the vortex structure, the data reported here are important for several reasons. First, the $\sim 4a_0$ periodicity and register to the Cu-O bond directions of the vortex-induced LDOS are likely signatures of strong electronic correlations in the underlying lattice. Such a $4a_0$ periodicity in the electronic structure is a frequent prediction of coupled spin-charge order theories for the cuprates, but has not been previously observed in the quasiparticle spectrum of any HTSC system. This may be the first local glimpse into the structure of the mysterious "pseudogap" phase whose bulk properties are exhibited by all high temperature superconducting materials outside of the superconducting dome.

Chapter 5

Impurities

Since the discovery of high temperature superconductivity in 1986, there has been a great deal of speculation about the nature of the underdoped phase(s). An undoped cuprate is an antiferromagnetic Mott insulator. The physics of a doped Mott insulator, which must connect the antiferromagnetic and superconducting phases, is not well understood theoretically, and few other real manifestations of a doped Mott insulator have been found. Above the superconducting transition temperature T_c, underdoped materials also exhibit a mysterious "pseudogap" phase,[132, 144] where density of states is gapped and electrons may be paired but there is no bulk superconductivity.

One reason these regions of phase space remain so mysterious is that extreme underdoped cuprate crystals have proven very difficult to grow, and have not been available for experimental study. In this chapter I will discuss scanning tunneling microscopy and spectroscopy results from inhomogeneous $Bi_2Sr_2CaCu_2O_{8+\delta}$ (BSCCO) crystals which may give us access to nanometer-sized patches of extreme underdoping. In these regions, we find a notable absence of defect scattering resonances, which may indicate a novel electronic structure. The relationship of the studies in this chapter to the phase diagram of BSCCO is shown in figure 5.1.

Possible explanations for the "disappearance" of defect resonances in underdoped crystal regions include a modified Kondo effect, a loss of particle-hole symmetry, or spin-charge separation or other electron fractionalization. More mundane possibilities include convergence of the hole dopants around the impurities during crystal growth or annealing, or perhaps the impurities themselves suppress the superconducting order parameter and lower the surrounding superconducting gap.

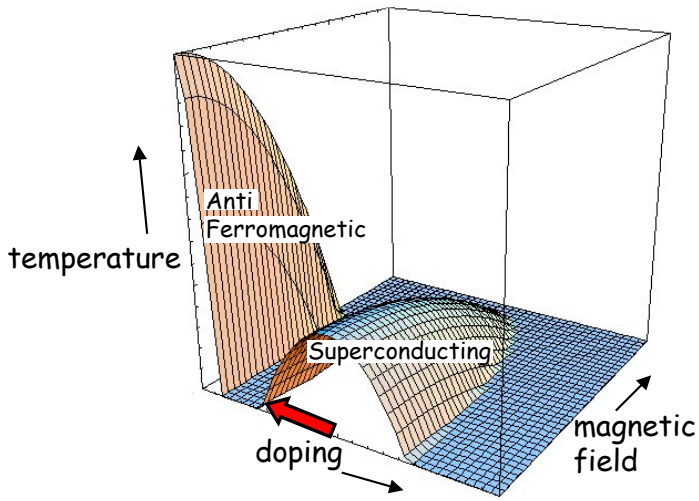

Figure 5.1: A schematic phase diagram of $Bi_2Sr_2CaCu_2O_{8+\delta}$. The red arrow shows the area in phase space covered in this chapter. Samples ranging from optimally doped to underdoped were studied at $T = 4.2$ K and $B = 0$ Tesla.

5.1 Inhomogeneity

Recently there has been much evidence for inhomogeneity in BSCCO.[91, 90, 92, 145] There has been some controversy as to whether the observed inhomogeneity is intrinsic or an artifact of dirty samples or poorly distributed oxygen atoms. Hoogenboom *et al.* claimed to have achieved homogeneity in slightly overdoped BSCCO following a specific annealing procedure, but they have never shown any 2-dimensional DOS maps to prove it. They also admit they have not been able to achieve homogeneity in underdoped BSCCO crystals.[146] Practically speaking, the apparent inevitability of inhomogeneity in underdoped crystals presents an additional challenge for bulk experimental studies: if novel properties are observed in underdoped crystals, one must ask whether they represent a single underdoped phase, or whether they are an artifact of the granularity or inhomogeneity itself. In any case, for our purposes, it matters not at all whether the inhomogeneity is an intrinsic or unavoidable phenomenon. The point is that we do see inhomogeneity in our crystals, and because we have a local probe, we can make use of the inhomogeneity to access different areas of phase space within a single crystal.

A useful way to quantify the inhomogeneity is to make a "gapmap". To do this, we measure a density of states (DOS) spectrum (101 energy points) at every single point in a 128×128 pixel, $\sim 500 \times 500$ Å field of view. From each spectrum, we extract the local gap Δ in the density of states at the Fermi level. (Note that this may or may not be a

superconducting gap; it's possible that in some spatial locations it is actually a pseudogap.)

We have measured these "gapmaps" on more than 10 different samples with nominal bulk doping ranging from $p \sim 0.1$ to $p \sim 0.17$. In all samples, we find segregation of the sample into patches of different local Δ. Each patch is 2-3 nm across. Within a typical sample, the variation in Δ from one patch to another can be as large as 100%. Example gapmaps for two samples of different bulk doping can be seen in figure 5.2.

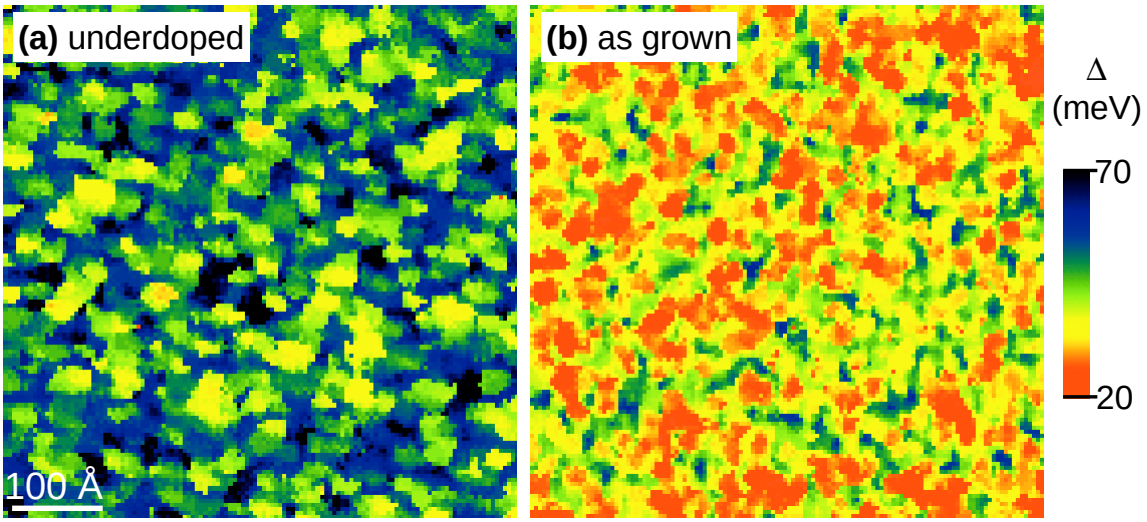

Figure 5.2: Gapmaps for (a) underdoped ($\overline{\Delta} = 50.6$ meV) BSCCO and (b) "as-grown" (slightly overdoped, $\overline{\Delta} = 35.3$ meV) BSCCO with 0.5% Ni substitutions.

Relating $\overline{\Delta}$ to T_c and p

From many different experiments on the cuprates, there are well-documented relationships between the independently controlled bulk doping p and the measured parameters T_c and mean gap of a bulk sample $\overline{\Delta}$. T_c can be related to hole concentration p using the following formula given by Presland *et al.*[147]

$$T_c/T_c^{\max} = 1 - 82.6(x - 0.16)^2 \tag{5.1}$$

This parabolic form seems to be quite general for many of the hole doped cuprates.[148] The relationship is plotted in figure 5.3(a) with $T_c^{\max} = 92$ K for optimally doped BSCCO.

Bulk mean gap $\overline{\Delta}$ can be related to hole concentration p using a compilation of measurements from SIS tunneling and ARPES. A plot from Miyakawa *et al.*[149] compiling results

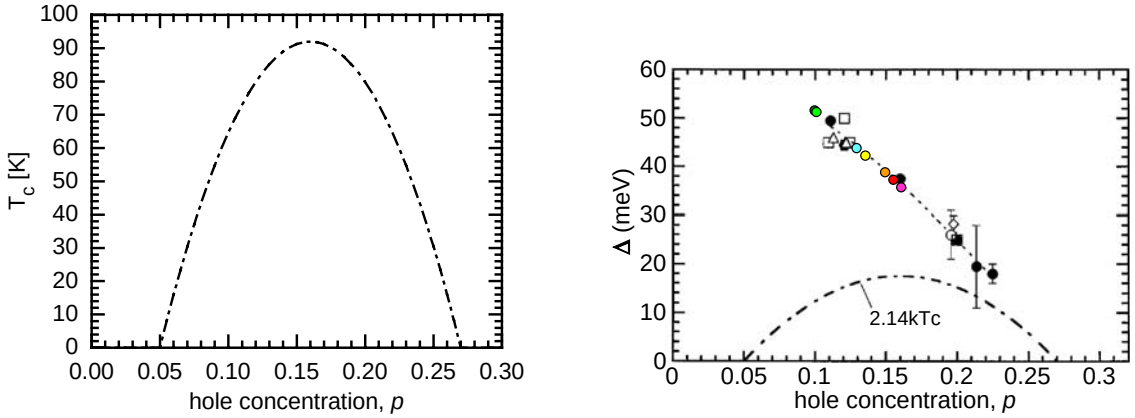

(a) T_c vs. p (b) $\overline{\Delta}$ vs. p

Figure 5.3: (a) Presland formula for critical temperature T_c vs. doping p. (b) Miyakawa plot of gap $\overline{\Delta}$ vs. doping p. Filled black circles are SIS tunneling results measured by Miyakawa *et al.*[149]; open circles and open diamonds are other SIS tunneling results; and open triangles and open squares are ARPES results. Colored circles show the measured bulk $\overline{\Delta}$ for seven different samples we have looked at. We cannot measure p directly, so I have just used our measured $\overline{\Delta}$ to place our samples onto the Miyakawa trend line.

from several experiments is reproduced here in figure 5.3(b). (Some other relevant results relating $\overline{\Delta}$ to p have been presented by Nakano *et al.*[150] and Ozyuzer *et al.*[145]) The Miyakawa plot shows a clear trend: as bulk doping p decreases, bulk $\overline{\Delta}$ increases. The best fit to the data shown by Miyakawa *et al.* gives the relationship:

$$\overline{\Delta} = 79.58 - 273.85p \tag{5.2}$$

I also plot in figure 5.3(b) colored circles representing seven of the crystals we have studied. Note that we measure $\overline{\Delta}$ but we cannot measure p directly. I have just plotted our points on top of the Miyakawa trend, with the assumption that our samples follow the same trend, so that bulk p can be estimated from the measured $\overline{\Delta}$. A summary these seven crystals is given in table 5.1.

It seems reasonable to suppose that the Miyakawa trend also holds locally in the crystal. If this is true, then a nanoscale region with low local Δ may have a high local hole concentration. Conversely, a nanoscale region with high local Δ will give us a window into the very underdoped region of the BSCCO phase diagram. As can be seen in the Miyakawa plot, the most underdoped samples available to all six different research groups who contributed data to this plot have $p \sim 0.1$ with $\overline{\Delta} \sim 50$ meV. However, in our "gapmap"

$\overline{\Delta}$ [meV] (measured, STM)	p (Miyakawa plot)	T_c (Presland formula)	T_c (measured, Eisaki)
35.3	0.163	92K	83K (0.5% Ni)
36.8	0.157	92K	85K (over)
38.9	0.150	91K	85K (0.2% Ni)
41.4	0.140	89K	84K (0.6% Zn)
43.7	0.132	86K	85K (0.2% Ni)
50.6	0.107	71K	79K (under)
50.9	0.106	70K	75K (under)

Table 5.1: Summary of measured $\overline{\Delta}$ and T_c, and calculated p and T_c for seven different crystals studied. All crystals are grown by Eisaki and Uchida, using the floating zone method. There is some disagreement between the calculated and measured T_c shown in this table. Some likely explanations for this disagreement include: (1) It is known that T_c is depressed by approximately 5 K per atomic percent by the presence of Zn or Ni impurities.[151] Therefore, the measured T_c for the Zn and Ni substituted crystals should be lower than the T_c calculated from doping p alone. (2) The T_c measurement was made by the crystal growers long before the crystals were inserted into the STM. It is possible that oxygen content changed during the long shelf time of up to several months. (3) The inhomogeneity may influence the relationship between p and T_c. If a connected path of high-T_c patches exists, then the measured bulk T_c may be higher than the average of the local T_c's from each patch.

studies, we see nanoscale patches with local gap Δ in excess of 70 meV. This indicates that with the spatial resolution of an STM we may be able to access properties of the material in a far-underdoped region of phase space inaccessible to bulk studies.

5.2 Types of Impurities

What can we learn about a new region of phase space if we have access only to a nanometer-sized patch of it? One way to probe a small region of material is to stick an impurity in, and see how the surrounding electronic structure responds. We cannot intentionally stick impurities into specific regions of the sample. But BSCCO crystals can be intentionally grown with known concentrations of impurities, so we can study the patches they happen to land in.

I will discuss three different types of impurities, all of which are centered at the Cu lattice site: intentionally substituted Zn, intentionally substituted Ni, and a native defect which

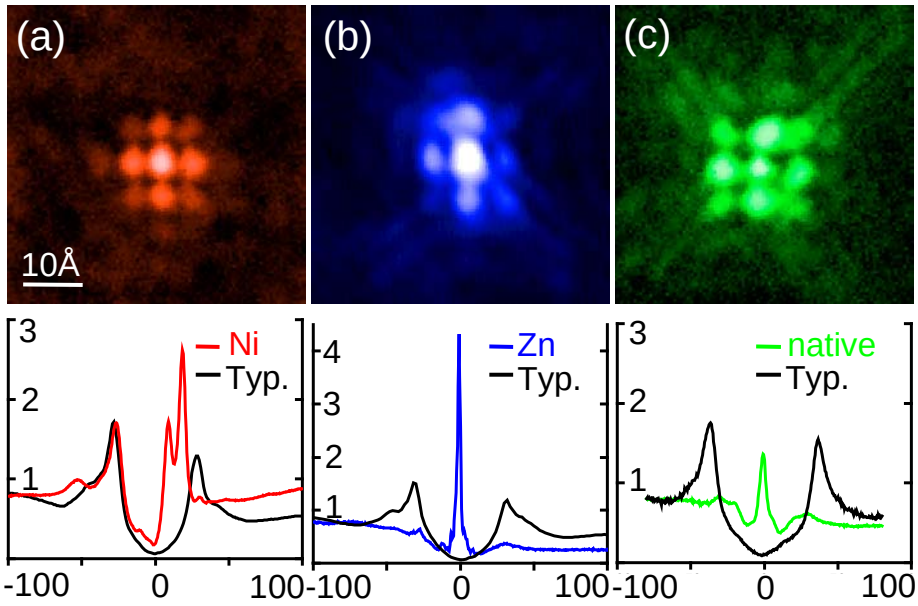

Figure 5.4: Density of states maps and spectra at (a) Ni, (b) Zn, and (c) native defect resonances in BSCCO. All maps are 50 Å square. A spectrum on the center atom of a Ni impurity shows peaks at +9 meV and +18 meV; a spectrum at a Zn impurity shows a peak at -1.5 meV; and a spectrum at a native defect shows a peak close to 0 meV. Black curves show typical spectra far from the impurities, for comparison. Each map was measured near the peak energy of the corresponding resonance: (a) +9 meV; (b) -1.5 meV; and (c) -0.5 meV.

has a strong zero bias conductance peak (ZBCP). The origin of the native defect is not known for sure, but based on a combination of topographic and spectroscopic information it seems likely that it is a missing Cu atom, or a missing apical oxygen atom from directly above the Cu atom.[152] The spatial and spectroscopic signatures of these three types of impurities are shown in figure 5.4.

I will report in detail on three samples:

1. nominal 0.6% Zn substitution (actual observed $\sim$ 0.13%);
   "as-grown" $T_c = 84$ K

2. nominal 0.2% Ni substitution (actual observed $\sim$ 0.21%);
   also contains $\sim$ 0.14% native defects with ZBCPs;
   "as-grown" $T_c = 85$ K

3. nominally "clean", but ∼ 0.13% native defects with 4-fold symmetric ZBCPs; overdoped $T_c = 85$ K

If these impurities are randomly distributed throughout the crystal, then they will land in many different patches of different Δ. By measuring the properties of the electronic perturbations caused by these impurities as a function of their local environment Δ, we may be able to probe patches of the very far underdoped region of the crystal. The punch-line to this story is that the impurities apparently *do not even show up* in the very large Δ (or very underdoped) regions of the crystal!

5.3 Defect Properties vs. Local Δ

To catalog the properties of large numbers of defects versus their surrounding local gap, automatic algorithms are needed for (1) identifying defects; and (2) computing the local gap Δ.

5.3.1 Identifying Defects

Each type of defect produces a resonance in the density of states at a characteristic energy. One correlation to look for is dependence of the strength of this resonance on local gap Δ. Since it's possible that the resonance will be significantly weaker in some local environments than others, we need a clear-cut algorithm for distinguishing between a weak impurity and a noise spike.

It's easier to make the distinction between real defects and noise when the data has higher energy resolution and higher spatial resolution. Due to limitations in the helium hold time of the fridge, most of our datasets have only 4 Å spatial resolution and 2 meV energy resolution. (A summary of the available data resolution is shown in table 5.2.) The identification of real impurities in low spatial resolution data can be somewhat ambiguous.

Zn impurities

Zn impurities have a peak in the density of states at -1.5 meV. This peak is strongest on the central atom, and falls off to about 1/5 of the value on the next nearest neighboring atoms.[153] In order to look for Zn resonances, I plot in figure 5.6 the strength of all local maxima in the 0 meV density of states map. Of course this includes all of the local maxima

nominal impurities	spatial resolution	energy resolution
0.6% Zn	4.1 Å	2 meV
0.2% Ni	4.7 Å	2 meV
none	1.3 Å	2 meV

Table 5.2: Spatial and energy resolution available for the three samples studied in this chapter.

in the background noise too. By examination of this plot, I impose a sensible cutoff at 0.2 nS zero bias conductance. From this cutoff, I find 25 Zn impurities in a 530 × 530 Å field of view, resulting in an actual concentration of 0.13% Zn substitution.

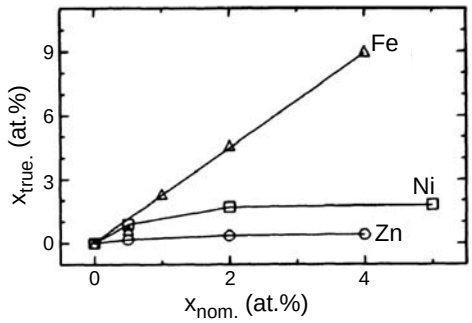

Figure 5.5: True vs. nominal impurity concentration.[151] Despite the introduction of a large number of impurities into the melt while the crystal is growing, some impurities do not incorporate well into the crystal, but are rather swept along by the melt. Therefore the true impurity concentration, measured by independent means after crystal growth, may be much less than the nominal impurity concentration, which is the % of impurities in the melt. This figure is borrowed from vom Hedt *et al.*[151]

The nominal Zn substitution was 0.6%, a factor of almost 5 higher than that observed. There are two possibilities for this discrepancy. One possibility is that the crystal actually contains fewer Zn atoms than the crystal growers thought. The crystal was grown by the floating zone method, so it is possible that most of the Zn impurity atoms introduced in the Cu mix are simply swept along instead of incorporating into the crystal. In fact, vom Hedt *et al.*[151] grew Zn-substituted BSCCO crystals by a similar method, and reported that the Zn concentration incorporated into the crystal saturated at 0.4% even as the starting Zn concentration in the melt was increased to 4%. The true impurity concentration (as measured by x-ray wavelength-dispersive microprobe analysis) is shown vs. nominal concentration in figure 5.5. According to the vom Hedt plot, our measured Zn concentration of 0.13% is very close to what we should expect for a nominal Zn concentration of 0.6%.

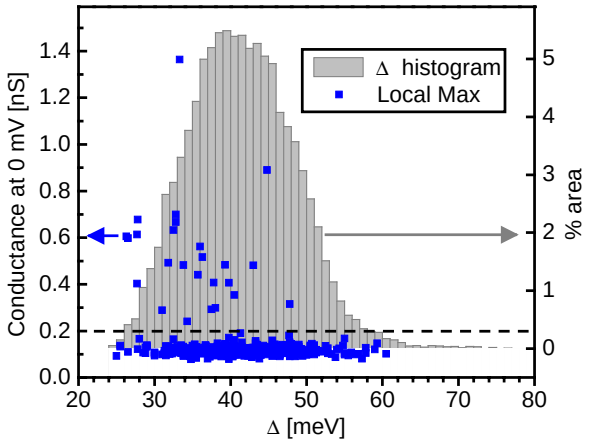

Figure 5.6: Strength of all local maxima in the 0 meV dI/dV map vs. local gap Δ, in nominal 0.6% Zn-substituted BSCCO. Over 500 local maxima are shown here as blue squares, but clearly the vast majority are just local maxima in the background noise. A sensible cutoff of 0.2 nS is imposed to separate true resonances from local noise maxima. A histogram of the gapmap values is plotted in the background in grey for comparison.

Another possibility is that more Zn impurities are present but for some reason we cannot see all of them, perhaps due to differences in their local environment which render them invisible to our STM technique. This may be true, but as we shall see, it would only account for ∼18% missing zinc atoms, not the ∼80% discrepancy we see. The most likely explanation for the bulk of the discrepancy is that the number of Zn atoms actually incorporated is significantly less than the number of Zn atoms introduced in the melt, and the "nominal" impurity concentration is simply not a reliable quantity.

Ni impurities

Ni impurities are more complicated (because they have spin 1, as opposed to Zn which has spin 0, so Ni resonance peaks are split in two). They have peaks in the density of states at +9 meV and +18 meV on the central atom, but they also have peaks in the density of states at -9 meV and -18 meV close to the nearest neighbor atoms.[154] The central atom peak is the strongest, so we look for Ni atoms in the positive density of states maps. We find Ni atoms by their +18 meV resonance (instead of their +9 meV resonance) for two reasons. First, since our sample has only 2 meV energy resolution, we would need to look for the +9 meV peak in the +8 meV or +10 meV maps, where it will not be at full strength. Second, this sample also contains a high concentration of native impurities, which have strong density of states peaks near zero bias. The tails of these strong peaks are still visible

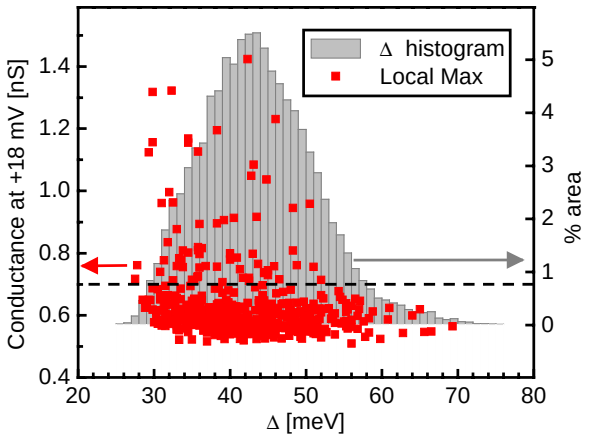

Figure 5.7: Strength of all local maxima in the +18 meV dI/dV map vs. local gap Δ, in nominal 0.2% Ni-substituted BSCCO. Over 500 local maxima are shown here as red squares, but a sensible cutoff of 0.7 nS is imposed to separate true resonances from local noise maxima. A histogram of the gapmap values is plotted in the background in grey.

as far away from zero bias as 10 meV, which makes it difficult to distinguish between Ni impurities and native impurities by looking at a +10 meV map.

The strength of all local maxima in the +18 meV map is plotted in figure 5.7. Here it is somewhat less clear where to impose a cutoff than in the Zn case. We impose a low cutoff at 0.7 nS conductance, and risk including some noise amongst our Ni resonances, rather than omit any real Ni resonances. This cutoff leads to 53 Ni resonances in the field of view. In fact, we are almost certainly including some noise, since the nominal Ni concentration is 0.2% but the observed Ni concentration is 0.21%. It's more likely that the true concentration is somewhat less than the nominal concentration, as shown in figure 5.5.

Native Defects

Unintentional native defects appear in most samples, and are similar to Zn impurities in that they have a strong peak in the density of states near zero bias. The local maxima of zero bias maps for two samples are shown in figure 5.8. Based on these plots, thresholds are imposed at 0.4 nS and 0.2 nS. The values are slightly different, most likely because the lock-in amplifier phase was set incorrectly in the 0.2% Ni-substituted map. An incorrect phase merely results in a constant offset in the conductance measurement. Indeed, the green value plots in figures 5.8(a) and 5.8(b) are very similar, just shifted by 0.2 nS vertically.

The spatial pattern of the native defects is somewhat different from the Zn spatial

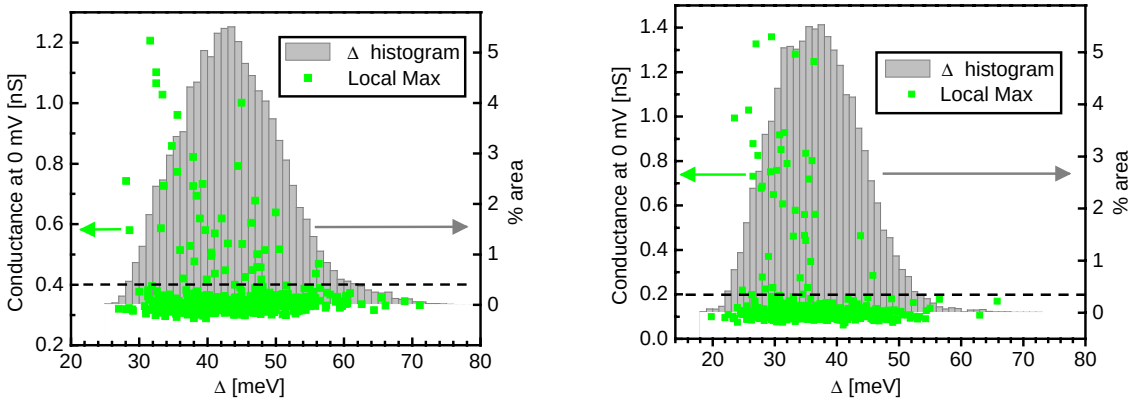

(a) nominally 0.2% Ni substitutions

(b) nominally no substitutions

Figure 5.8: Strength of all local maxima in the 0 meV dI/dV map vs. local gap Δ, in (a) nominal 0.2% Ni-substituted BSCCO, and (b) nominally clean BSCCO with no intentional impurities. Over 500 local maxima are shown here as green squares, but sensible cutoffs of (a) 0.4 nS and (b) 0.2 nS are imposed to separate true resonances from local noise maxima. Histograms of the gapmap values for the two samples are plotted in the background in grey.

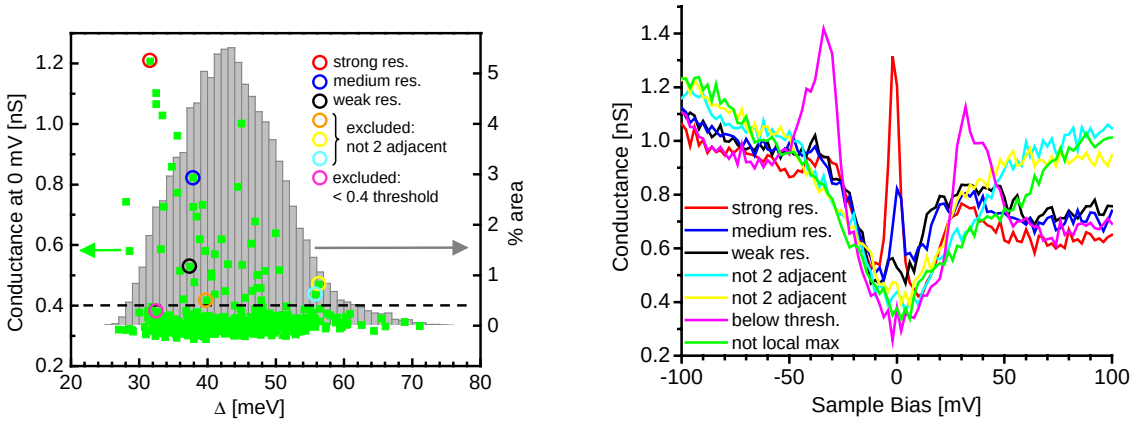

(a) local max

(b) sample curves

Figure 5.9: Sample curves from potential native defect sites. In order to find the native defects, we impose two constraints: zero bias conductance must exceed a certain threshold, and the spatial signature must include two adjacent pixels with high zero bias conductance. (a) circles several definite zero bias defects and several borderline "local maxima", while (b) shows sample spectra from the chosen circles examples in (a). We can see that the automatic criteria were good; only red, blue, and black deserved to be called zero bias conductance peaks, and only these three spectra passed the automatic criteria.

pattern. Unlike Zn and Ni, the native defect resonance has more strength on neighboring atoms than it does on the central atom. Therefore we impose an additional constraint when looking for native impurities in the low spatial resolution dataset in figure 5.8(a). They must have two adjacent pixels with a high zero bias conductance. In figure 5.9(a), the three local maxima eliminated by this additional constraint are circled in yellow, cyan, and orange. In figure 5.9(b) spectra from these and several other local maxima are shown for comparison. It is apparent from these spectra that there is really no zero bias conductance peak in the eliminated local maxima.

The other dataset, in figure 5.8(b) has high spatial resolution, so we impose the additional constraint that observed ZBCPs must exhibit clear 4-fold symmetry in the zero bias conductance map. This eliminates 4 of the 34 local maxima which exceeded the cutoff of 0.2 nS. (All 4 eliminated had local $\Delta < 35$ meV.)

5.3.2 Local Gap Determination

The local gap needs to be determined at a large number of pixels, so it is impractical to look at every single spectra individually and determine the gap by eye. The spectra are also somewhat noisy, so the determination of gap by eye might in some cases be somewhat subjective. This might lead to a false correlation between impurity characteristics and local gap, if the by-eye-gap-determiner really *wants* the local gap to take a certain value in order to support an attractive hypothesis.

So it is safer to let a computer algorithm do the gap determination. Of course any program is written by a human and may still be subject to systematic errors in gap determination, but at least any such errors will be systematic and objective. The computer algorithm to find the gap is summarized in appendix A. In summary, the algorithm looks for positive and negative gap-edge peaks, then returns the average, $\Delta = (\Delta_+ + \Delta_-)/2$.

Local gap around an impurity

It is important to choose a consistent method to measure the local gap around an impurity. In some cases, the impurity destroys the coherence peaks on site, so it is difficult to determine the local gap. It makes more sense to look for the gap in neighboring pixels. But how far away should we look? We could try 4 nearest neighboring pixels, 8 nearest plus next nearest neighboring pixels, 12, 20, etc. The more pixels we average over, the more likely we are to be sampling an adjacent nanoscale region with totally different local Δ. Averaging over multiple pixels will have the effect of narrowing all gap distributions and

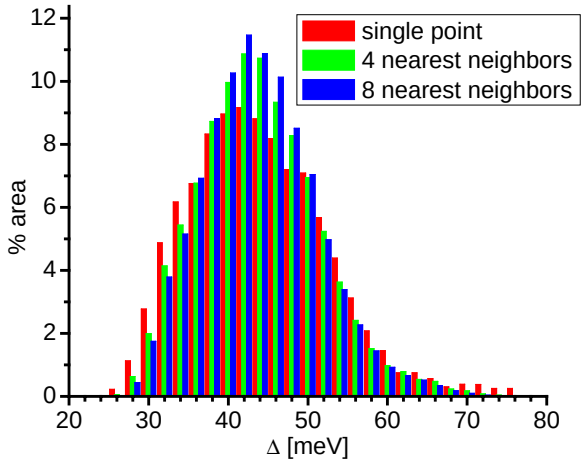

Figure 5.10: Comparison of gap histograms for different averaging schemes. Red shows the true single-pixel gap histogram, which has the largest spread. Green shows a histogram of the average of 4 nearest-neighboring pixels around each central pixel. Blue shows the average of 8 nearest-neighboring pixels; blue has all but lost the tails of the distribution.

eliminating the tails of the distributions. For example, figure 5.10 shows the histogram of local gap in a single field of view for three different averaging schemes: (red) single pixel distribution; (green) average of 4 nearest neighbors around each pixel; (blue) average of 8 nearest neighbors around each pixel. Note that the red distribution is broadest and has the longest tails, while the blue distribution has lost significant weight in the tails.

In order to define the local gap around each pixel without inadvertently including pixels from neighboring different-gapped regions, we define the local gap at a given pixel as the average of the gap measured at its four nearest neighbor pixels.

5.3.3 Distribution of Impurities

Now that we have an objective algorithm to (a) locate impurities and (b) determine the local gap Δ around the impurities, we can plot their distributions. Histograms of total gap distributions and impurity local gap distributions are shown in figure 5.11. The locations of the impurities are superimposed on the gapmaps in figure 5.12. It is striking that no defect resonances of any type appear in large gap regions any of these three samples.

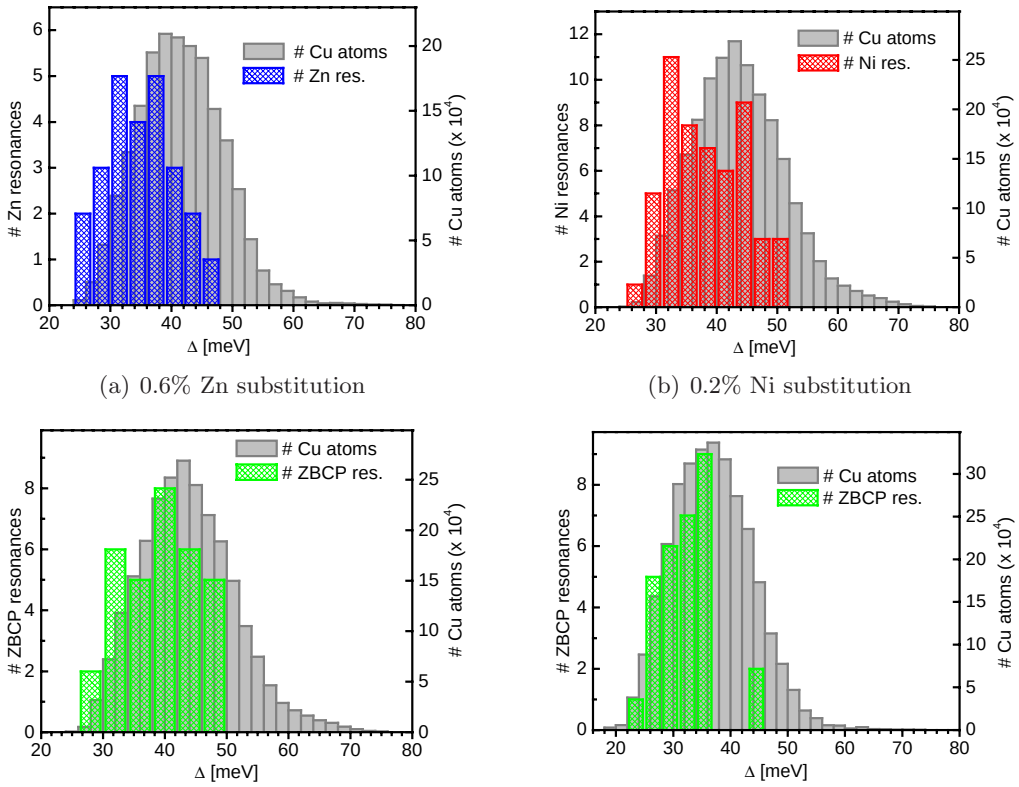

(a) 0.6% Zn substitution

(b) 0.2% Ni substitution

(c) 0.2% Ni substitution

(d) no intentional substitution

Figure 5.11: Gap and defect histograms. Histograms of Δ from three spectral-surveys are shown in gray. Histograms of local Δ at the impurity sites are shown in blue (Zn substitution), red (Ni substitution), and green (native defect). For each impurity resonance, the local gap is determined by the spatial average of Δ from the four nearest neighbor pixels, effectively 4 points approximately 4-5 Å away on all 4 sides. Although for $\Delta < 35$ meV the total Δ distributions and impurity site Δ distributions are similar in shape, above $\Delta \sim 35$ meV they rapidly diverge and the impurity resonance distributions reach zero by 50 meV. Remarkably, no defect scattering-resonances are observed in any region where $\Delta > 50 \pm 2$ meV.

Are these distributions a statistical accident?

With a small number of defects, statistical fluctuations might result in the absence of defects in regions where $\Delta > 50$ meV. However, if the defects are distributed randomly, and if all regions can support quasiparticle scattering resonances, our non-observation (in three independent experiments on three different crystals) of defect resonances in regions with $\Delta > \Delta_{\text{cutoff}}$ (where $\Delta_{\text{cutoff}} \sim 50$ meV) has a very low combined probability.

For each sample and impurity type, the probability of such a low-Δ distribution of

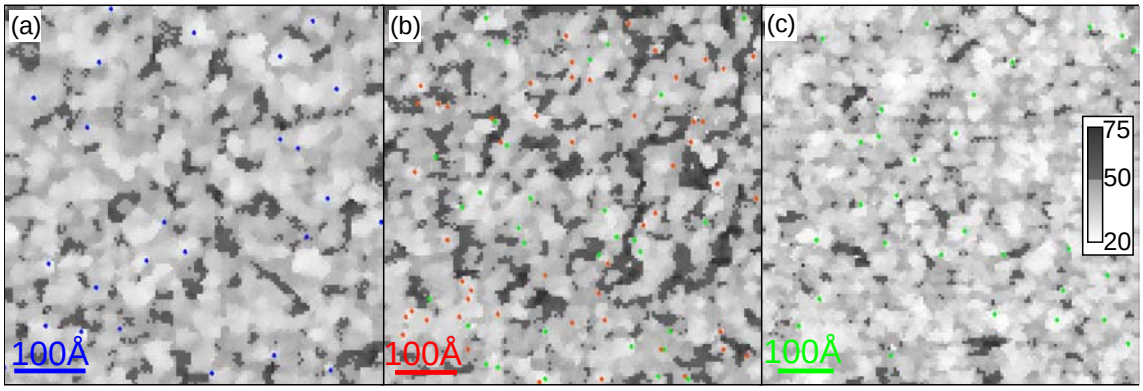

Figure 5.12: Location of defect resonances with respect to gapmap. Spectral surveys of 101 energies × 128 × 128 pixels were acquired at 4.2K on three BSCCO samples, all with tunnel junction resistance of 1GΩ. The gapmap calculated from each spectral survey is shown with a color scale such that regions with $\Delta < 50$ meV are light gray and regions with $\Delta > 50$ meV are dark gray. The locations of defect resonances are superimposed on the gapmaps in blue (Zn substitutions), red (Ni substitutions), and green (native defects). No defect resonances of any type were detected in dark gray regions where $\Delta > 50 \pm 2.5$ meV in any of the three samples.

visible resonances is:

$$p(\Delta_{\rm imp} < \Delta_{\rm cutoff} \ \ \forall \ \ \text{impurities}) = (\%\ \text{area with}\ \Delta < \Delta_{\rm cutoff})^{(\#\ \text{impurities observed})} \qquad (5.3)$$

Combining the probabilities from our 3 samples results in a total probability of:

$$p_{\rm total} = (0.824)^{25} \times (0.867)^{53} \times (0.804)^{32} \times (0.904)^{30} = 2 \times 10^{-10}, \qquad (5.4)$$

very low indeed. However, in our excessive care to include all visible impurity resonances, we may have inadvertently included some noise spikes. Reducing the exponents in equation 5.4 will increase $p_{\rm total}$. So let us go back to figures 5.6, 5.7, and 5.8 and impose a more stringent conductance cutoff, just to see how much it might increase our chances of accidental occurrence of this low-Δ distribution. In the Zn-doped sample, the cutoff was very clear; it does not need to be changed. In the "clean" sample, each defect was simultaneously identified by its spatial pattern in a high-spatial resolution map, so the cutoff does not need to be changed. However, in the Ni-doped sample we can choose a more conservative cutoff of 0.85 nS for identification of Ni impurities, and a cutoff of 0.6 nS for identification of native defects. This results in a new total of 22 Ni impurities and 20 native defects. The

sample	defect	# observed	Δ_{cutoff} (highest Δ at observed defect site)	% area with $\Delta < \Delta_{\text{cutoff}}$	probability of accidental occurrence
0.6% Zn	Zn	25	47.8 meV	82.4%	0.007910
0.2% Ni	Ni	53	52.0 meV	86.7%	0.000519
0.2% Ni	native	32	49.8 meV	80.4%	0.000929
"clean"	native	30	45.8 meV	90.4%	0.032339

Table 5.3: Defect resonance gap distributions and their probability of occurrence.

new probability of these distributions occurring by chance is:

$$p_{\text{total}} = (0.824)^{25} \times (0.839)^{22} \times (0.804)^{20} \times (0.904)^{30} = 1 \times 10^{-7} \tag{5.5}$$

Therefore, with either a liberal or conservative criterion for locating defects, chance occurrence of this low-Δ distribution appears ruled out.

Are dopants attracted to defect regions during crystal growth?

One scenario which might explain our observations is that defects somehow seed nanoscale regions, influencing them to develop into superconducting domains with $\Delta < 50$ meV. Perhaps oxygen dopant atoms are attracted to the vicinity of defect sites, either during crystal growth, subsequent annealing, or mobility at room temperature during crystal storage. Even if the oxygen atoms do not move at all, it is possible that the doped holes in the CuO plane congregate near defects. These pockets of oxygen and their concomitant holes would locally depress Δ and would thus explain our observed correlation between visible defects and low-Δ regions.

This scenario seems unlikely, because visible resonances at both Ni and Zn (and possibly vacancy) sites would have to attract holes. The Cu atoms in the crystal are believed to have valance $3d^9$ and charge +2. The Ni substitutions are believed to have valance $3d^8$ and charge +2. Zn substitutions are believed to have valance $3d^{10}$ and charge +2. So there is no compelling reason why both Ni and Zn substitutions would attract oxygen atoms or holes. In fact, since they are on opposite sides of Cu in the periodic table, one might expect that if Ni attracts oxygen or holes, then Zn would repel oxygen or holes, or vice versa. Some relevant properties of Ni, Cu, and Zn are shown in table 5.4. From this it can be seen that almost all chemical properties of Cu are intermediate between the properties of Ni and Zn,

so it is likely that Ni and Zn would have opposite chemical behavior with respect to Cu.

element	ionization energy (eV)			electronegativity (Pauling scale: 0-4)	covalent radius (Å)
	1st	2nd	3rd		
Ni	7.635	18.15	35.16	1.91	1.15
Cu	7.726	20.29	36.83	1.9	1.17
Zn	9.394	17.96	39.7	1.65	1.25

Table 5.4: Some chemical properties of Ni, Cu, and Zn which might affect their tendency to attract oxygen atoms or holes in a cuprate superconductor. For all properties listed, Cu has values intermediate between those of Ni and Zn.

In summary, attraction of dopants to Zn substitutions, Ni substitutions, and native defects is a possible scenario we cannot rule out. However, it seems unlikely because Zn and Ni sandwich Cu in the periodic table, and thus might be expected to display opposite chemical behavior, not the same behavior.

Does the impurity lower the gap in the surrounding region?

Defects of any type may suppress superconductivity and thus lower the superconducting order parameter and local gap Δ (without actually affecting local dopant concentration). One might expect that Zn (which has spin 0 and is non-magnetic) would have a more disruptive effect than Ni (which has spin 1 and is magnetic) when substituting for the magnetic spin-1/2 Cu atom. There is some conflicting literature in this regard.

Vom Hedt *et al.* report that Zn and Ni (and in fact Co and Fe too) substitutional impurities in BSCCO have exactly the same effect on T_c, which might imply that no one element is more disruptive to local superconductivity than the other. All four substitutional impurities suppress T_c with an initial slope (at low concentrations) of -5 K / atomic %, as shown in figure 5.13(a), copied from vom Hedt *et al.*[151] This slope holds up to 2% for Ni and Fe, but it has not been measured beyond 0.4% for Zn, because of difficulties in sample growth. Although the three closely spaced data points measured for Zn substitution in BSCCO may be insufficient to establish a reliable trend, the effect of Ni substitution on T_c in BSCCO has been verified by Hancotte *et al.*[155]

However, a later study by Westerholt *et al.* showed that Zn causes a much larger T_c suppression than Ni or Fe when substituted in YBCO. In YBCO it is apparently easier to achieve high Zn concentration, and the T_c drop is 15 K / atomic % Zn, compared to approximately 2 K / atomic % Ni, as shown in figure 5.13(b). Other non-magnetic elements

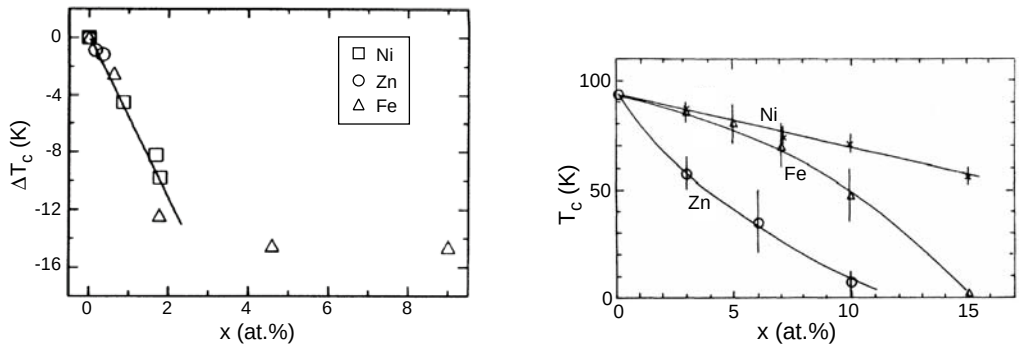

(a) $Bi_2Sr_2CaCu_2O_{8+\delta}$ (b) $YBa_2Cu_3O_{7-\delta}$

Figure 5.13: Bulk T_c suppression by substitution of Ni, Zn, or Fe impurities in BSCCO[151] or YBCO[156]

such as Al and Mo also cause large T_c suppression, while other magnetic elements such as Fe have a weaker effect.[156]

Furthermore, S-I-S tunneling experiments, both STM and break junction, on Ni and Zn substituted crystals have shown that Zn concentration up to 1% has little effect on gap $\overline{\Delta}$ (if anything, $\overline{\Delta}$ decreases slightly). On the contrary, Ni substitution up to 2% increases $\overline{\Delta}$ by up to a factor of 2.[155] However, a theoretical study of Ni atoms in BSCCO requires that Ni atoms locally suppress Δ by 6 meV in order to achieve a good fit to the data.[157]

Microscopic studies show that Zn atoms locally destroy the superconducting coherence peaks.[153] Substitution of Ni at a Cu site has a much weaker effect on the local electronic structure of superconductivity. Ni atoms retain particle-hole symmetry in the electronic structure (a hallmark of superconductivity), when integrated over area. This is in stark contrast to Zn atoms which display a single resonance at -1.5 meV. Furthermore, the superconducting coherence peak is still strong at the Ni site and neighboring sites, in contrast to the coherence peaks which are destroyed surrounding the Zn site.[154]

Therefore, while it might be reasonable to guess that Zn significantly depresses the superconducting gap, we would expect that suppression of the gap by a Ni impurity would be substantially less pronounced. However, both Zn and Ni display similar local Δ distributions, as shown in table 5.5. Furthermore, impurity atoms are clearly not necessary to create patches of low Δ, since these low-Δ regions exist even in samples with no visible defects.

defect	$\overline{\Delta}_{\text{total}}$ (meV)	$\overline{\Delta}_{\text{defect}}$ (meV)	abs. difference	% difference
Zn	41.4 ± 7.8	35.9 ± 5.7	5.5	13.3%
Ni	43.6 ± 8.7	38.7 ± 6.4	4.9	11.2%
native	36.8 ± 8.2	32.1 ± 4.8	4.7	12.8%

Table 5.5: Mean gap overall for three samples, and mean gap surrounding just the defects in these samples.

Does the impurity intensity decrease with increasing local gap?

It is important to distinguish whether the defect resonances are actually absent in high-Δ regions, or merely too weak to detect in the presence of noise. If the defect resonances are decreasing in strength as a function of increasing local Δ then we would expect that at some Δ_{cutoff} the resonances would drop below the noise level and we would no longer be able to detect them. However, we can see from figures 5.6, 5.7, and 5.8, that the strength of the impurity resonance does not appear to be dependent on local Δ. Furthermore, the impurity with largest detected Δ is not necessarily close to the noise level.

Are the impurities present but not visible in the high-gap regions?

The final, and most interesting, hypothesis is that Zn, Ni, and native defects are physically present in regions with $\Delta > 50$ meV, but that they do not create scattering resonances because these regions represent an electronically distinct phase. If defects are randomly distributed, and if the locations of defect resonances indicate the local existence of superconductivity, then the distribution of superconducting regions has a similar shape to the colored histograms shown in figure 5.11. The picture would then be of superconducting regions when $\Delta < 50$ meV, and an unidentified second phase (possibly the pseudogap phase) when $\Delta > 50$ meV. Data concerning typical shapes of the DOS spectra corroborates this picture[92] particularly because the energy where regions of low-Δ and sharp coherence peaks disappear is identical to the energy where the defect resonances disappear.[92] Overall, these measurements suggest BSCCO is inhomogeneous, possibly with superconducting regions embedded in an electronically distinct underdoped background.

Additional evidence: native defect concentration vs. doping

One experiment to distinguish between this chemical explanation for the correlation between visible defect resonances and low-Δ regions, and the explanation that defects are

present everywhere but for some reason *invisible* in the high-Δ regions is the following: Grow a single sample with a uniform concentration of Ni or Zn substitutions. Then split the sample into several pieces and anneal each piece in different oxygen environments to change the bulk doping of the crystal. The oxygen annealing temperatures ($\sim 500°$C) are much lower than the crystal growth temperatures ($\sim 800 - 900°$C), so the Ni or Zn impurities would be unable to move, while the oxygens would be mobile. Then perform STM mapping on all the samples. If the dopants merely congregate around the defects, then we should see the same number of defects in all crystals. But if the location of the dopants is uncorrelated to that of the defects, and defects are *invisible* in regions of high Δ, then we should see more Ni or Zn defect resonances in the overdoped crystals, and fewer in the underdoped crystals, despite the fact that all crystals were grown from the same melt and therefore actually contain the same number of defects.

We have not had the opportunity to perform this experiment, because we have not had access to such an intentionally specifically grown set of crystals. However, we have mapped "clean" samples at three different dopings. Each of these three crystals contains some of the same native defects discussed above, identifiable by a sharp zero bias conductance peak, and a characteristic four-fold symmetric spatial pattern. However, as the doping decreases, so does the number of these visible defects.

From topographic information, which shows an indentation at the defect site, we believe that these defects are some kind of missing atom, perhaps missing Cu or missing apical O. If these defects are really missing Cu atoms, we should expect that their numbers would be the same for all three crystals, since the crystals are grown first, and doped second, at a temperature too low for Cu atoms to be mobile. If the defects are missing apical oxygen atoms, we might expect that the number of defects would *increase* as we underdope and reduce the total number of oxygen atoms in the crystal. However, we see the number of defects *decrease* as we underdope.

Zero bias conductance maps and their accompanying gapmaps are shown for three samples in figure 5.14. The locations of four-fold symmetric defect resonances with ZBCPs are shown as red dots superimposed on the gapmaps.

However, there are some additional ZBCPs observed without 4-fold symmetry. Their resonances are not as strong as the 4-fold symmetric ZBCPs, and they do not have any characteristic spatial structure. It is possible that they are a different manifestation of the same underlying defect as the 4-fold symmetric ZBCPs, but lacking the d-wave symmetry of the strongly superconducting nanoscale patches. These weak ZBCPs without 4-fold symmetry will require further investigation.

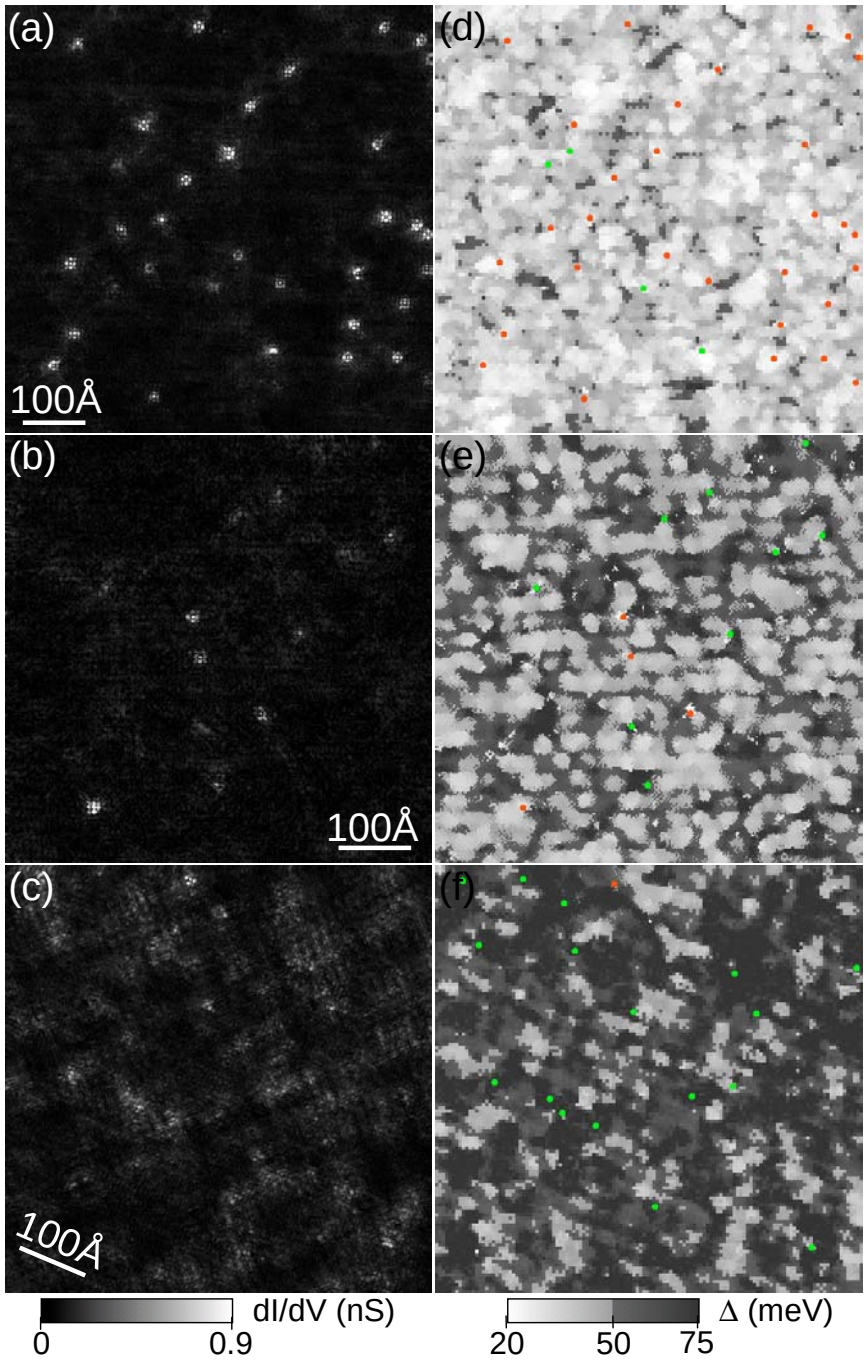

Figure 5.14: Location of defect resonances with respect to gapmap in three "clean" samples of different doping: (a) $p \sim 0.16$; (b) $p \sim 0.11$; and (c) $p \sim 0.08$. In (d)-(f), impurity locations are superimposed on gapmaps with a colorscale cutoff of ∼50 meV. Red dots represent full four-fold symmetric defects, while green dots represent weaker zero bias conductance peaks which display no four-fold symmetry. All red dots are seen in low-Δ (lightly colored) regions of the gapmaps.

sample	$\overline{\Delta}$ (meV)	% area with $\Delta < 50$ meV	4-fold symmetric ZBCPs #	4-fold symmetric ZBCPs total conc.	4-fold symmetric ZBCPs conc. in low-Δ	total ZBCPs #	total ZBCPs total conc.
85K over	36.8	94.9%	30	0.098%	0.103%	34	0.111%
75K under	50.9	53.4%	4	0.017%	0.034%	13	0.056%
65K under	62.5*	20.8%	1	0.004%	0.020%	18	0.076%

Table 5.6: Native defect resonance gap distributions and their probability of occurrence. *This value of $\overline{\Delta}$ is not reliable; the gapmap algorithm does not know how to deal with values of local $\Delta > 75$ meV, so in this very high-Δ sample, a large number of pixels were simply binned into the 75 meV bin for lack of a better plan. Thus the value 62.5 meV is likely too low.

One can see from table 5.6 that the concentration of 4-fold symmetric ZBCPs decreases with decreasing fraction of low-Δ area in the sample. However, the sixth column shows that even the observed concentration within the low-Δ area alone is decreasing with decreasing doping. This comparison between three samples of different dopings suffers from two problems: (1) small number statistics, and (2) the unintentional nature of the impurities which prevents a more complete knowledge of their source. Although we may tentatively suppose that the decreasing number of visible 4-fold symmetric ZBCPs with decreasing doping supports the hypothesis that they only appear in low-Δ regions although they are present everywhere, we must reserve definitive judgement until a more carefully planned study with known impurities can be carried out.

5.4 Possible Theoretical Explanations

The exciting conclusion is that we can locally access patches of underdoped phase, at a doping so low that it is inaccessible to bulk studies. Numerous theoretical predictions exist for this phase, so we can for the first time begin to make comparison between theory and experiment. Some of the theories of underdoped cuprates which specifically address the nature of impurity resonances in a non-superconducting phase are summarized here.

Sachdev

Polkovnikov *et al.* explains that a non-magnetic Zn impurity in BSCCO displays a modified Kondo effect.[158] The spinless Zn replaces a spin-1/2 Cu atom, but causes a spin-1/2

moment to be distributed among the four nearest neighbor Cu atoms. NMR observations show that there is no Kondo screening of the moment at low doping.

However, Sachdev states that there is an onset of non-zero Kondo temperature T_K at a critical doping beyond which the T_K rises rapidly. Near optimal doping, the Kondo resonance is detectable by STM as a sharp peak in the density of states whose energy and width are determined by T_K.[159]

This Kondo scenario would explain our non-observation of Zn resonances in high-Δ regions. The local doping p in the high-Δ regions is simply too low, so T_K there is less than 4.2 K. Even if there is a Zn impurity in one of these regions, there is no Kondo resonance to be seen.

Flatte

Tang and Flatté used the experimental on-site density of states spectrum at a Ni impurity to match a calculation with six adjustable but mostly independently determined parameters. They fit the chemical potential μ based on the unperturbed superconducting density of states far from a Ni impurity. Then they fit the Ni potential, both V_0 (non-magnetic) and V_S (magnetic) which set the energies of the Ni resonances at 9.2 meV and 18.6 meV. They then set the nearest-neighbor hopping δt_{01} based on the linewidth of the resonances. Finally, they must assume a local suppression of the (2-component) superconducting order parameter Δ in order to explain the energy difference between the 9.2 and 18.6 meV resonances on one side of the Fermi level, and the large peak ("coherence peak" or "van Hove singularity") on the other side of the Fermi level. The best fit for the Δ suppression is $\delta\Delta = 6$ meV, starting from an unperturbed local $\Delta = 28$ meV.[157]

A similar calculation and fit shows that a Zn impurity suppresses local Δ by $\delta\Delta = 8$ meV, starting from an unperturbed local $\Delta = 30$ meV. Missing Cu atoms should have a similar effect.[a]

If both Ni and Zn impurities are locally suppressing Δ then it makes sense that we see no Ni or Zn atoms in the highest-Δ regions. The actual shifts in the distribution $\delta\Delta = \overline{\Delta} - \overline{\Delta}_{\text{cutoff}}$ (from table 5.5) are 5.7 meV, 4.9 meV, and 4.7 meV for Zn, Ni, and native defects, respectively. These are comparable to the Tang-predicted shifts of 8 meV, 6 meV, and ∼8 meV. Therefore, according to the Tang calculation, our observation of the low-Δ distribution for impurities would be entirely explained by the local suppression of Δ by each impurity.

[a] Private communication from J.-M. Tang.

Flatté[160] also predicted that the resonance near the Zn impurity would be particle-hole symmetric (i.e. appearing at both -1.5 meV and +1.5 meV) for a fully phase coherent superconducting gap of 40 meV. But the resonance would lose particle-hole symmetry and emphasize the -1.5 meV peak over the +1.5 meV peak if either (1) the gap became a non-superconducting "pseudogap" or (2) the superconducting gap lost phase coherence. Since we measure only the -1.5 meV peak, case (1) or (2) must be true. However, neither case predicts that the -1.5 meV resonance should disappear as well.

However, Flatté[161] has also predicted that the Ni atoms will be a local probe of superconductivity. The Ni resonance will either lose its particle hole symmetry, or disappear altogether, if placed in non-superconducting environment.

Ni atoms placed in regions where there is no pairing coherence would display only the positive energy component of their associated quasiparticles. The negative energy component, which appears only through pairing coherence, would not be visible. One can even imagine circumstances where ordinary quasiparticles found in metals, which are usually pure electron or pure hole, would lose their own coherence. For example, in the case of spin-charge separation the electron itself dissolves into two exotic particles, the 'spinon' and the 'holon'. In this event it is likely that neither an electron nor a hole component would be associated with the Ni atom.

Balatsky

Balatsky and coworkers address the DOS at a nonmagnetic impurity located in a pseudogap region. They find that the mere fact that DOS is depleted at the Fermi energy is sufficient to produce a resonance near the nonmagnetic impurity, such as Zn. While no superconductivity is required to form the impurity state in the PG, if the superconducting fluctuations are present then an additional satellite peak should appear on a symmetric bias due to the particle-hole nature of the Bogoliubov quasiparticles. The relative magnitude of the particle and the hole parts of the impurity spectrum can be used to determine the extend to which the PG is governed by the superconducting fluctuations. In the case of fully nonsuperconducting PG there should be no observable counterpart state.[162]

Their work provides impetus for the use of impurities to distinguish between local phases in cuprates. However, according to their theory, merely landing in a pseudogap region of the crystal would not cause the Zn impurity resonance to vanish, as we see. In fact, according to their theory, all of our observed Zn impurities must already be in pseudogap regions, because none exhibit the particle-hole symmetry they claim is the hallmark of an impurity

in a superconductor. It's possible that the Zn impurities are so disruptive that they each locally create their own pseudogap region.

Senthil & Fisher

Senthil and Fisher provide a formal mathematical theory for fractionalization of the electron quantum number. Underdoped cuprates may have a tendency towards spin-charge separation into new quasiparticles: 'chargons' and 'spinons'. In some regions of the sample, the quasiparticles may be orthogonal to ordinary electrons so the tip electrons can't tunnel in or out because there are no overlapping states available. This means that if the defects created resonances out of these orthogonal quasiparticles, we wouldn't see them.[43]

Granular Superconductivity

Granular superconductivity occurs when microscopic superconducting grains are separated by non-superconducting regions through which Josephson tunneling between the grains establishes the macroscopic superconducting state.[163] Although crystals of the cuprate high-T_c superconductors are not granular in a structural sense, theory indicates that at low levels of hole doping the holes can become concentrated at some locations resulting in hole-rich superconducting domains.[164, 33, 165, 166] Superconductivity due to Josephson tunneling through undoped regions between such domains would represent a new paradigm for underdoped high-T_c superconductors. Since we observe three different types of defects with possibly starkly different behavior in two distinct types of sample region, it seems likely that in some bulk doping range, BSCCO is best described as a granular superconductor.

5.5 Conclusion

In conclusion, I calculated gapmaps for BSCCO samples of several different dopings, and showed that Δ is very inhomogeneous. I showed that three different types of crystal defect, Zn impurities, Ni impurities, and native defects, appear only in low-Δ regions of the crystal. This distribution is statistically significant. Although I cannot rule out a chemical explanation for this distribution, I propose that the absence of visible defect resonances in high-Δ regions is evidence for a quite different electronic phase. With a local probe such as STM, we may be able to probe nanoscale patches of the far underdoped non-superconducting phase, although bulk crystals in this doping regime are currently impossible to grow.

Bibliography

[1] H. K. Onnes. *Communications from the Physical Laboratory of the University of Leiden* (1911).

[2] W. Meissner and R. Ochsenfeld, "Ein neuer Effekt bei Eintritt der Supraleitfähigkeit." *Naturwissenschaften* **21**, 787–788 (1933).

[3] F. and H. London. *Proceedings of the Royal Society of London* **A149**, 71 (1935).

[4] V. L. Ginzburg and L. D. Landau. *Zh. Eksperim. i Teor. Fiz.* **20**, 1064 (1950).

[5] J. Bardeen, L. N. Cooper, and J. R. Schrieffer, "Theory of Superconductivity." *Physical Review* **108**, 1175–1204 (1957).

[6] L. N. Cooper, "Bound Electron Pairs in a Degenerate Fermi Gas." *Physical Review* **104**, 1189 (1956).

[7] H. Fröhlich, "Theory of the Superconducting State. I. The Ground State at the Absolute Zero of Temperature." *Physical Review* **79**, 845 (1950).

[8] W. S. Corak, B. B. Goodman, C. B. Satterthwaite, and A. Wexler, "Exponential Temperature Dependence of the Electronic Specific Heat of Superconducting Vanadium." *Physical Review* **96**, 1442 (1954).

[9] W. S. Corak, B. B. Goodman, C. B. Satterthwaite, and A. Wexler, "Atomic Heats of Normal and Superconducting Vanadium." *Physical Review* **102**, 656 (1956).

[10] M. A. Biondi, M. P. Garfunkel, and A. O. McCoubrey, "Millimeter Wave Absorption in Superconducting Aluminum." *Physical Review* **101**, 1427 (1956).

[11] R. E. Glover and M. Tinkham, "Transmission of Superconducting Films at Millimeter-Microwave and Far Infrared Frequencies." *Physical Review* **104**, 844 (1956).

[12] R. E. Glover and M. Tinkham, "Conductivity of Superconducting Films for Photon Energies between 0.3 and $40kT_c$." *Physical Review* **108**, 243 (1957).

[13] E. Maxwell, "Isotope Effect in the Superconductivity of Mercury." *Physical Review* **78**, 477 (1950).

[14] C. A. Reynolds, B. Serin, W. H. Wright, and L. B. Nesbit, "Superconductivity of Isotopes of Mercury." *Physical Review* **78**, 487 (1950).

[15] G. Bednorz and K. A. Müller, "Possible high T_c superconductivity in the Ba-La-Cu-O system." *Z. Phys. B* **64**, 189–193 (1986).

[16] M. K. Wu, "Superconductivity at 93 K in a New Mixed-Phase Y-Ba-Cu-O Compound System at Ambient Pressure." *Physical Review Letters* **58**, 908 (1987).

[17] A. A. Abrikosov and L. P. Gor'kov. *Zh. Eksperim. i Teor. Fiz.* **39**, 1781 (1960).

[18] A. A. Abrikosov and L. P. Gor'kov. *Soviet Phys - JETP* **12**, 1243 (1961).

[19] D. A. Wollman, D. J. V. Harlingen, W. C. Lee, D. M. Ginsberg, and A. J. Leggett, "Experimental determination of the superconducting pairing state in YBCO from the phase coherence of YBCO-Pb dc SQUIDs." *Physical Review Letters* **71**, 2134–2137 (1993).

[20] C. C. Tsuei, J. R. Kirtley, C. C. Chi, L. S. Yu-Jahnes, A. Gupta, T. Shaw, J. Z. Sun, and M. B. Ketchen, "Pairing Symmetry and Flux Quantization in a Tricrystal Superconducting Ring of $YBa_2Cu_3O_{7-\delta}$." *Physical Review Letters* **73**, 593–596 (1994).

[21] C. E. Gough, M. S. Colclough, E. M. Forgan, R. G. Jordan, M. Keene, C. M. Muirhead, A. I. M. Rae, N. Thomas, J. S. Abell, and S. Sutton, "Flux quantization in a high-T_c superconductor." *Nature* **326**, 855 (1987).

[22] A. Lanzara, P. V. Bogdanov, X. J. Zhou, S. A. Kellar, D. L. Feng, E. D. Lu, T. Yoshida, H. Eisaki, A. Fujimori, K. Kishios, J.-I. Shimoyama, T. Noda, S. Uchida, Z. Hussain, and Z.-X. Shen, "Evidence for ubiquitous strong electronphonon coupling in high-temperature superconductors." *Nature* **412**, 510–514 (2001).

[23] H.Eisaki, N. Kaneko, D. L. Feng, A. Damascelli, P. K. Mang, K. M. Shen, Z.-X. Shen, and M. Greven, "Effect of chemical inhomogeneity in bismuth-based copper oxide superconductors." *Physical Review B* **69**, 064512 (2004).

[24] D. J. Derro, E. W. Hudson, K. M. Lang, S. H. Pan, J. C. Davis, J. T. Markert, and A. L. de Lozanne, "Nanoscale One-Dimensional Scattering Resonances in the CuO Chains of $YBa_2Cu_3O_{6+x}$." *Physical Review Letters* **88**, 97002 (2002).

[25] H. Maeda, Y. Tanaka, M. Fukutomi, and T. Asano, "A new high-T_c oxide superconductor without a rare-earth element." *Japanese Journal of Applied Physics, Part 2 - Letters* **27**, L209–L210 (1988).

[26] S. Sachdev, "Quantum criticality: competing ground states in low dimensions." *Science* **288**, 475–480 (2000).

[27] P. W. Anderson, "The Resonating Valence Bond State in La_2CuO_4 and Superconductivity." *Science* **235**, 1196–1198 (1987).

[28] I. Affleck and J. B. Marston, "Large-n limit of the Heisenberg-Hubbard model: Implications for high-T_c superconductors." *Physical Review B* **37**, 3774–3777 (1988).

[29] J. B. Marston and I. Affleck, "Large-n limit of the Hubbard-Heisenberg model." *Physical Review B* **39**, 11538–11558 (1989).

[30] T. C. Hsu, J. B. Marston, and I. Affleck, "Two observable features of the staggered-flux phase at nonzero doping." *Physical Review B* **43**, 2866–2877 (1991).

[31] X.-G. Wen and P. A. Lee, "Theory of underdoped cuprates." *Physical Review Letters* **76**, 503–506 (1996).

[32] J. Kishine, P. A. Lee, and X. G. Wen, "Staggered local density of states around the vortex in underdoped cuprates." *Physical Review Letters* **86**, 5365–5368 (2001).

[33] J. Zaanen and O. Gunnarsson, "Charged magnetic domain lines and the magnetism of high-T_c oxides." *Physical Review B* **40**, 7391–7394 (1989).

[34] S. A. Kivelson, E. Fradkin, and V. J. Emery, "Electronic liquid-crystal phases of a doped Mott insulator." *Nature* **393**, 550–553 (1998).

[35] O. Zachar, S. A. Kivelson, and V. J. Emery, "Landau theory of stripe phases in cuprates and nickelates." *Physical Review B* **57**, 1422–1426 (1998).

[36] S. R. White and D. J. Scalapino, "Density matrix renormalization group study of the striped phase in the 2D $t-J$ model." *Physical Review Letters* **80**, 1272–1275 (1998).

[37] U. Löw, V. J. Emery, K. Fabricius, and S. A. Kivelson, "Study of an Ising-model with competing long-range and shortrange interactions." *Physical Review Letters* **72**, 1918–1921 (1994).

[38] S.-C. Zhang, "A unified theory based on $SO(5)$ symmetry of superconductivity and antiferromagnetism." *Science* **275**, 1089–1096 (1997).

[39] M. Vojta and S. Sachdev, "Charge order, superconductivity, and a global phase diagram of doped antiferromagnets." *Physical Review Letters* **83**, 3916–3919 (1999).

[40] E. Demler, S. Sachdev, and Y. Zhang, "Spin-ordering quantum transitions of superconductors in a magnetic field." *Physical Review Letters* **87**, 067202 (2001).

[41] C. M. Varma, "Proposal for an experiment to test a theory of high-temperature superconductors." *Physical Review B* **61**, R3804–R3807 (2000).

[42] S. Chakravarty, R. B. Laughlin, D. K. Morr, and C. Nayak, "Hidden order in the cuprates." *Physical Review B* **63**, 094503 (2001).

[43] T. Senthil and M. P. A. Fisher, "Z_2 gauge theory of electron fractionalization in strongly correlated systems." *Physical Review B* **62**, 7850–7881 (2000).

[44] M. Franz, D. E. Sheehy, and Z. Tešanović, "Magnetic field induced charge and spin instabilities in cuprate superconductors." *Physical Review Letters* **88**, 257005 (2002).

[45] R. B. Laughlin, "Gossamer Superconductivity." http://arxiv.org/abs/cond-mat/0209269 (2002).

[46] B. Lake, H. M. Rønnow, N. B. Christensen, G. Aeppli, K. Lefmann, D. F. McMorrow, P. Vorderwisch, P. Smeibidl, N. Mangkorntong, T. Sasagawa, M. Nohara, H. Takagi, and T. E. Mason, "Antiferromagnetic order induced by an applied magnetic field in a high-temperature superconductor." *Nature* **415**, 299–302 (2002).

[47] J. M. Tranquada, B. J. Sternlieb, J. D. Axe, Y. Nakamura, and S. Uchida, "Evidence for stripe correlations of spins and holes in copper oxide superconductors." *Nature* **73**, 561–563 (1995).

[48] V. J. Emery, S. A. Kivelson, and J. M. Tranquada, "Stripe phases in high-temperature superconductors." *Proceedings of the National Academy of Sciences U. S. A.* **96**, 8814–8817 (1999).

[49] S. H. Pan, E. W. Hudson, and J. C. Davis, "^{3}He Refrigerator Based Very Low Temperature Scanning Tunneling Microscope." *Review of Scientific Instruments* **70**, 1459–1463 (1999).

[50] C. K. Shih, R. M. Feenstra, and G. V. Chandrashekhar, "Scanning tunneling microscopy and spectroscopy of Bi-Sr-Ca-Cu-O 2:2:1:2 high-temperature superconductors." *Physical Review B* **43**, 7913–7922 (1991).

[51] G. Binnig, H. Rohrer, C. Gerber, and E. Weibel, "Surface Studies by Scanning Tunneling Microscopy." *Physical Review Letters* **49**, 5761 (1982).

[52] J. Bardeen, "Tunnelling from a Many-Particle Point of View." *Physical Review Letters* **6**, 57–59 (1961).

[53] M. H. Cohen, L. M. Falicov, and J. C. Phillips, "Superconductive Tunneling." *Physical Review Letters* **8**, 316318 (1962).

[54] N. D. Lang, "Resistance of a one-atom contact in the scanning tunneling microscope." *Physical Review B* **36**, 8173–8176 (1987).

[55] E. W. Hudson, "Investigating High-T_c Superconductivity on the Atomic Scale by Scanning Tunneling Microscopy." Ph.D. thesis, University of California, Berkeley (1999).

[56] A. Damascelli, Z. Hussain, and Z.-X. Shen, "Angle-resolved photoemission studies of the cuprate superconductors." *Reviews of Modern Physics* **75**, 473–541 (2003).

[57] H. Ding, M. R. Norman, J. C. Campuzano, M. Randeria, A. F. Bellman, T. Yokoya, T. Takahashi, T. Mochiku, and K. Kadowaki, "Angle-resolved photoemission spectroscopy study of the superconducting gap anisotropy in $Bi_2Sr_2CaCu_2O_{8+\delta}$." *Physical Review B* **54**, R9678–R9681 (1996).

[58] D. S. Dessau, Z. X. Shen, D. M. King, D. S. Marshall, L. W. Lombardo, P. H. Dickinson, A. G. Loeser, J. Dicarlo, C. H. Park, A. Kapitulnik, and W. E. Spicer, "Key features in the measured band-structure of $Bi_2Sr_2CaCu_2O_{8+\delta}$- flat bands at ε_F and fermi-surface nesting." *Physical Review Letters* **71**, 2781–2784 (1993).

[59] Z.-X. Shen, W. E. Spicer, D. M. King, D. S. Dessau, and B. O. Wells, "Photoemission Studies of High-T_c Superconductors: The Superconducting Gap." *Science* **267**, 5296 (1995).

[60] M. R. Norman, H. Ding, M. Randeria, J. C. Campuzano, T. Yokoya, T. Takeuchi, T. Takahashi, T. Mochiku, K. Kadowaki, P. Guptasarma, and D. G. Hinks, "Destruction of the Fermi surface underdoped high-T_c superconductors." *Nature* **392**, 157–160 (1998).

[61] T. Valla, A. V. Fedorov, P. D. Johnson, B. O. Wells, S. L. Hulbert, Q. Li, G. D. Gu, and N. Koshizuka, "Evidence for quantum critical behavior in the optimally doped cuprate $Bi_2Sr_2CaCu_2O_{8+\delta}$." *Science* **285**, 2110–2113 (1999).

[62] D. L. Feng, D. H. Lu, K. M. Shen, C. Kim, H. Eisaki, A. Damascelli, R. Yoshizaki, J. Shimoyama, K. Kishio, G. D. Gu, S. Oh, A. Andrus, J. O'Donnell, J. N. Eckstein, and Z. X. Shen, "Signature of superfluid density in the single-particle excitation spectrum of $Bi_2Sr_2CaCu_2O_{8+\delta}$." *Science* **289**, 277–281 (2000).

[63] J. Mesot, M. R. Norman, H. Ding, M. Randeria, J. C. Campuzano, A. Paramekanti, H. M. Fretwell, A. Kaminski, T. Takeuchi, T. Yokoya, T. Sato, T. Takahashi, T. Mochiku, and K. Kadowaki, "Superconducting gap anisotropy and quasiparticle interactions: A doping dependent photoemission study." *Physical Review Letters* **83**, 840–843 (1999).

[64] A. Boothroyd, "Introduction to Neutron Scattering." http://xray.physics.ox.ac.uk/Boothroyd/IoPworkshop%20ATB.PDF (2003).

[65] B. Lake, G. Aeppli, K. N. Clausen, D. F. McMorrow, K. Lefmann, N. E. Hussey, N. Mangkorntong, M. Nohara, H. Takagi, T. E. Mason, and A. Schroder, "Spins in the vortices of a high-temperature superconductor." *Science* **291**, 1759–1762 (2001).

[66] H. A. Mook, P. C. Dai, and F. Doğan, "Charge and spin structure in $YBa_2Cu_3O_{6.35}$." *Physical Review Letters* **88**, 097004 (2002).

[67] H. F. Fong, P. Bourges, Y. Sidis, L. P. Regnault, A. Ivanov, G. D. Gu, N. Koshizuka, and B. Keimer, "Neutron scattering from magnetic excitations in $Bi_2Sr_2CaCu_2O_{8+\delta}$." *Nature* **398**, 588–591 (1999).

[68] B. Khaykovich, Y. S. Lee, R. W. Erwin, S. H. Lee, S. Wakimoto, K. J. Thomas, M. A. Kastner, and R. J. Birgeneau, "Enhancement of long-range magnetic order by magnetic field in superconducting La_2CuO_{4+y}." *Physical Review B* **66**, 014528 (2002).

[69] A. Rigamonti, F. Borsa, and P. Carretta, "Basic aspects and main results of NMR-NQR spectroscopies in high-temperature superconductors." *Reports on Progress in Physics* **61**, 1367–1439 (1998).

[70] C. Berthier, M. H. Julien, M. Horvatic, and Y. Berthier, "NMR studies of the normal state of high temperature superconductors." *Journal de Physique I* **6**, 2205–2236 (1996).

[71] M. Takigawa and D. B. Mitzi, "NMR-studies of spin excitations in superconducting $Bi_2Sr_2CaCu_2O_{8+\delta}$single-crystals." *Physical Review Letters* **73**, 1287–1290 (1994).

[72] V. F. Mitrović, E. E. Sigmund, M. Eschrig, H. N. Bachman, W. P. Halperin, A. P. Reyes, P. Kuhns, and W. G. Moulton, "Spatially resolved electronic structure inside and outside the vortex cores of a high-temperature superconductor." *Nature* **413**, 501–504 (2001).

[73] M. Tinkham, *Introduction to Superconductivity* (New York: McGraw-Hill, Inc., 1996), second edition.

[74] M. R. Norman, M. Randeria, H. Ding, and J. C. Campuzano, "Phenomenological models for the gap anisotropy of $Bi_2Sr_2CaCu_2O_{8+\delta}$as measured by angle-resolved photoemission spectroscopy." *Physical Review B* **52**, 615–622 (1995).

[75] R. J. Radtke and M. R. Norman, "Relation of extended Van Hove singularities to high-temperature superconductivity within strong-coupling theory." *Physical Review B* **50**, 9554–9560 (1994).

[76] A. A. Abrikosov, J. C. Campuzano, and K. Gofron, "Experimentally observed extended saddle point singularity in the energy spectrum of $YBa_2Cu_3O_{6.9}$ and $YBa_2Cu_4O_8$ and some of the consequences." *Physica C* **214**, 73–79 (1993).

[77] K. Gofron, J. C. Campuzano, H. Ding, C. Gu, R. Liu, B. Dabrowski, B. W. Veal, W. Cramer, and G. Jennings, "Occurrence of van Hove singularities in $YBa_2Cu_4O_8$ and $YBa_2Cu_3O_{6.9}$." *Journal of Physics and Chemistry of Solids* **54**, 1193–1198 (1993).

[78] M. C. Schabel, C.-H. Park, A. Matsuura, Z.-X. Shen, D. A. Bonn, R. Liang, and W. N. Hardy, "Angle-resolved photoemission on untwinned $YBa_2Cu_3O_{6.95}$. I. Electronic structure and dispersion relations of surface and bulk bands." *Physical Review B* **57**, 6090–6106 (1998).

[79] J. Brinckmann and P. A. Lee, "Slave boson approach to neutron scattering in $YBa_2Cu_3O_{6+y}$ superconductors." *Physical Review Letters* **82**, 2915–2918 (1999).

[80] H. Ding, J. C. Campuzano, A. F. Bellman, T. Yokoya, M. R. Norman, M. Randeria, T. Takahashi, H. Katayama-Yoshida, T. Mochiku, K. Kadowaki, and G. Jennings, "Momentum Dependence of the Superconducting Gap in $Bi_2Sr_2CaCu_2O_{8+\delta}$." *Physical Review Letters* **74**, 2784–2787 (1995).

[81] D. L. Feng, N. P. Armitage, D. H. Lu, A. D. J. P. Hu, P. Bogdanov, A. Lanzara, F. Ronning, K. M. S. H. Eisaki, C. Kim, Z.-X. Shen, J. i. Shimoyama, and K. Kishio, "Bilayer Splitting in the Electronic Structure of Heavily Overdoped $Bi_2Sr_2CaCu_2O_{8+\delta}$." *Physical Review Letters* **86**, 5550–5553 (2001).

[82] H. Ding, A. F. Bellman, J. C. Campuzano, M. Randeria, M. R. Norman, T. Yokoya, T. Takahashi, H. Katayama-Yoshida, T. Mochiku, K. Kadowaki, G. Jennings, and G. P. Brivio, "Electronic Excitations in $Bi_2Sr_2CaCu_2O_{8+\delta}$: Fermi Surface, Dispersion, and Absence of Bilayer Splitting." *Physical Review Letters* **76**, 1533–1536 (1996).

[83] M. R. Norman, "Relation of neutron incommensurability to electronic structure in high-temperature superconductors." *Physical Review B* **61**, 14751–14758 (2000).

[84] M. Eschrig and M. R. Norman, "Neutron Resonance: Modeling Photoemission and Tunneling Data in the Superconducting State of $Bi_2Sr_2CaCu_2O_{8+\delta}$." *Physical Review Letters* **85**, 3261–3264 (2000).

[85] M. Eschrig and M. R. Norman, "Effect of the magnetic resonance on the electronic spectra of high-T_c superconductors." *Physical Review B* **67**, 144503 (2003).

[86] Q. H. Wang and D. H. Lee, "Quasiparticle scattering interference in high-temperature superconductors." *Physical Review B* **67**, 020511 (2003).

[87] J. Corson, J. Orenstein, S. Oh, J. O'Donnell, and J. N. Eckstein, "Nodal quasiparticle lifetime in the superconducting state of $Bi_2Sr_2CaCu_2O_{8+\delta}$." *Physical Review Letters* **85**, 2569–2572 (2000).

[88] Z. X. Shen, D. S. Dessau, B. O. Wells, D. M. King, W. E. Spicer, A. J. Arko, D. Marshall, L. W. Lombardo, A. Kapitulnik, P. Dickinson, S. Doniach, J. Dicarlo, A. G. Loeser, and C. H. Park, "Anomalously large gap anisotropy in the $a-b$ plane of $Bi_2Sr_2CaCu_2O_{8+\delta}$." *Physical Review Letters* **70**, 1553–1556 (1993).

[89] T. Cren, D. Roditchev, W. Sacks, and J. Klein, "Nanometer scale mapping of the density of states in an inhomogeneous superconductor." *Europhys. Lett.* **54**, 84–90 (2001).

[90] S. H. Pan, J. P. O'Neal, R. L. Badzey, C. Chamon, H. Ding, J. R. Engelbrecht, Z. Wang, H. Eisaki, S. Uchida, A. K. Guptak, K. W. Ng, E. W. Hudson, K. M. Lang, and J. C. Davis, "Microscopic electronic inhomogeneity in the high-T_c superconductor $Bi_2Sr_2CaCu_2O_{8+\delta}$." *Nature* **413**, 282–285 (2001).

[91] C. Howald, R. Fournier, and A. Kapitulnik, "Inherent inhomogeneities in tunneling spectra of $Bi_2Sr_2CaCu_2O_{8+\delta}$ crystals in the superconducting state." *Physical Review B* **6410**, 100504 (2001).

[92] K. M. Lang, V. Madhavan, J. E. Hoffman, E. W. Hudson, H. Eisaki, S. Uchida, and J. C. Davis, "Imaging the granular structure of high T_c superconductivity in underdoped $Bi_2Sr_2CaCu_2O_{8+\delta}$." *Nature* **415**, 412–416 (2002).

[93] L. Capriotti, D. J. Scalapino, and R. D. Sedgewick, "Wave-vector power spectrum of the local tunneling density of states: Ripples in a *d*-wave sea." *Physical Review B* **68**, 014508 (2003).

[94] S. A. Kivelson, I. P. Bindloss, E. Fradkin, V. Oganesyan, J. M. Tranquada, A. Kapitulnik, and C. Howald, "How to detect fluctuating stripes in the high-temperature superconductors." *Reviews of Modern Physics* **75**, 1201–1241 (2003).

[95] D. Podolsky, E. Demler, K. Damle, and B. I. Halperin, "Translational symmetry breaking in the superconducting state of the cuprates: Analysis of the quasiparticle density of states." *Physical Review B* **67**, 094514 (2003).

[96] M. F. Crommie, C. P. Lutz, and D. M. Eigler, "Imaging standing waves in a 2-dimensional electron-gas." *Nature* **363**, 524–527 (1993).

[97] Y. Hasegawa and P. Avouris, "Direct observation of standing-wave formation at surface steps using scanning tunneling spectroscopy." *Physical Review Letters* **71**, 1071–1074 (1993).

[98] L. Bürgi, H. Brune, O. Jeandupeux, and K. Kern, "Quantum coherence and lifetimes of surface-state electrons." *Journal of Electron Spectroscopy and Related Phenomena* **109**, 33–49 (2000).

[99] J. Friedel, "The Distribution of Electrons Round Impurities in Monovalent Metals." *Philosophical Magazine* **43**, 153–189 (1952).

[100] C. Wittneven, R. Dombrowski, M. Morgenstern, and R. Wiesendanger, "Scattering states of ionized dopants probed by low temperature scanning tunneling spectroscopy." *Physical Review Letters* **81**, 5616–5619 (1998).

[101] K. Kanisawa, M. J. Butcher, H. Yamaguchi, and Y. Hirayama, "Imaging of friedel oscillation patterns of two-dimensionally accumulated electrons at epitaxially grown InAs(111)A surfaces." *Physical Review Letters* **86**, 3384–3387 (2001).

[102] A. Yazdani, B. A. Jones, C. P. Lutz, M. F. Crommie, and D. M. Eigler, "Probing the local effects of magnetic impurities on superconductivity." *Science* **275**, 1767–1770 (1997).

[103] L. Petersen, P. Hofmann, E. W. Plummer, and F. Besenbacher, "Fourier transform-STM: determining the surface Fermi contour." *Journal of Electron Spectroscopy and Related Phenomena* **109**, 97–115 (2000).

[104] D. Fujita, K. Amemiya, T. Yakabe, H. Nejoh, T. Sato, and M. Iwatsuki, "Observation of two-dimensional Fermi contour of a reconstructed Au(111) surface using Fourier transform scanning tunneling microscopy." *Surface Science* **423**, 160–168 (1999).

[105] J. M. Byers, M. E. Flatte, and D. J. Scalapino, "Influence of gap extrema on the tunneling conductance near an impurity in an anisotropic superconductor." *Physical Review Letters* **71**, 3363–3366 (1993).

[106] C. Howald, H. Eisaki, N. Kaneko, M. Greven, and A. Kapitulnik, "Periodic density-of-states modulations in superconducting $Bi_2Sr_2CaCu_2O_{8+\delta}$." *Physical Review B* **67**, 014533 (2003).

[107] J. E. Hoffman, E. W. Hudson, K. M. Lang, V. Madhavan, H. Eisaki, S. Uchida, and J. C. Davis, "A Four Unit Cell Periodic Pattern of Quasi-Particle States Surrounding Vortex Cores in $Bi_2Sr_2CaCu_2O_{8+\delta}$." *Science* **295**, 466–469 (2002).

[108] D. G. Zhang and C. S. Ting, "Energy-dependent modulations in the local density of states of the cuprate superconductors." *Physical Review B* **67**, 100506 (2003).

[109] T. Pereg-Barnea and M. Franz, "Theory of quasiparticle interference patterns in the pseudogap phase of the cuprate superconductors." *Physical Review B* **68**, 180506 (2003).

[110] C. Bena, S. Chakravarty, J.-P. Hu, and C. Nayak, "Quasiparticle scattering and local density of states in the *d*-density-wave phase." *Physical Review B* **69**, 134517 (2004).

[111] L. Zhu, W. A. Atkinson, and P. J. Hirschfeld, "Power spectrum of many impurities in a *d*-wave superconductor." *Physical Review B* **69**, 060503 (2004).

[112] A. Polkovnikov, M. Vojta, and S. Sachdev, "Pinning of dynamic spin-density-wave fluctuations in cuprate superconductors." *Physical Review B* **65**, 220509 (2002).

[113] A. Polkovnikov, S. Sachdev, and M. Vojta, "Spin collective mode and quasiparticle contributions to STM spectra of *d*-wave superconductors with pinning." *Physica C* **388-389**, 19 (2003).

[114] J. H. Han, "Signature of a collective spin mode in the local tunneling spectra of a d-wave superconductor." *Physical Review B* **67**, 094506 (2003).

[115] B. M. Andersen, "Two nonmagnetic impurities in the d-wave-superconducting and d-density-wave states of the cuprate superconductors as a probe for the pseudogap." *Physical Review B* **68**, 094518 (2003).

[116] K.-K. Voo, H.-Y. Chen, and W. C. Wu, "Defect and anisotropic gap-induced quasi-one-dimensional modulation of the local density of states of $YBa_2Cu_3O_{7-\delta}$." *Physical Review B* **86**, 012505 (2003).

[117] J.-X. Zhu, A. V. Balatsky, J. Sun, and Q. Si, "Effects of Magnetic Collective Modes in the Tunneling Spectra of High-T_c Superconductors." *International Journal of Modern Physics B* **17**, 3473–3478 (2003).

[118] N. B. Christensen, D. F. McMorrow, H. M. Ronnow, B. Lake, S. M. Hayden, G. Aeppli, T. G. Perring, M. Mangkorntong, M. Nohara, and H. Tagaki, "Universal Dispersive Excitations in the High-Temperature Superconductors." http://arxiv.org/PS_cache/cond-mat/pdf/0403/0403439.pdf (2004).

[119] Q. M. Si, Y. Y. Zha, K. Levin, and J. P. Lu, "Comparison of spin dynamics in $YBa_2Cu_3O_{7-\delta}$ and $La_{2-x}Sr_xCuO_4$: effects of Fermi-surface geometry." *Physical Review B* **47**, 9055–9076 (1993).

[120] P. B. Littlewood, J. Zaanen, G. Aeppli, and H. Monien, "Spin fluctuations in a 2-dimensional marginal fermi-liquid." *Physical Review B* **48**, 487–498 (1993).

[121] C. Caroli, P. G. DeGennes, and J. Matricon, "Bound Fermion States on a Vortex Line in a Type-II Superconductor." *Physics Letters* **9**, 307–309 (1964).

[122] H. F. Hess, R. B. Robinson, R. C. Dynes, J. M. Valles, and J. V. Waszczak, "Scanning-Tunneling-Microscope Observation of the Abrikosov Flux Lattice and the Density of States near and inside a Fluxoid." *Physical Review Letters* **62**, 214–216 (1989).

[123] D. J. Griffiths, *Introduction to Quantum Mechanics* (Englewood Cliffs, New Jersey: Prentice-Hall, Inc., 1995), first edition.

[124] G. E. Volovik, "Superconductivity with lines of gap nodes - density-of-states in the vortex." *JETP Letters* **58**, 469–473 (1993).

[125] P. I. Soininen, C. Kallin, and A. J. Berlinsky, "Structure of a vortex line in a $d_{x^2-y^2}$ superconductor." *Physical Review B* **50**, 13883–13886 (1994).

[126] Y. Wang and A. H. MacDonald, "Mixed-state quasi-particle spectrum for d-wave superconductors." *Physical Review B* **52**, R3876–R3879 (1995).

[127] M. Ichioka, N. Hayashi, N. Enomoto, and K. Machida, "Vortex structure in d-wave superconductors." *Physical Review B* **53**, 15316–15326 (1996).

[128] M. Franz and Z. Tešanović, "Self-consistent electronic structure of a $d_{x^2-y^2}$ and a $d_{x^2-y^2} + id_{xy}$ vortex." *Physical Review Letters* **80**, 4763–4766 (1998).

[129] I. Maggio-Aprile, C. Renner, A. Erb, E. Walker, and O. Fischer, "Direct vortex lattice imaging and tunneling spectroscopy of flux lines on $YBa_2Cu_3O_{7-\delta}$." *Physical Review Letters* **75**, 2754–2757 (1995).

[130] C. Renner, B. Revaz, K. Kadowaki, I. Maggio-Aprile, and O. Fischer, "Observation of the low temperature pseudogap in the vortex cores of $Bi_2Sr_2CaCu_2O_{8+\delta}$." *Physical Review Letters* **80**, 3606–3609 (1998).

[131] S. H. Pan, E. W. Hudson, A. K. Gupta, K. W. Ng, H. Eisaki, S. Uchida, and J. C. Davis, "STM studies of the electronic structure of vortex cores in $Bi_2Sr_2CaCu_2O_{8+\delta}$." *Physical Review Letters* **85**, 1536–1539 (2000).

[132] J. L. Tallon and J. W. Loram, "The doping dependence of T^* – what is the real high-T_c phase diagram?" *Physica C* **349**, 53–68 (2001).

[133] Y. Ando, G. S. Boebinger, A. Passner, T. Kimura, and K. Kishio, "Logarithmic divergence of both in-plane and out-of-plane normal state resistivities of superconducting $La_{2-x}Sr_xCuO_4$ in the zero-temperature limit." *Physical Review Letters* **75**, 4662–4665 (1995).

[134] G. S. Boebinger, Y. Ando, A. Passner, T. Kimura, M. Okuya, J. Shimoyama, K. Kishio, K. Tamasaku, N. Ichikawa, and S. Uchida, "Insulator-to-metal crossover in the normal state of $La_{2-x}Sr_xCuO_4$ near optimum doping." *Physical Review Letters* **77**, 5417–5420 (1996).

[135] D. P. Arovas, A. J. Berlinsky, C. Kallin, and S. C. Zhang, "Superconducting vortex with antiferromagnetic core." *Physical Review Letters* **79**, 2871–2874 (1997).

[136] J. X. Zhu and C. S. Ting, "Quasiparticle states at a d-wave vortex core in high-T_c superconductors: Induction of local spin density wave order." *Physical Review Letters* **87**, 147002 (2001).

[137] Q. H. Wang, J. H. Han, and D. H. Lee, "Staggered currents in the mixed state." *Physical Review Letters* **87**, 167004 (2001).

[138] J. P. Hu and S.-C. Zhang, "Theory of static and dynamic antiferromagnetic vortices in LSCO superconductors." *Journal of Physics and Chemistry of Solids* **63**, 2277–2282 (2002).

[139] K. Park and S. Sachdev, "Bond-operator theory of doped antiferromagnets: From Mott insulators with bond-centered charge order to superconductors with nodal fermions." *Physical Review B* **64**, 184510 (2001).

[140] K. Kakuyanagi, K. Kumagai, Y. Matsuda, and M. Hasegawa, "Antiferromagnetic Vortex Core in $Tl_2Ba_2CuO_{6+\delta}$ Studied by Nuclear Magnetic Resonance." *Physical Review Letters* **90**, 197003 (2003).

[141] J. Zaanen, "High-temperature superconductivity - Stripes defeat the Fermi liquid." *Nature* **404**, 714–715 (2000).

[142] K. Matsuba, H. Sakata, N. Kosugi, H. Nishimori, and N. Nishida, "Ordered Vortex Lattice and Intrinsic Vortex Core States in $Bi_2Sr_2CaCu_2O_{8-\delta}$ Studied by Scanning Tunneling Microscopy and Spectroscopy." *Journal of the Physical Society of Japan* **72**, 2153–2156 (2003).

[143] B. W. Hoogenboom, K. Kadowaki, B. Revaz, M. Li, C. Renner, and Ø. Fischer, "Linear and Field-Independent Relation between Vortex Core State Energy and Gap in $Bi_2Sr_2CaCu_2O_{8+\delta}$." *Physical Review Letters* **87**, 267001 (2001).

[144] T. Timusk and B. Statt, "The pseudogap in high-temperature superconductors: an experimental survey." *Reports on Progress in Physics* **62**, 61–122 (1999).

[145] L. Ozyuzer, J. F. Zasadzinski, N. Miyakawa, C. Kendziora, J. Sha, D. G. Hinks, and K. E. Gray, "Tunneling spectroscopy of heavily underdoped crystals of $Bi_2Sr_2CaCu_2O_{8+\delta}$." *Physica C* **341-348**, 927–928 (2000).

[146] B. W. Hoogenboom, K. Kadowaki, B. Revaz, and Ø. Fischer, "Homogeneous samples of $Bi_2Sr_2CaCu_2O_{8+\delta}$." *Physica C* **391**, 376–380 (2003).

[147] M. R. Presland, J. L. Tallon, R. G. Buckley, R. S. Liu, and N. E. Flower, "General Trends in Oxygen Stoichiometry Effects on T_c in Bi and Tl Superconductors." *Physica C* **176**, 95–105 (1991).

[148] S. D. Obertelli, J. R. Cooper, and J. L. Tallon, "Systematics in the thermoelectric power of high-T_c oxides." *Physical Review B* **46**, 1492814931 (1992).

[149] N. Miyakawa, P. Guptasarma, J. F. Zasadzinski, D. G. Hinks, and K. E. Gray, "Strong Dependence of the Superconducting Gap on Oxygen Doping from Tunneling Measurements on $Bi_2Sr_2CaCu_2O_{8-\delta}$." *Physical Review Letters* **80**, 157–160 (1998).

[150] T. Nakano, N. Momono, M. Oda, and M. Ido, "Correlation between the doping dependences of superconducting gap magnitude $2\Delta_0$ and pseudogap temperature T^* in high-T_c cuprates." *Journal of the Physical Society of Japan* **67**, 2622–2625 (1998).

[151] B. vom Hedt, W. Lisseck, K. Westerholt, and H. Bach, "Superconductivity in $Bi_2Sr_2CaCu_2O_{8+\delta}$ single crystals doped with Fe, Ni, and Zn." *Physical Review B* **49**, 9898–9905 (1994).

[152] E. W. Hudson, V. Madhavan, K. McElroy, J. E. Hoffman, K. M. Lang, H. Eisaki, S. Uchida, and J. C. Davis, "STM study of novel resonances in $Bi_2Sr_2CaCu_2O_{8+\delta}$." *Physica B* **329**, 1365–1366 (2003).

[153] S. H. Pan, E. W. Hudson, K. M. Lang, H. Eisaki, S. Uchida, and J. C. Davis, "Imaging the effects of individual zinc impurity atoms on superconductivity in $Bi_2Sr_2CaCu_2O_{8+\delta}$." *Nature* **403**, 746–750 (2000).

[154] E. W. Hudson, K. M. Lang, V. Madhavan, S. H. Pan, H. Eisaki, S. Uchida, and J. C. Davis, "Interplay of magnetism and high-T_c superconductivity at individual Ni impurity atoms in $Bi_2Sr_2CaCu_2O_{8+\delta}$." *Nature* **411**, 920–924 (2001).

[155] H. Hancotte, R. Deltour, D. N. Davydov, A. G. M. Jansen, and P. Wyder, "Superconducting order parameter in partially substituted $Bi_2Sr_2CaCu_2O_{8+x}$ single crystals as measured by the tunneling effect." *Physical Review B* **55**, R3410–R3413 (1997).

[156] K. Westerholt, H. J. Wüller, H. Bach, and P. Stauche, "Influence of Ni, Fe, and Zn substitution on the superconducting and antiferromagnetic state of $YBa_2Cu_3O_{7-\delta}$." *Physical Review B* **39**, 11680–11689 (1989).

[157] J.-M. Tang and M. E. Flatté, "Van Hove features in $Bi_2Sr_2CaCu_2O_{8+\delta}$ and effective parameters for Ni impurities inferred from STM spectra." *Physical Review B* **66**, 060504 (2002).

[158] A. Polkovnikov, S. Sachdev, and M. Vojta, "Impurity in a *d*-wave superconductor: Kondo effect and STM spectra." *Physical Review Letters* **86**, 296–269 (2001).

[159] S. Sachdev, "Spin and charge order in Mott insulators and d-wave superconductors." *Journal of Physics and Chemistry of Solids* **63**, 2269–2276 (2002).

[160] M. E. Flatté, "Quasiparticle resonant states as a probe of short-range electronic structure and Andreév coherence." *Physical Review B* **61**, R14920–R14923 (2000).

[161] M. E. Flatte, "Condensed-matter physics - Nickel probes superconductivity." *Nature* **411**, 901–903 (2001).

[162] H. V. Kruis, I. Martin, and A. V. Balatsky, "Impurity-induced resonant state in a pseudogap, state of a high-T_c superconductor." *Physical Review B* **64**, 054501 (2001).

[163] E. Šimánek, *Inhomogeneous Superconductors: Granular and Quantum Effects* (New York: Oxford University Press, 1994).

[164] L. P. Gor'kov and A. V. Sokol, "Phase stratification of an electron liquid in the new superconductors." *JETP Letters* **46**, 420–423 (1987).

[165] V. J. Emery, S. A. Kivelson, and H. Q. Lin, "Phase-separation in the $t - J$ model." *Physical Review Letters* **64**, 475–478 (1990).

[166] V. J. Emery and S. A. Kivelson, "Frustrated electronic phase-separation and high-temperature superconductors." *Physica C* **209**, 597–621 (1993).

[167] E. Hudson, "Noise in Vibration Measurements." Unpublished (2003).

[168] C. Kittel and Krömer, *Introduction to Thermodynamics* (New York: W. H. Freedman and Company, 1980), second edition.

[169] P. Horowitz and W. Hill, *The Art of Electronics* (Cambridge University Press, 1989).

[170] W. H. Press, S. A. Teukolsky, W. T. Vetterling, and B. P. Flannery, *Numerical Recipes in C* (New York: Cambridge University Press, 2002), second edition.

[171] E. Hoskinson, "Geophone Calibration." Unpublished (2003).

Appendix A

Gapmap Algorithm

This algorithm to find Δ from a given spectrum was written by Kristine Lang and subsequently extensively revised by me.

Main Gapmap Algorithm

The gapmap program calls a function `FindPeakInSpectrum` on each of the 128×128 pixels individially. `FindPeakInSpectrum` walks out from zero energy at the center of the gap and looks for the first feature it can identify as a coherence peak, subject to several filters described in the next section.

Generally the program is set to look for a peak in the range `en1 = 14 meV` to `en2 = 76 meV`. Then it looks for a peak in the range `en1 = -14 meV` to `en2 = -76 meV`. The results Δ_+ and Δ_- are averaged together to give the final output Δ.

A summary of the algorithm is as follows:

```
FindPeakInSpectrum{inSpectrum}

  nPts = size(inSpectrum, /N_ELEMENTS)

  maxVal = MAX(inSpectrum[en1:en2], maxValIndex)

  peakIndex = -1

  posSpectrum = inSpectrum[en1:*]
  derivSpectrum = CalcSimpleDeriv(inSpectrum)[en1:*]
  decrease = (derivSpectrum lt 0)
```

```
fiveptsum = decrease $
        + [decrease[1:*],0] $
        + [decrease[2:*],0,0] $
        + [decrease[3:*],0,0,0] $
        + [decrease[4:*],0,0,0,0]

; indices of points which satisfy 3/5 criterion
threeoffive = where((fiveptsum[0:(en2-en1)] ge 3), count)

; if count<=0 then no peak was found between en1 and en2,
; so return maxValIndex if we suspect the peak is just higher
;   than the given range
; or return error code -1 if we don't think the peak is out of range
if (count le 0) then begin
  if outrangefil then peakIndex=maxValIndex+en1 else peakIndex=-1

; if we are not skipping resonances, then we just return the local max
; by the first point satisfying the 3of5 criterion
end else if (not skipresfil) then begin
  peakIndex = threeoffive[0]
  while ((peakIndex+1) le (en2-en1)) do begin
    if (posSpectrum[peakIndex] ge posSpectrum[peakIndex+1]) then $
      break $
    else $
      peakIndex = peakIndex + 1
  endwhile
  peakIndex = peakIndex + en1

; if we are skipping resonances, then find the first peak which
;   satisfies the skiprespct criterion
; if such points exist, then we return the local max around the first one
; but if such points don't exist, we consider outrangefil
end else begin
  peakIndex = threeoffive[0]
  for i = 0, count-1 do begin
    tempIndex = threeoffive[i]
    while ((tempIndex+1) le (en2-en1)) do begin
      if (posSpectrum[tempIndex] ge posSpectrum[tempIndex+1]) then break $
      else tempIndex = tempIndex + 1
    end
    if (posSpectrum[tempIndex] gt posSpectrum[peakIndex]) then $
      peakIndex = tempIndex
    if (posSpectrum[peakIndex] ge skiprespct/100.0 * maxVal) then break
  end
```

```
      if (posSpectrum[peakIndex] ge skiprespct/100.0 * maxVal) then begin
        peakIndex = peakIndex + en1
      end else begin

        ; if outrangefil is true then we see if the peakIndex we found
        ;   (which is the local max by the global max of all pts satisfying
        ;   the 3of5 criterion) satisfies the outrangepct criterion
        ;   (which is usually less stringent than the outrangecriterion)
        ;   if so, then return peakIndex
        ;   if not, then return maxValIndex
        ; if outrangefil is false, then return -1
        if outrangefil then begin
          if (posSpectrum[peakIndex] ge outrangepct/100.0 * maxVal) then $
            peakIndex = peakIndex + en1 $
          else $
            peakIndex = maxValIndex + en1
        end else begin
          peakIndex = peakIndex + en1
        end
      end ; no peaks found above skiprespct * maxVal
    end ; (skipresfil)
  end ; (en1<en2)
```

Additional Gapmap Filters

`Skip resonances:` If the peak found is less than `x%` of the maximum value in the range, then keep looking for higher peaks, and return the first one to meet the `x%` criterion. If no such peak is found, and if `Peak out of range` is not set, then return `0` (error code).

`Peak out of range:` If no satisfactory peak is found, set gap energy to the location of maximum value in the range, which should be within `2` energy steps of the maximum energy in the range. If `Skip resonances` is set, the peak must be at least `y%` of the maximum value in the range; otherwise any peak is fine.

`Max gap:` Set equal to $\texttt{MAX}\{\Delta_+, \Delta_-\}$ instead of $(\Delta_+ + \Delta_-)/2$.

`Bad pixel:` Wherever there is a bad pixel (i.e. no coherence peak found) set that pixel equal to the average of its nearest neighbors.

`Contiguity:` If a pixel is not within threshold T_1 of half of its nearest neighbors (i.e. `2 of 4`, `1 of 3`, `1 of 2`), then set that pixel equal to the average of its nearest neighbors.

`Pos/Neg Difference:` If Δ_+ and Δ_- differ by more than threshold T_2, then see which one fits better with its nearest neighbors, set the average gapmap equal to that one. If neither agree with nearest neighbors, set the average gapmap equal to $(\Delta_+ + \Delta_-)/2$.

All gapmaps shown in this thesis were calculated using the `Skip resonances` filter (with x = 90%), `Peak out of range` filter (with y = 80%), and `Pos/Neg Difference` filter (with T_2 = 10 meV). It is particularly important to use the `Skip resonances` filter in the Ni-substituted samples. Otherwise the gapmap algorithm will misinterpret the +18 meV resonance as a coherence peak and report an erroneously low value for Δ.

Appendix B

Noise Measurements

A scanning tunneling microscope is extremely sensitive to vibration noise. Changes in the tip-sample separation are exponentially multiplied in the tunneling current: a change in tip-sample separation of as little as an Ångstrom results in an order of magnitude change in the tunneling current. It is therefore extremely important to reduce all external vibrations which might couple to the STM.

This appendix describes the process for measuring the velocity of floor vibrations using a geophone. There is a brief description of electronic noise encountered in geophone measurements, followed by a description of the inner workings of a geophone and a procedure for geophone calibration. Finally, some representative building vibration measurements are reported.

In describing the electronic noise and geophone calibration, I have relied heavily on work done by Eric Hudson and Emile Hoskinson, respectively. I have made some small corrections and clarifications and added a few measurements of my own. It is not my intention to present this document as a body of independent work by myself. However I hope that by bringing the Hudson, Hoskinson, and Hoffman contributions together in one place, this document may serve as a useful reference for future vibration measurements.

B.1 Electronic Noise

Eric Hudson has written a thorough electronic noise summary,[167] and large portions of this section are borrowed from his work. Basic types of electronic noise are:

- **Johnson Noise** arises from fluctuations in voltage across a resistor. Johnson noise takes the form $\Delta V = \sqrt{4k_B T R \Delta f}$. For a resistor at room temperature, Johnson noise becomes $0.13\sqrt{R(\Omega)}$ nV $/\sqrt{\text{Hz}}$.[168] This kind of noise, whose magnitude is flat as a function of frequency, is called "white noise".

- **1/f Noise** arises from fluctuations in the value of the resistance itself, due probably to motion of impurities.[169] This kind of noise, which is the same for each decade of frequency, is called "pink noise".

- **Shot Noise** arises from the quantization of electric charge. At the macroscopic currents we are considering, shot noise will not play a role.

To measure vibrations, one measures the voltage across the two geophone leads. The geophone itself has a resistance r_c, and may also include a damping resistor R_d. The voltage signal is measured using a voltage pre-amplifier and a spectrum analyzer. Choices for the pre-amplifier include: Stanford Research Systems SR560, or Princeton Applied Research 113. Choices for the spectrum analyzer include: Stanford Research Systems SR760 or SR785. Each of these components may contribute electronic noise to the final measurement.

We can measure these sources of noise by working our way up stream from the spectrum analyzer to the pre-amplifier to the geophone. We start by grounding the input to the spectrum analyzer, figuring out the noise of the spectrum analyzer alone, then adding the pre-amplifier, and finally the geophone resistor.

What we are interested in is the "effective input noise". The noise which comes out the final stage of the spectrum analyzer may be quite large, but if we have a very high gain on our pre-amplifier, then our signal is quite large too. The real effect of our output noise must be divided by the gain in order to arrive at the effective input noise.

B.1.1 Spectrum Analyzer

The spectrum analyzer has a front end amplifier stage and an ADC, which each produce noise. After the ADC, everything is digital, so there is no more noise produced after this stage. The noise produced by the ADC does not depend on the spectrum analyzer input gain. Therefore, at high input gain, the effective noise of the ADC is reduced, because the actual noise must be divided by the high gain. Conversely, at low input gain (input attenuation), the effective noise of the ADC is increased. Therefore, we can measure the noise of these two stages independently by setting the input gain to its lowest and highest

levels. At low gains, the ACD noise will dominate, while at high gains, the input amplifier will dominate.

SR760 Spectrum Analyzer

The input gain level ranges from -60dB (i.e. a gain of 1000) to +34dB (i.e. an attenuation of $(1/10)^{(34/20)} = 0.02$). This gain and attenuation occurs in several steps, so the noise may not vary smoothly from one input level to the next, as different gain and attenuation stages are included or excluded.

In fact, as is shown in figures B.1 and B.2, the "noise" of the SR560 is below the level of the lowest ADC bin for most values of the input gain. There remain a few unexplained noise spikes at regular frequency intervals, but these most likely result from the details of the 32-bit logic. All "noise" is below the quoted 90 dB dynamic range of the SR760.

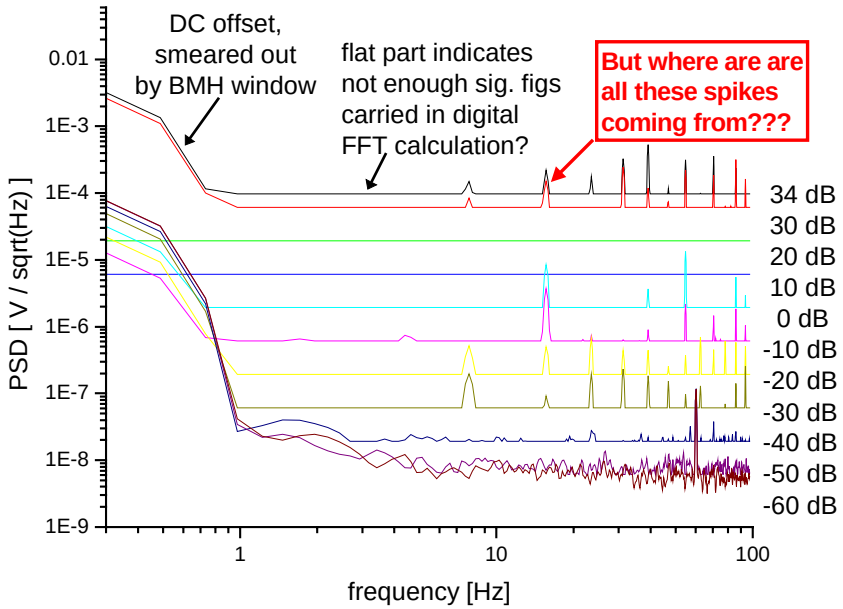

Figure B.1: SR760 noise, characterized in a 12.5 Hz frequency span, for 11 different values of the input level from -34 dB attenuation to 60 dB gain. These spectra show the output of the SR760 with a BNC grounding cap on its input. For the highest values of the input gain, the total noise should be dominated by the input amplifier, while for the lowest values of input gain (i.e. input attenuation), the total noise should be dominated by the ADC. In practice, for all except the highest input gain, the noise is dominated by a series of unexplained spikes superimposed on a constant value which presumably represents the lowest digital bin of the ADC.

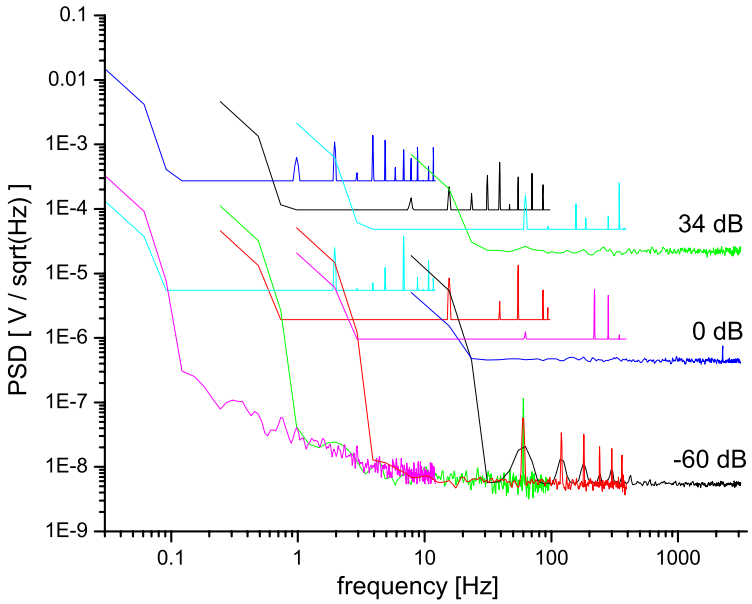

Figure B.2: SR760 noise, characterized across 4 different frequency spans, for 3 different values of the input level from -34 dB attenuation to 60 dB gain. This figure demonstrates that four spectra, all acquired in PSD mode with the same gain, but with different frequency spans, don't match up. The most likely explanation is that they are all in the bottom bit of ADC input, but the digital FFT output is divided by the square-root of the frequency bin size, which is different for each span, to compute the PSD. In order for this explanation to make sense, it must be true that the digital calculations are carried out with more bits than the ADC. In fact, the ADC is 18-bit, with 2 bits reserved for sign, while the digital logic is all carried out with 32 bits.

SR785 Spectrum Analyzer

Both the SR760 and the SR785 have an 18-bit ADC with 2 bits used for sign, so the dynamic range is $2^{16} = 65536$ bins or 90 dB. However the SR785 has a more advanced chip which uses a technique called "noise injection" or "dithering". If the actual signal is relatively quiet, and sits, say 80% of the way between bins 1 & 2, then the ADC will always convert the signal into bin 2. However, if the input signal contains some noise of amplitude larger than the bin width, and if the ADC samples the input multiple times, then it can actually measure a value to much greater accuracy than the bin size. Of course this is only relevant if the internal digital calculations are carried out with greater bit resolution than the nominal bit resolution of the ADC. In the case of the SR785, the input ADC is 18-bit (with 2 bits reserved for sign) with input dithering, while the digital logic is carried out with 32 bits, so the effective dynamic range is much larger than the quoted 90 dB.

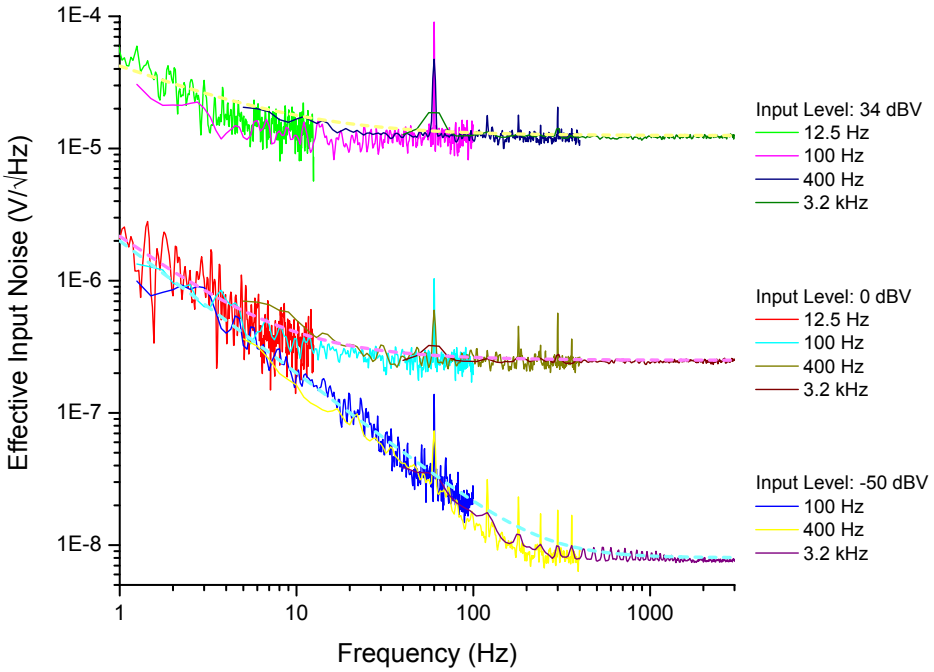

Figure B.3: SR785 noise characterization, by Hudson.[167] Measurements were taken with the SR785 input grounded, at 3 different ranges, for 4 different frequency spans.

The input stage of the SR785, as characterized by Hudson[167], has a $1/f$ noise of $\sim 2f^{-1}$ μV/$\sqrt{\text{Hz}}$ and a high frequency noise floor of 8 nV/$\sqrt{\text{Hz}}$. The signal then passes through a gain depending on the input level setting (IL in dBV): gain $= 10^{(-IL/20)}$. The input level ranges from -50 dbV to 34 dbV in 2 dbV steps. The ADC has a $1/f$ noise of ~ 0.8 μV/$\sqrt{\text{Hz}}$ and a high frequency noise floor of $\sim$ 250 nV/$\sqrt{\text{Hz}}$.

FFT Windowing

Another effect to consider is FFT windowing. The spectrum analyzer captures a time sequence of voltage samples. But the FFT algorithm assumes that this sequence will be periodic, i.e. that the first point will match up to the last point.[170] Of course this is not generally the case for actual measurements of an arbitrary time sample, so there will be a sharp step in the voltage at the boundary between the beginning and the looped around end. This sharp step has high frequency components, higher than the Nyquist frequency of 1/2 the sampling rate. So these high frequency components will be folded back and create inaccuracies in the output FFT.

The way to ameliorate (but not completely fix) this problem is to apply a windowing

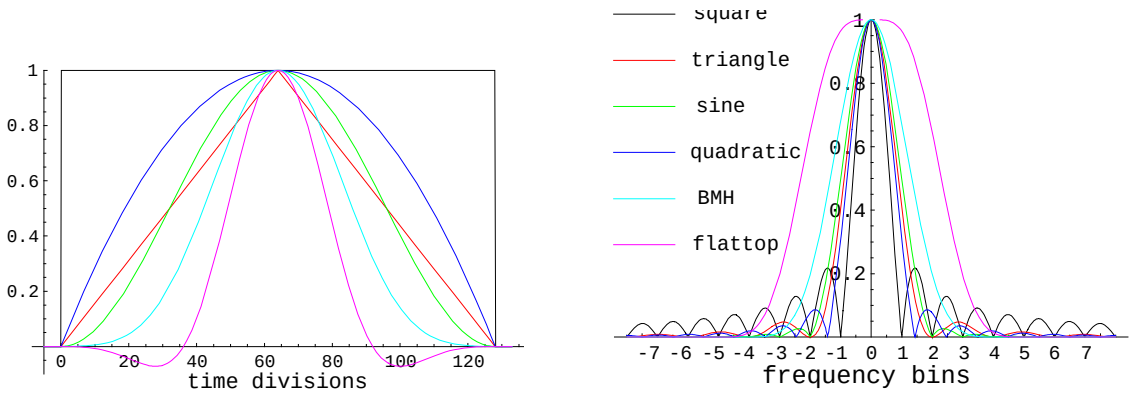

(a) (b)

Figure B.4: Fourier transform windowing functions. (a) Real space windowing functions: all go smoothly to zero at the beginning and end of the time trace except for the square window. (b) Frequency effect of windowing functions: leakage to adjacent frequency bins.

function to the captured time sequence, which sends the beginning and the end smoothly to zero. None of these windows are perfect, and there will always be some leakage from one frequency bin to the next. This is perhaps most relevant at very low frequencies. The input stage of the spectrum analyzer has some DC offset. Although the spectrum analyzer automatically self calibrates every half hour or so, it will always have some DC offset. In practice, this offset seems to be is larger than the signals we are trying to measure at any other frequency. Because of windowing, the DC offset becomes spread out across several adjacent low-frequency bins, as can be seen in figure B.1.

By judicious choice of a windowing function we can minimize the number of adjacent bins into which the DC offset signal will spill. A typical choice (recommended in the spectrum analyzer manual) is the BMH window. Also, by taking measurements across lower and lower frequency ranges (i.e. more and more time consuming measurements) we can push down the frequency at which the DC offset will plague us.

B.1.2 Voltage Pre-Amplifier

SR560 Voltage Pre-Amplifier

The noise floor of the SR560 consists of two main components: a high frequency white noise floor that depends on the gain and dynamic reserve setting, and a $1/f$ component. At the highest gain and low noise setting, the minimum white noise is just less than 4

nV/$\sqrt{\text{Hz}}$. The white noise for all values of the SR560 gain is summarized in table B.1. The $1/f$ noise prefactor appears to scale linearly with the white noise for each gain; the constant of proportionality is ~ 4.5.

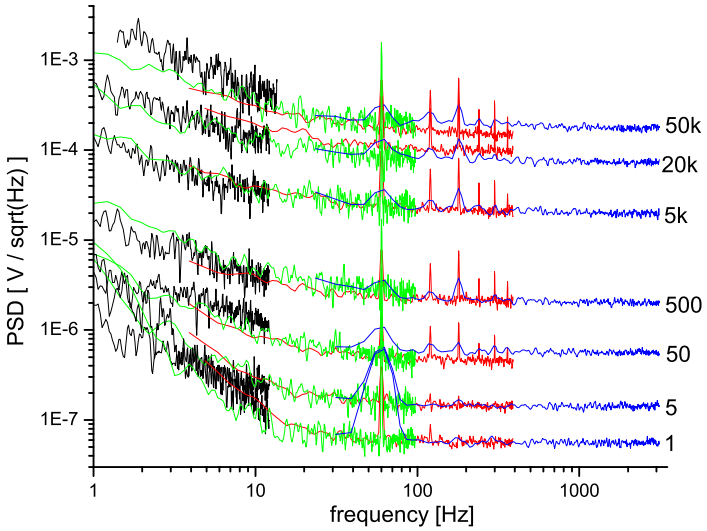

Figure B.5: SR560 noise characterization for seven different values of the SR560 gain, from 1 to 50,000. Measurements were taken with the SR560 input grounded, and the SR560 output connected to the input of the SR760.

PAR 113 Voltage Pre-Amplifier

At the highest gain of the PAR 113, the minimum white noise is $\sim$ 1-2 nV/$\sqrt{\text{Hz}}$, significantly better than the SR560.

B.1.3 Geophone

The resistor(s) in the geophone r_c (and R_d if applicable), each contribute Johnson noise. Our source resistance for the largest geophone used was $r_c = 4500\ \Omega$, and for the smaller geophones used more frequently is typically $r_c = 500\ \Omega$. Therefore, using the Johnson noise formula $0.13\sqrt{R(\Omega)}$ nV /$\sqrt{\text{Hz}}$, the large and small geophones will contribute 8.7 and 2.9 nV /$\sqrt{\text{Hz}}$, respectively.

The geophone resistors will also contribute a $1/f$ noise component. However, this $1/f$ noise will be very difficult to separate from a true vibration signal.

Gain	eff. input noise [nV/$\sqrt{\text{Hz}}$]
1	56.9
2	38.4
5	29.2
10	13.3
20	12.0
50	9.0
100	4.3
200	4.1
500	4.1
1,000	4.1
2,000	4.0
5,000	3.9
10,000	3.9
20,000	3.7
50,000	3.6

Table B.1: SR560 effective input noise characterization, measured for all values of the SR560 gain from 1 to 50,000.

B.1.4 Total Electronic Noise

Taking all noise sources together, the combined effective input noise from the geophone r_c, the SR560, and the SR785, is given by:

Effective input noise (nV / $\sqrt{\text{Hz}}$)

$$= \frac{\sqrt{\left(\left(\text{PreampOutputNoise}^2 + \left(\frac{2000}{f}\right)^2 + 8^2\right) \times 10^{(-IL/20)} + \left(\frac{800}{f}\right)^2 + 250^2\right)}}{10^{(-IL/20)} \times \text{PreampGain}} \quad \text{(B.1)}$$

$$= \sqrt{\text{PreampInputNoise}^2 + \frac{\left(\frac{2000}{f}\right)^2 + 8^2 + \left(\left(\frac{800}{f}\right)^2 + 250^2\right) \times 10^{(IL/20)}}{\text{PreampGain}^2}} \quad \text{(B.2)}$$

where PreampInputNoise is the geophone noise plus the effective input noise of the preamplifier itself, and IL is the input level of the SR785. Equation B.2 makes clear that to

minimize noise we want to use as large a pre-amplifier gain as possible (since the input noise is fixed by the source impedance and the amplifier specifications) and as small an input level as possible (to minimize effects of ADC noise).

To find the noise floor of the vibration measurements in real velocity units, we would just divide this by the (frequency dependent) sensitivity of the geophone.

B.2 How a Geophone Works

Large portions of the section are borrowed from Emile Hoskinson's geophone calibration report.[171] My modifications include:

- fixed a few errors in formulas
- additional figures & circuit diagrams
- equations to calibrate a geophone which has a permanent series resistor R_d

There are two common ways to make vibration measurements. One is intrinsically a velocity-measurement device, while the other is intrinsically an accelerometer.

Typically, velocity is measured with a geophone, which consists of a massive coil on a spring, which can move with respect to a fixed magnet. The motion of the coil with respect to the magnet induces an *emf* in the coil, which can then be put in series with a resistor to produce a measurable voltage. A diagram of a geophone is shown in Fig. B.6.

When the case of the geophone accelerates, the coil moves relative to the fixed magnet, and induces a voltage across the coil:

$$V = -N\frac{d\Phi}{dt} = -N\frac{d\Phi}{dx}\dot{x} \tag{B.3}$$

where N is the number of coil turns, and Φ is the magnetic flux produced by the permanent magnet. We see that the voltage produced is proportional to the velocity, therefore the geophone is intrinsically a velocity-measuring device, with sensitivity G defined by: $V \equiv G\dot{x}$. We can read off the sensitivity from Eq. B.3 as:

$$G = -N\frac{d\Phi}{dx} \tag{B.4}$$

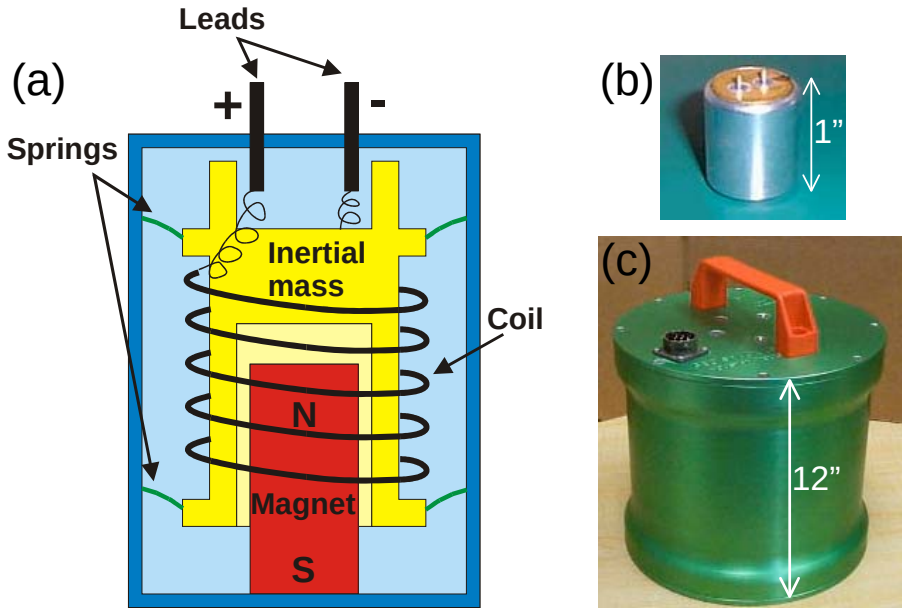

Figure B.6: (a) Schematic of a typical geophone. A massive coil on springs moves with respect to a fixed magnet, inducing a current in the coil which can then be read out as a voltage across the geophone resistance. (b) Photo of a small HS-J geophone from GeospaceLP. (c) Photo of a monstrous green 3-axis geophone, which contains 3 separate GS-1 geophones.

Let's give some thought to the direction of winding of the coil. In the center of the coil, $d\Phi/dx < 0$ by geometry. If the coil moves up with respect to the fixed magnet, then $\dot{x} > 0$, and $d\Phi/dt < 0$. Lens' law requires that the induced current oppose the decrease in upwards pointing flux, so the induced current must create a flux Φ_{ind} which points up, so the induced current must be counter-clockwise. We define the direction of positive current flow to be from the plus terminal to the minus terminal, down around the coil, or counter-clockwise as viewed from above. Therefore an upwards motion of the coil with respect to the fixed magnet produces a positive current and a positive voltage across the terminals from plus to minus. This means that $G > 0$, as we would hope.

If the geophone leads are unconnected, no current flows and the only damping is mechanical, described by a damping constant D. If the geophone drives an external resistive load R_d, then a current I flows through the geophone:

$$V \equiv G\dot{x} = I(R_d + r_c) - L\frac{dI}{dt} \tag{B.5}$$

where r_c is the coil resistance and L is the coil inductance. For an excitation at frequency ω, $\dot{I}(t) \approx \omega I$, so the inductive term will be negligible if $\omega L/(R_d + r_c) \ll 1$.

For example, the values from some GeospaceLP geophones are: [a]

geophone	$r[\Omega]$	$L[H]$	L/r	$\omega L/r$ $[f = 10$ Hz$]$	$\omega L/(R+r)$ $[f = 100$ Hz$]$ $[R = 10r]$
HS-1 (V)	208	0.029	1.40×10^{-4}	0.009	0.008
HS-J-L1 (H1)	1232	0.327	2.65×10^{-4}	0.016	0.015
HS-J-L1 (H2)	306	0.079	2.58×10^{-4}	0.017	0.015
GS-1 (V)	4613	1.440	3.12×10^{-4}	0.020	0.018
GS-1 (H1)	4557	1.903	4.18×10^{-4}	0.026	0.024
GS-1 (H2)	4555	1.982	4.35×10^{-4}	0.027	0.025

Therefore, we can safely ignore the voltage contribution from the inductance of the coil for frequencies below $f \approx 10$ Hz with no damping resistor R, and for frequencies below $f \approx 100$ Hz with a damping resistor $R = 10r$. Neglecting the inductance, we see that the current is proportional to the velocity:

$$I = \frac{G}{R+r}\dot{x} \tag{B.6}$$

There is an additional force on the mass when a current flows, due to the force of the fixed magnetic field gradient which acts on the coil (approximated as a dipole of area NA, where N is the number of loops and A is the area of a single loop).

$$F = m\nabla B = NIA\frac{dB}{dx} = N\frac{d\Phi}{dx}I = -GI = -\frac{G^2}{R_d + r_c}\dot{x} \tag{B.7}$$

For a $\dot{x} > 0$, the current is positive, and the dipole $m = NIA$ points up, while the gradient in field points down, so the resultant force on the coil is down, opposing the direction of motion. Therefore, the flow of current acts as an additional damping force with damping coefficient $G^2/(R+r)$ so the total damping coefficient is now:

$$d = D + \frac{G^2}{R_d + r_c} \tag{B.8}$$

We can compare the strength of the two damping forces. Some approximate parameters are (for an external resistor $R = 0$, short circuit):

[a] http://www.geospaceLP.com

geophone	D	G [V/(m/s)]	$r[\Omega]$	G^2/r
HS-J-L1 (V)	11.0	30	1250	26.5
HS-J-L1 (H1)	6.6	15	300	38.4
GS-1 (V)	0.15	350	4600	0.74
GS-1 (H1)	0.23	420	4550	1.14

Therefore, we see that the electromagnetic damping is much larger than the mechanical damping, so it is important to short the geophone when moving it, to electromagnetically clamp the mass in place an avoid damage to the springs due to the fatigue from violent stretching and compressing.

Taking into account both sources of damping, the sum of all the forces on the mass is therefore:

$$m\ddot{x} = -GI - D\dot{x} - kx \tag{B.9}$$

B.3 Geophone Calibration

A nice, easy-to-automate way to calibrate the geophone (thanks to Emile Hoskinson[171]) is to put a resistor in series with the geophone, apply a sine wave voltage of variable frequency, and map the response voltage across the geophone as a function of frequency. The circuit diagram is shown in Fig. B.7.

For full generality, we have included a parallel damping resistor R_d in addition to the series resistor R, because some Geospace geophones such as the GS-1's come with a permanent damping resistor which can't be removed. (In the smaller geospace geophones such as the HS-J-L1's, there is no damping resistor, so we can take $R_d \to \infty$.) In the configuration of Fig.B.7, the sum of all the voltages around the loop is:

$$V_0 e^{i\omega t} + G\dot{x} = IR + I_2 r \tag{B.10}$$

where we have equated the sources of *emf* on the left side with the resultant voltages across the components on the right side (again ignoring the contribution from the inductor, which we already argued was negligible.)

The voltage across the geophone plus series resistor is therefore:

$$V_0 e^{i\omega t} = IR + I_2 r - G\dot{x} \tag{B.11}$$

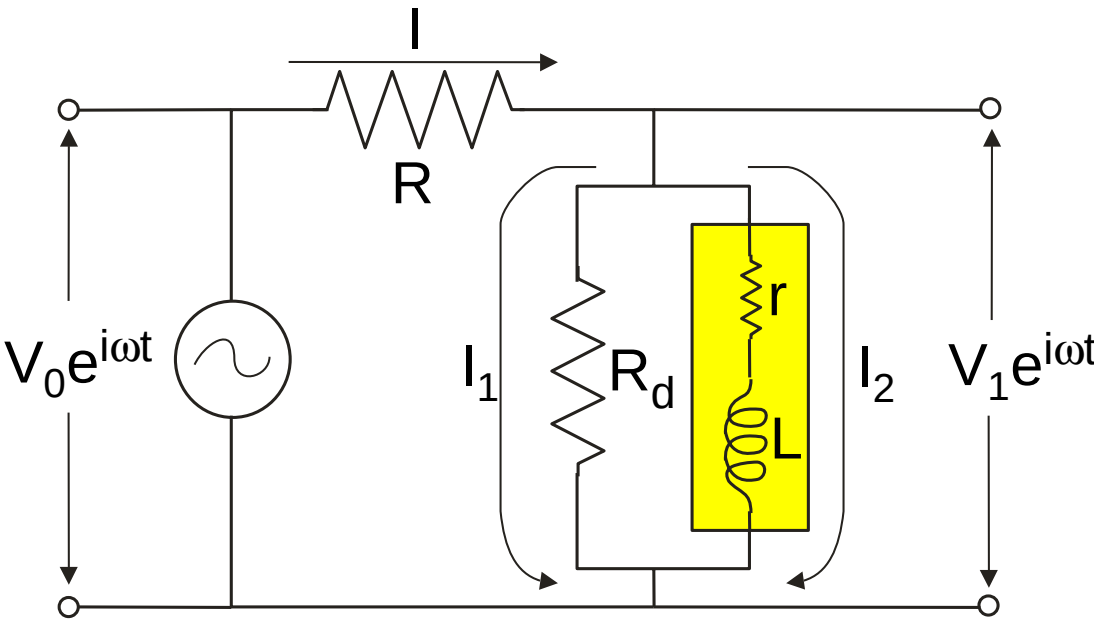

Figure B.7: Circuit diagram for automated geophone calibration. The geophone is shown in yellow; it consists of an internal resistance r plus a coil with inductance L. A damping resistor R_d may be in parallel with the geophone. The geophone is placed in series with a third resistor R. A sinusoidal voltage V_0 is applied, and the resultant voltage V_1 across the geophone is measured.

while the voltage across the geophone alone is:

$$V_1 e^{i\omega t} = V_0 e^{i\omega t} - IR = I_2 r - G\dot{x} \tag{B.12}$$

We can measure the magnitude and phase of V_1/V_0 as a function of frequency, fit each to a pre-calculated functional form, and therefore have two independent measurements of the important parameters of the geophone.

So let's calculate the expected functional form of V_1/V_0. To do this, we first eliminate the currents I and I_2 from the ratio. We note that:

$$I = I_1 + I_2; \quad I_1 R_d = I_2 r \qquad \Rightarrow \qquad I = I_2 \left(1 + \frac{r}{R_d}\right) \tag{B.13}$$

We can find I_2 from the modified version of Eq. B.9:

$$m\ddot{x} = -GI_2 - D\dot{x} - kx \tag{B.14}$$

where the only difference is that now the current flowing through the geophone coil (which is responsible for the damping) is called I_2 instead of I.

This can be re-written as:

$$\ddot{x} + 2\alpha_0\omega_0\dot{x} + \frac{G}{m}I_2 + \omega_0^2 x = 0 \tag{B.15}$$

where $\omega_0 \equiv \sqrt{k/m}$ is the mechanical resonance frequency, and $\alpha_0 \equiv D/(2m\omega_0)$ is the mechanical damping as a fraction of critical damping.

Now we let $\dot{x} = v_0 e^{i\omega t}$, where v_0 may be complex. We can substitute this into Eq. B.15, and solve for I_2:

$$I_2 = -\left[D + im\omega\left(1 - \frac{\omega_0^2}{\omega^2}\right)\right]\frac{v_0 e^{i\omega t}}{G} \tag{B.16}$$

Now we can substitute Eqs. B.13 and B.16 into Eqs. B.11 and B.12, and after some messy algebra, we arrive at:

$$\frac{V_1}{V_0} = \frac{I_2 r - G\dot{x}}{IR + I_2 r - G\dot{x}} = c + \frac{2sc(1-c)}{2\alpha_0 + 2sc + iz} \tag{B.17}$$

where we have defined the following (real) constants:

$$c \equiv \frac{rR_d}{rR_d + RR_d + rR}; \qquad s \equiv \frac{G^2}{2m\omega_0 r}; \qquad z \equiv \frac{\omega}{\omega_0}\left(1 - \frac{\omega_0^2}{\omega^2}\right) \tag{B.18}$$

Note that c is just the ratio V_1/V_0 at DC. In the case of no damping resistor, $R_d \to \infty$ and $c \to r/(r+R)$.

After some more messy algebra, we can arrive at expressions for the magnitude and phase of the ratio:

$$\left|\frac{V_1}{V_0}\right| = c\sqrt{1 + \frac{4b[2\alpha_1 + b]}{4\alpha_1^2 + z^2}} \tag{B.19}$$

$$\theta = \arctan\frac{\mathrm{Im}(V_1/V_0)}{\mathrm{Re}(V_1/V_0)} = \arctan\left(\frac{-z}{2\alpha_1 + \frac{1}{2b}(4\alpha_1^2 + z^2)}\right) \tag{B.20}$$

where we have defined the additional constants:

$$\alpha_1 \equiv \alpha_0 + sc; \qquad b = s(1-c) \tag{B.21}$$

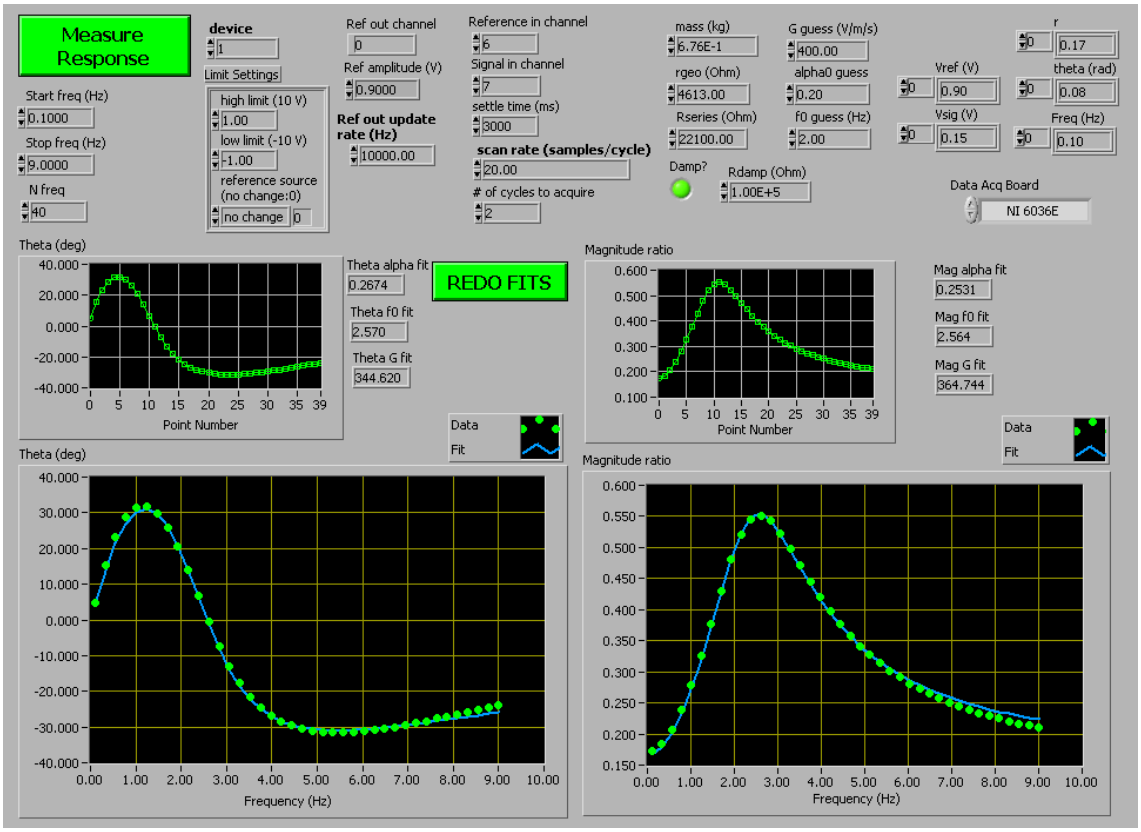

Figure B.8: Labview output for geophone calibration. The graph on the lower left shows the fit to the phase of V_1/V_0 while the graph on the lower right shows the fit to the magnitude of V_1/V_0.

Now we use a Labview program (primarily written by Emile Hoskinson) to sweep the frequency and measure the response, and we can independently do a three parameter fit (α_1, b, and ω_0) to the magnitude and phase of the response to determine the three physical parameters resonance frequency (f_0 via ω_0), sensitivity (G via b and α_1) and damping (α_0 via b and α_1). A typical output is shown in figure B.8.

So now we know f_0, α_0, and G, how do we use them to turn our geophone's output voltage into a velocity in real world units? The full system is described by the differential equation:

$$m(\ddot{x} + \ddot{w}) + d\dot{x} + kx = 0 \tag{B.22}$$

where $x(t)$ is the displacement of the coil relative to the case, $\ddot{w}(t)$ is the acceleration of the case (fixed to the ground), and d is the total damping constant ($d = D$ in case of no damping

resistor, while $d = D + G^2/(r + R_d)$ for damping resistor R_d). This can be rewritten as:

$$\ddot{x} + 2\alpha\omega_0\dot{x} + \omega_0^2 x = a_g e^{i\omega t} \tag{B.23}$$

where α is now the total damping constant as a fraction of critical damping, and we have taken the acceleration of the case with respect to the ground for a fixed frequency to be $a_g e^{i\omega t}$.

This equation can be solved by substituting $x = x_c e^{i\omega t}$. We solve for x_c (the position of the coil relative to the case) in terms of a_g (the acceleration of the ground):

$$x_c = \frac{a_g}{(\omega^2 - \omega_0^2) - 2i\alpha\omega_0\omega} \tag{B.24}$$

But we know that the *emf* produced by the geophone will be proportional to the velocity (and we don't care about phase, just maximum amplitude, so we take $|v_c| = |\omega x_c|$ and $|a_g| = |\omega v_g|$), so we can write:

$$\begin{aligned} |V| &= |Gv_c| = \left| \frac{G\omega^2 v_g}{(\omega^2 - \omega_0^2) - 2i\alpha\omega_0\omega} \right| \\ &= \frac{G\left(\frac{\omega^2}{\omega_0^2}\right) v_g}{\sqrt{\left(1 - \frac{\omega^2}{\omega_0^2}\right)^2 + 4\alpha^2 \frac{\omega^2}{\omega_0^2}}} \end{aligned} \tag{B.25}$$

There is one remaining complication: Eq. B.25 gives the total *emf* produced by the geophone coil, but this *emf* causes a current to flow through r and possibly R_d (if there is an R_d). We assume for the purposes of measurement that we are using a pre-amplifier with effectively infinite input impedance, so $R \to \infty$ and no current flows except around the loop through r and R_d. Therefore the *emf* is split between the two resistors, and our measured voltage is multiplied by a factor of $R_d/(R_d + r)$ (which of course reduces to 1 in the case where there is no damping resistor R_d).

Therefore, our velocity in real world units is:

$$v_g = V_{\text{meas}} \div \left\{ \frac{G\left(\frac{f^2}{f_0^2}\right)\left(\frac{R_d}{R_d + r}\right)}{\sqrt{\left(1 - \frac{f^2}{f_0^2}\right)^2 + 4\alpha^2 \frac{f^2}{f_0^2}}} \right\} \tag{B.26}$$

where we must calculate α from α_0 according to the value of R_d:

$$\alpha = \frac{1}{2m\omega_0}\left(D + \frac{G^2}{R_d + r}\right) \tag{B.27}$$

B.3.1 Geospace Parameters

In the calibration procedure described above, the only parameter we need to use which we can't measure directly is the mass of the coil. We just need to take Geospace's word for this one. We can measure the resistances ourselves with an ohm-meter.

But it's useful to put in reasonable initial guesses for the various parameters of our fit. And it's nice to be able to compare our final calibration results with the company specs. So here is a list of parameters typically given by Geospace, and what they mean:

Parameter	Geospace Symbol	Our Symbol
Natural Frequency	F_n	f_0
Suspended Mass	m	m
Coil Resistance	R_C	r
Coil Inductance	L_C	L
Damping Resistor	R_L	R_d
Sensitivity		G
Open Circuit Damping	B_0	α_0
Damping Constant	B_C	
Shock		
Coil/Case Displacement Limit		
Overswing (A1)		
Overswing (A2)		

Of these parameters, we have discussed all but the last five. Shock is the maximum shock sustainable by the geophone without damage (presumably this means with the geophone leads shorted, although it doesn't say so explicitly). For example, the maximum shock for the GS-1 geophones (the ones inside the big green cylinder) is $50g$ which is approximately equivalent to dropping the geophone from a height of 5 cm onto a tile floor which will deform by 1 mm on impact.

The coil/case displacement limit is irrelevant to us.

The overswings A1 & A2 are related to an alternate calibration method involving the measurement of subsequent transient response peaks.[171] A1 & A2 are the magnitudes of the first two transient response peaks, apparently in terms of oscilloscope divisions as measured at Geospace.

The damping constant B_c is redundant information with the open circuit damping B_0. It is used for an easy determination of the damping resistance R_d the user must add to achieve a given total damping α. Geospace gives the formula as:

$$R_L = \frac{B_C}{B_T - B_0} - R_C \tag{B.28}$$

or, in our language:

$$B_C = (\alpha - \alpha_0)(R_d + r) \tag{B.29}$$

Comparing this to equation B.8 and recalling that $\alpha = d/(2m\omega_0)$ we see that:

$$B_C = \frac{G^2}{2m\omega_0} \tag{B.30}$$

If we do this calculation for multiple geophones and compare our calculated B_C from Geospace's reported B_C, we find that we are consistently off by a factor of 159, which must be some strange way that Geospace is reporting their units.

B.4 Vibration Results

The STM used in this thesis was located in the basement of Birge Hall at the University of California, Berkeley. The room actually protruded underground from the main footprint of the building, and was surrounded by dirt on five sides. This resulted in an extremely quiet environment. However, even in this isolated "bunker", external events would occasionally couple vibrations into the STM. In rare cases, external vibrations were responsible for crashing the STM tip into the sample, which invariably ended the data run and forced a time consuming temperature cycle. Therefore, we conclude that the vibration profile surrounding this STM defines an approximate cutoff for an acceptable STM operating environment.

I have compiled vibration data from several STM labs around the United States (thanks to Don Eigler for data from IBM Almaden, Séamus Davis for data from Cornell University, Eric Hudson for data from NIST Gaithersburg and MIT, and Ali Yazdani for data from the University of Illinois Urbana-Champaign). The comparison of the data from these STM labs is show in figure B.9.

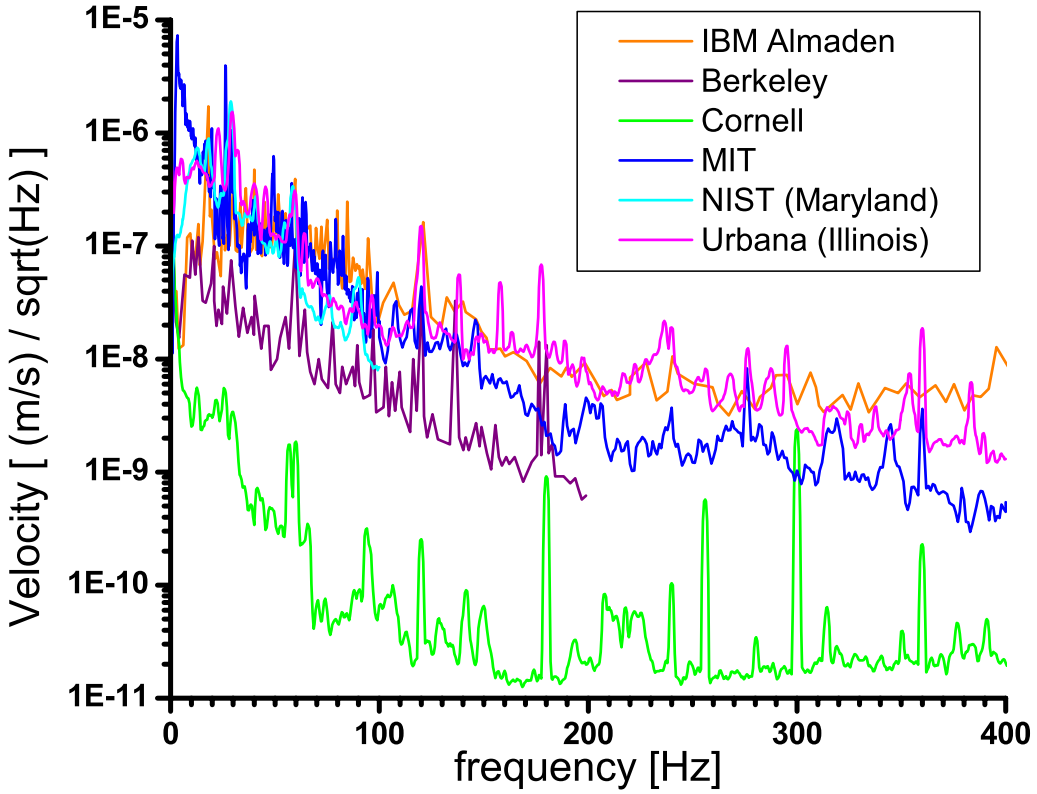

Figure B.9: Vibration measurement results from several STM labs around the country, shown in narrow band velocity units.

Vibrations from five of the labs lie within an order of magnitude of each other, with Berkeley showing the best performance of the five. Conspicuously several orders of magnitude quieter than Berkeley are the new ultra-low-vibration labs constructed by Séamus Davis at Cornell University. These labs consist of 30-ton slabs of concrete, floating on air spring isolators. The entire experiment is enclosed in a double-walled sound room, with the outer wall of cinder blocks and sand, and the inner wall a commercial mineral rock product from IAC. Although the steady-state vibration levels in these labs are perhaps overkill for STM, the major advantage is complete freedom from the isolated very noisy events which can crash an STM tip and destroy 3 months of work.

1/3-Octave analysis

We physicists prefer to display vibration data as a narrow band spectrum in $(\mathrm{m/s})/\sqrt{\mathrm{Hz}}$, because it conveys the largest amount of data. However, the architectural standard for talking about vibrations is 1/3-octave analysis. This is essentially a smoothing technique,

which integrates noise over frequency ranges whose widths are proportional to their center frequencies. Specifically, we display the total integrated rms noise in a band centered at f_0 with width $2^{1/3} \times f_0$. A 1/3-octave band spectrum can easily be calculated from a narrow-band spectrum by adding up the appropriate bins.

American architects also like to talk in μinches/s rather than m/s. They have defined a set of vibration criteria, labeled VC-A through VC-E, where B is twice as quiet as A, C is twice as quiet as B, etc. In order to meet a specific vibration criterion, a room's vibrations must lie entirely below the relevant VC line at at all frequencies. It turns out that the minimum acceptable vibration criterion for STM lies well below the most stringent criterion acknowledged by architectural standards, VC-E. In fact, if we extend the vibration criteria lettering scheme using the same factor of 2 relations, we find that Séamus Davis' new Cornell labs would satisfy VC-M! The same data from figure B.9 are replotted in the architectural units in figure B.10.

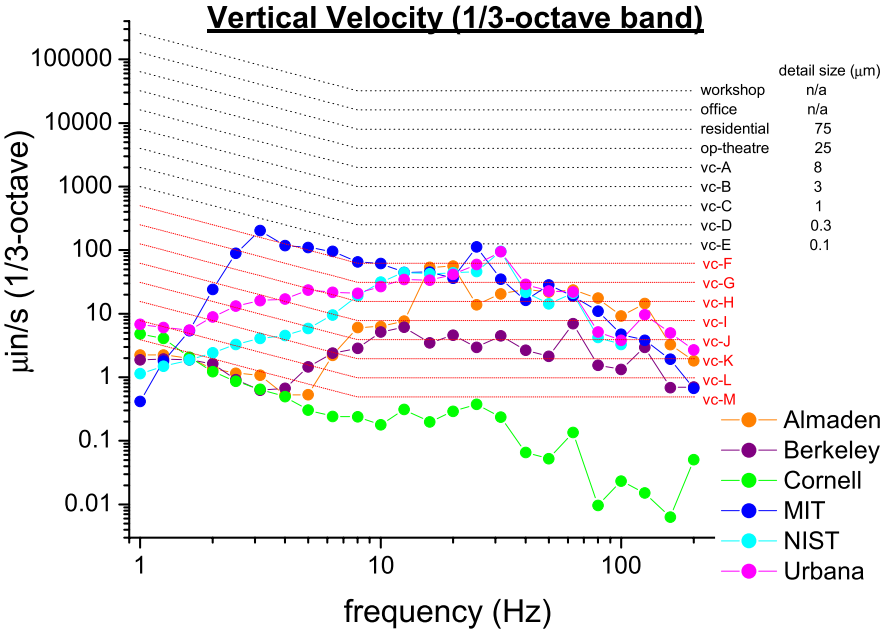

Figure B.10: Vibration measurement results from several successful STM labs, shown in 1/3-octave band units. Vibration criteria A through E are standard architectural criteria. The Davis STM lab at Cornell meets the non-standard criterion 'VC-M'!

Appendix C

STM Construction

I constructed a new scanning tunneling microscope and low-temperature probe with the intent to study high-T_c superconductors near their critical temperatures, around 90 Kelvin.

Because all of the studies reported in this thesis were done at $T = 4.2$ K, maintaining the ultra-high vacuum necessary for clean surface studies was not a challenge. However, when planning an experiment at higher temperatures, one has to pay more consideration to the cleanliness of the system in order to maintain proper vacuum. Therefore, although I borrowed heavily from the existing 4.2 Kelvin STM plans, I redesigned some components for better vacuum compatibility. Specifically, I redesigned all plastic parts, and all solder joints. I also designed a lower impedance pump path between 300 K and 4.2 K.

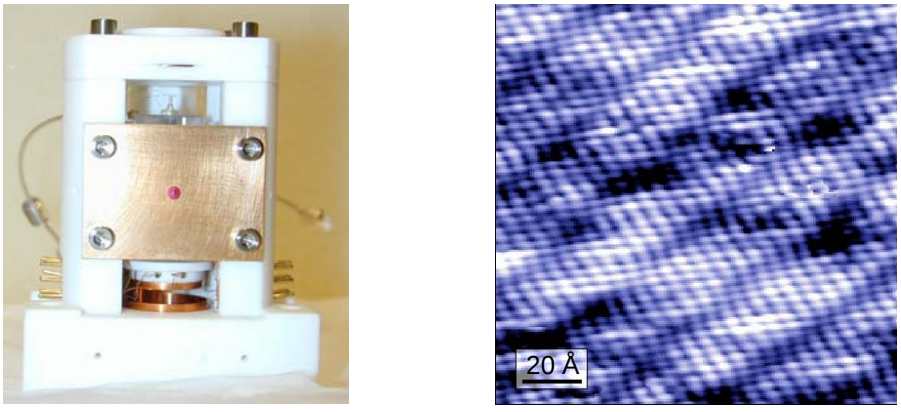

(a) (b)

Figure C.1: New STM construction: (a) photograph of the newly assembled STM (b) first atomic resolution topography acquired with the new STM. This topography was taken at $T \sim 4$ K, on the surface of $Bi_2La_xSr_{2-x}CuO_4$.

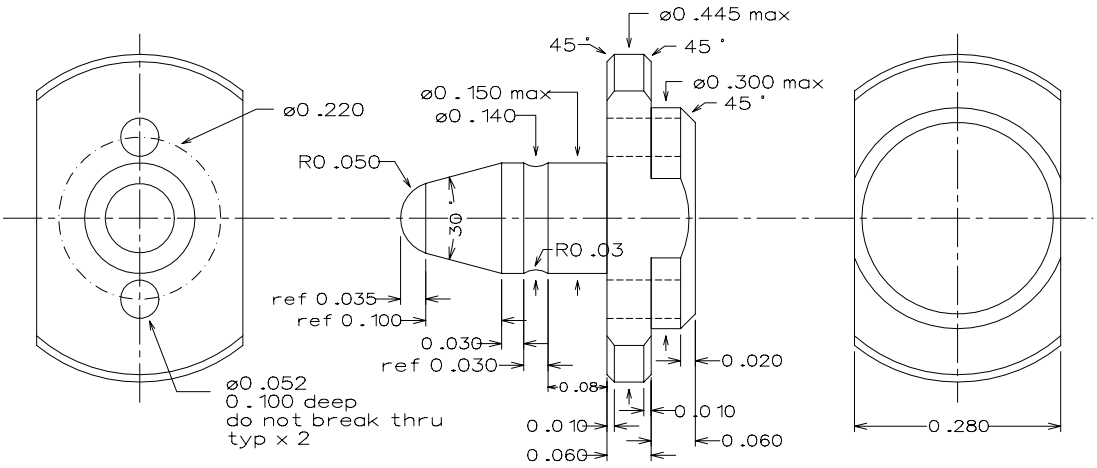

Figure C.2: Copper sample holder stud.

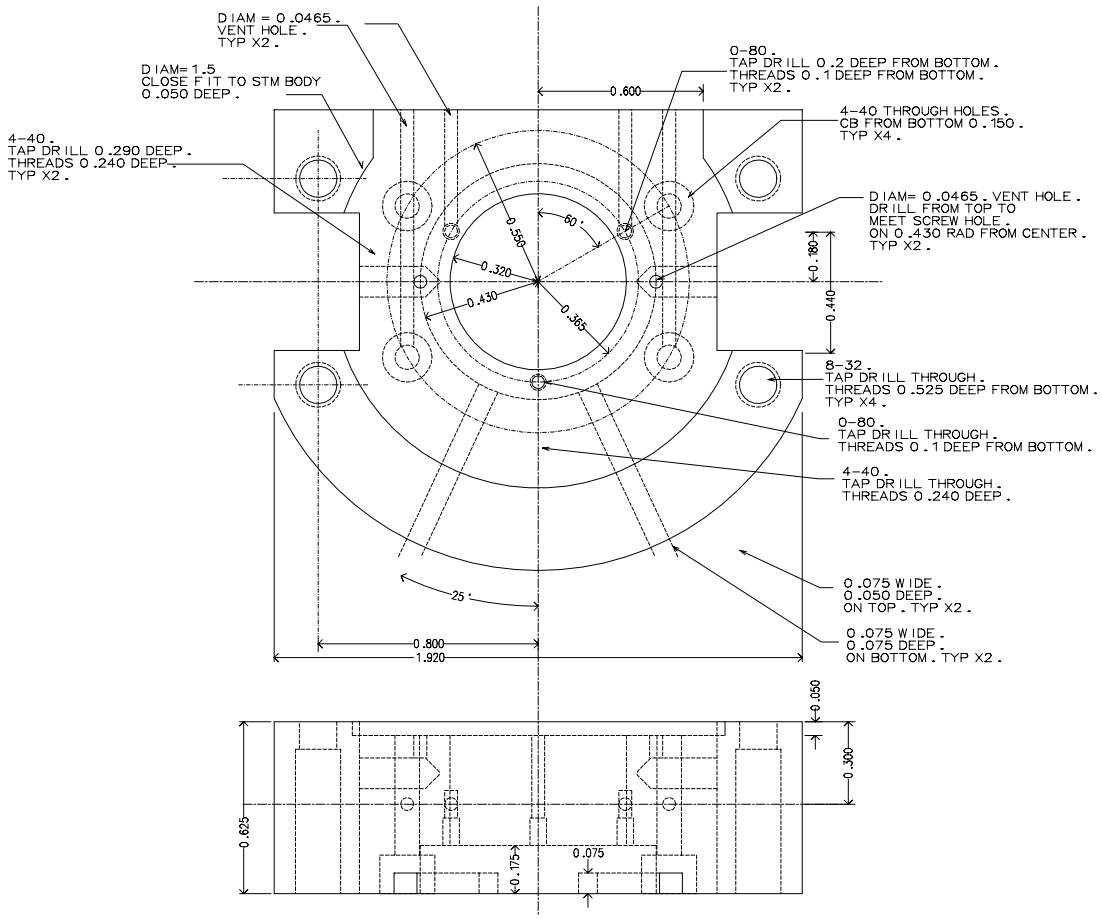

Figure C.3: Macor STM base.

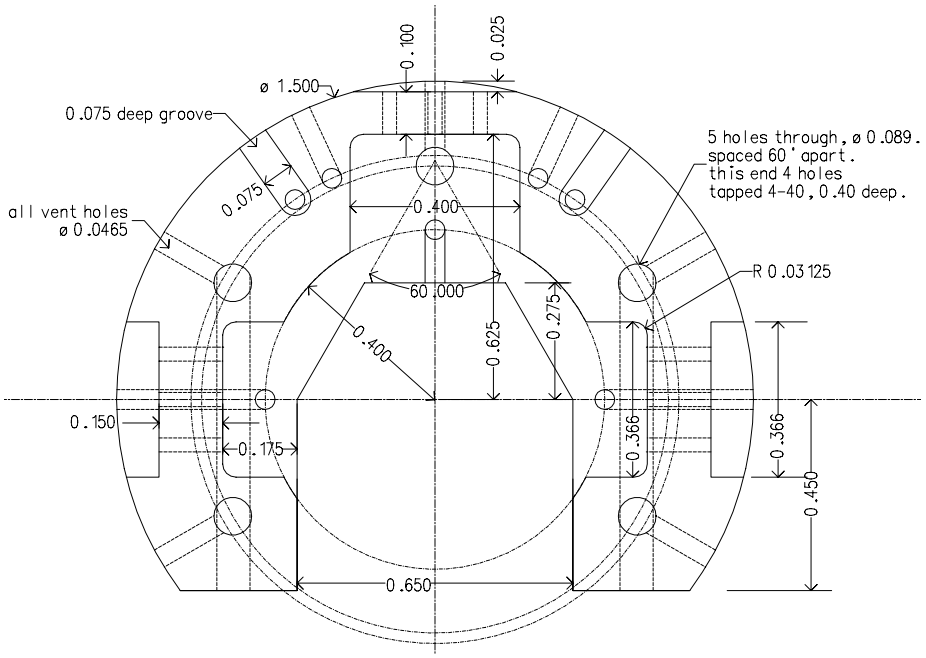

Figure C.4: Macor STM body, bottom.

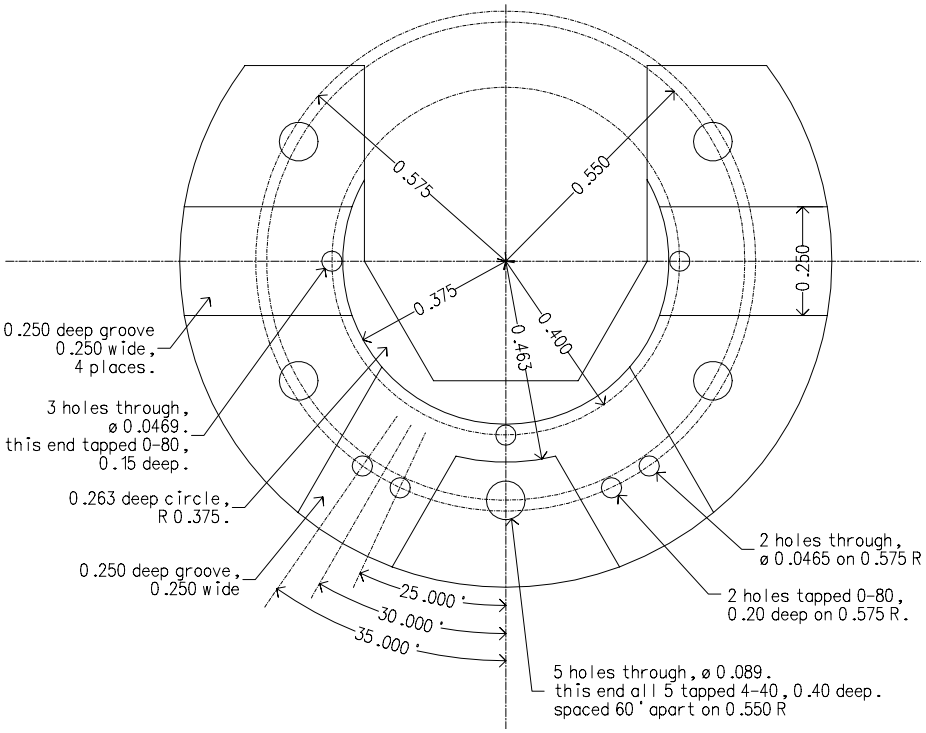

Figure C.5: Macor STM body, top.

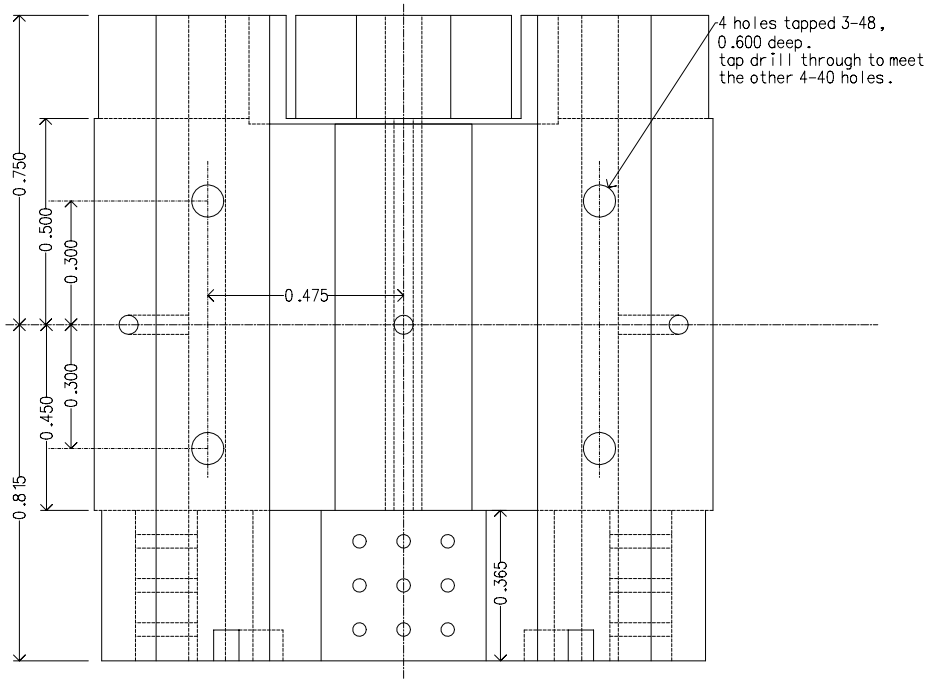

Figure C.6: Macor STM body, front.

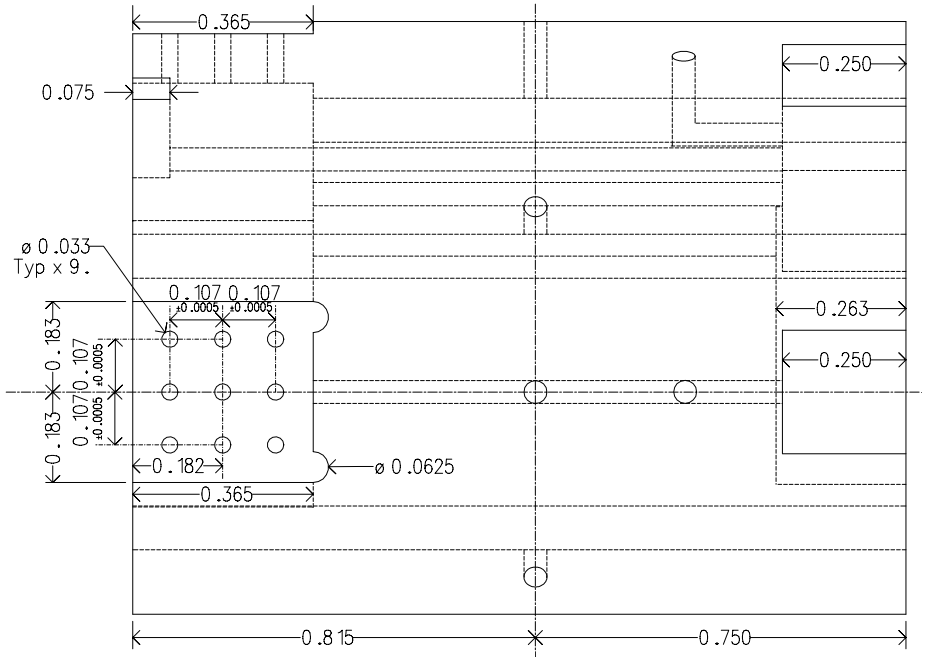

Figure C.7: Macor STM body, right.

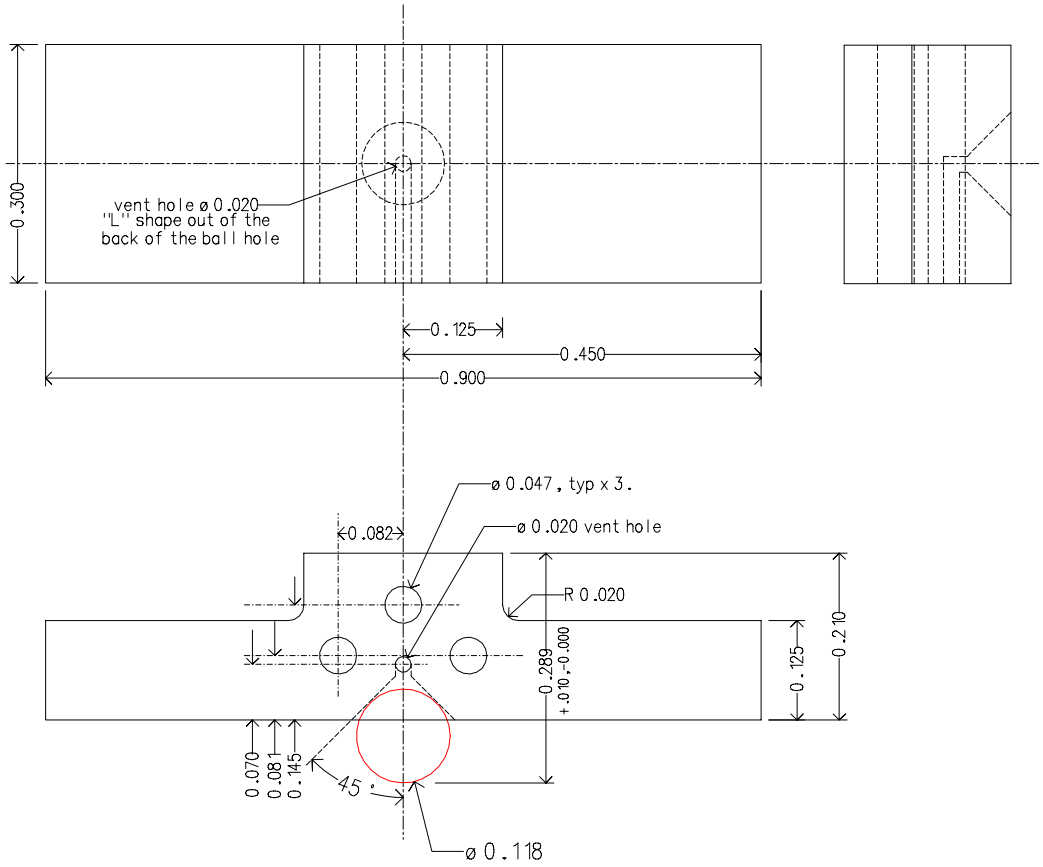

Figure C.8: STM front ball cover.

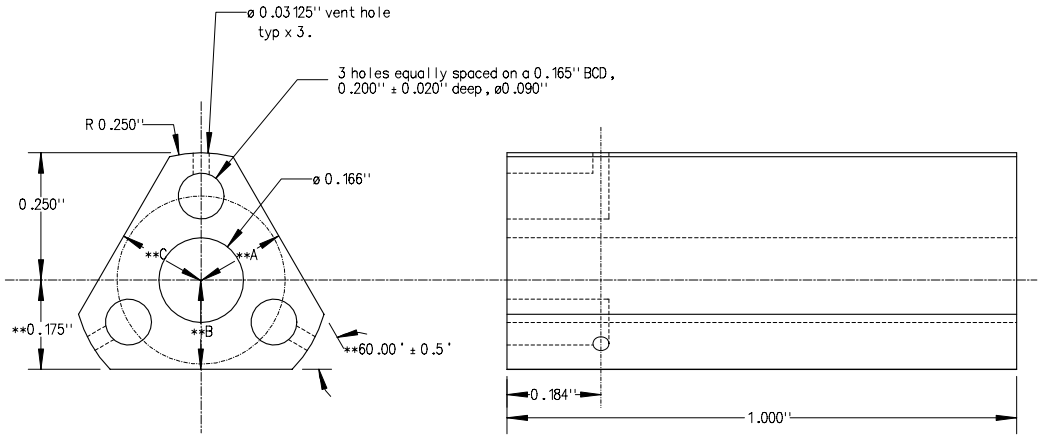

Figure C.9: Sapphire prism.

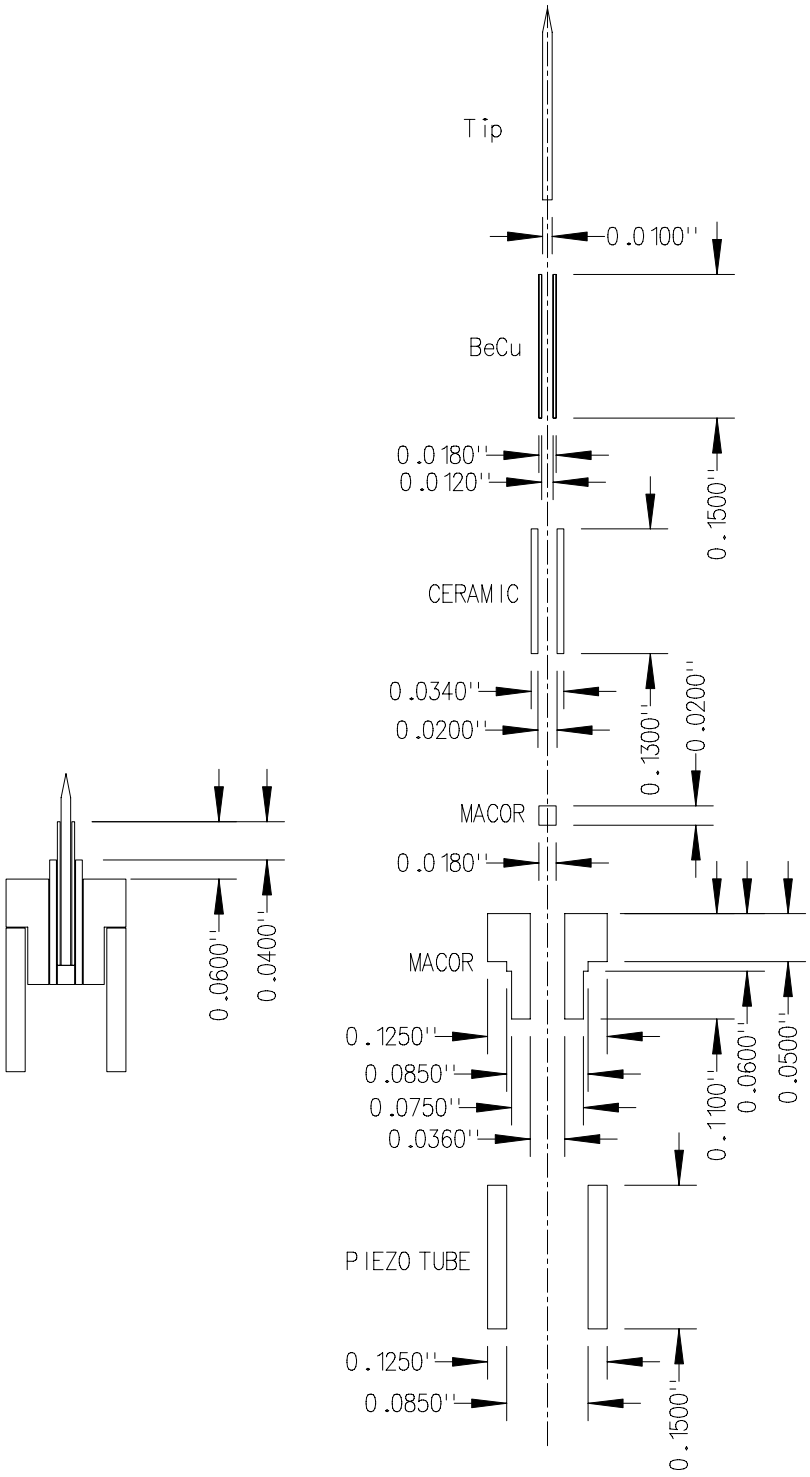

Figure C.10: Tip assembly.

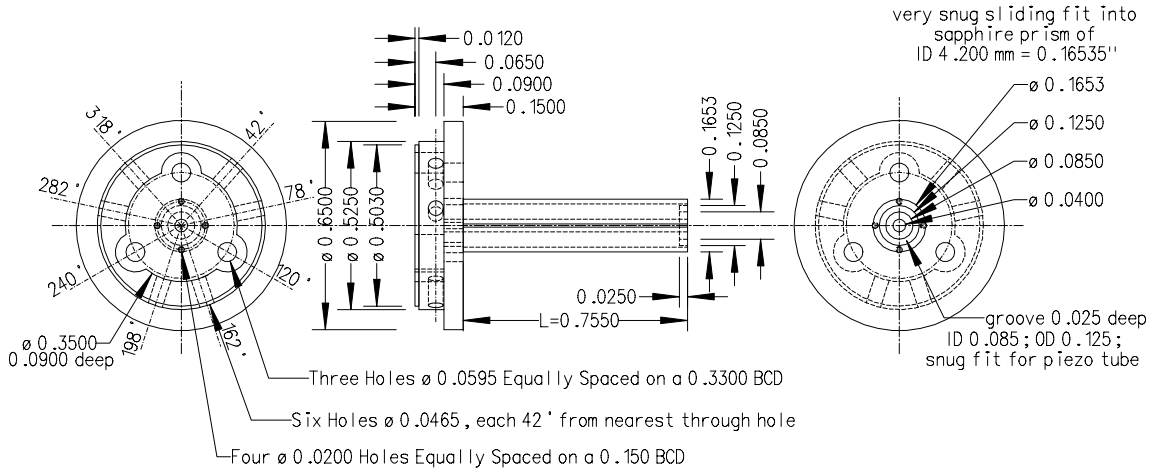

Figure C.11: Macor scanner holder.

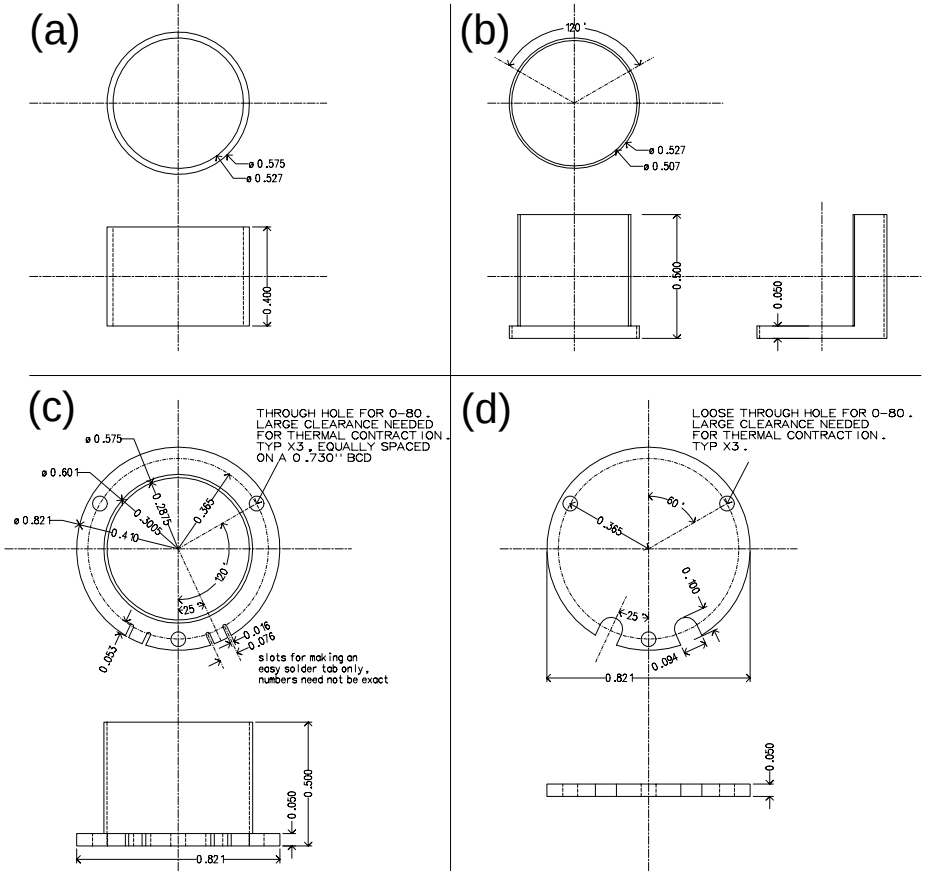

Figure C.12: Capacitive position sensor.